UNIVERSITÀ DEGLI STUDI DEL SANNIO

Dipartimento di Ingegneria

Corso di Laurea Magistrale in Ingegneria Energetica

MASTER THESIS
in
PHYSICS

Optimization of the Beam Size at the Interaction Point of the Accelerator Test Facility 2

Author:
Vera CILENTO

University Supervisor:
Prof. Stefania Petracca

CERN Supervisor:
Dr. Rogelio Tomás

Academic Year 2017/2018

A mio padre… sempre nel cuore…

Optimization of the Beam Size at the Interaction Point of the Accelerator Test Facility 2

by Vera CILENTO

Abstract

A new era of discovery in particle physics has opened in November 2009 with the start-up of the Large Hadron Collider (LHC) at CERN, the European Organization for Nuclear Research, in Geneva, Switzerland. The LHC, a circular proton-proton synchrotron, operates at the highest energies particle accelerators ever achieved. Nowadays, an upgrade of the LHC to achieve instantaneous luminosities a factor of five larger than the LHC nominal value, thereby enabling the experiments to enlarge their data sample by one order of magnitude compared with the LHC baseline programme, has been developed, called the High Luminosity LHC (HL-LHC).

A Linear Collider could be the next large accelerator after LHC. Instead of protons, electrons and their antiparticles, positrons, will be colliding with each other at very high energies. Just like at the LHC, the physics at the Terascale will be explored in order to clarify questions such as the nature of dark matter in the universe, possible new symmetries and new dimensions of space, and to provide the possibility for unexpected discoveries. In comparison to the LHC, the use of electrons and positrons has the advantage of significantly cleaner events with less background, allowing a higher precision and detailed studies of physics beyond the standard model, as well as an analysis of the Higgs mechanism with higher accuracy.

These are some of the reasons that induced the Accelerator Physics community to go towards an electron positron collider. In this context, the High Energy Physics (HEP) community produced a Technical Design Report (TDR) presenting the matured technology, design and construction plan for the International Linear Collider (ILC) [1]. The Compact Linear Collider (CLIC) [2] collaboration demonstrated the feasibility of the project. Therefore, the International Committee for Future Accelerators (ICFA) decided to gather the two projects in order to develop the common issues of the two different technologies in the Linear Collider Collaboration (LCC). The two projects have in common the structure of a linear collider that accelerates the particles to high energy and brings them to collision. These two technologies, ILC, with a maximum energy between 250 GeV and 1 TeV, and CLIC, with energies up to 3 TeV represent the new era of the linear collider research and development platform in the accelerator physics scenario. Furthermore, for these accelerators extremely complex detector systems are designed to achieve high accuracies. More

than a thousand scientists are involved in the development of these new accelerators and detectors world-wide.

This thesis work concentrates on the final-focusing system (FFS) of future linear colliders, like ILC or CLIC. The FFS has the function of squeezing the beams to the IP, down to nanometer transverse sizes. The beam transport and focusing optics in such a system are very challenging. The FFS of CLIC and ILC share the same conceptual design based on the local chromaticity correction scheme (although beam parameters are different, e.g. energy, emittances, beam sizes). On the other hand, CLIC has also an alternative correction scheme, the traditional one [3]. Since the local chromaticity correction scheme was never used in any accelerator before, a small version of this system was built as a demonstrator in order to prove, experimentally, its effectiveness, called ATF2 located at KEK in Japan, near Tokyo. This test facility, operating since early 2010, has achieved many experimental successes, such as achieve the extremely low vertical beam or emittance required for linear accelerators [4, 5].

ATF2 has two main goals: squeeze the beam to 37 nm; and to demonstrate beam stability at IP at nanometer level. In this thesis I focus on the optimization methods to achieve tens of nanometer beam size at the IP in the ATF2 facility, such as mitigation of ground motion effects using the feed-forward control system and experimental studies on ultra-low β_y^* optics. Measurements and simulations results are presented together with a novel proposal to use crystal focusing to reach the same beam size of the traditional focusing scheme (with normal quadrupoles).

An introduction of the framework where this study is carried out, in particular the CLIC and ATF2 projects is presented and discussed in Chapter 1.

Chapter 2 presents some basic concepts of the transverse accelerator physics and some important tools for optics design with particular emphasis on the FFS optics.

The mitigation of ground motion effects using feed-forward control in ATF2 is described in Chapter 3, together with the measurements results achieved in December 2017 and February 2018 beam operations at ATF2 (described in the last section of the Chapter).

In Chapter 4 the feasibility studies, the motivation and the measurements results of the ultra-low β_y^* optics in the ATF2 are presented. The results of the nonlinear beamline optimization for minimizing the IP beam size are presented in the first section of this chapter. In the second section the computer tools for performing the tuning simulations are described. The tuning results achieved in December 2017, February 2018 and May 2018 beam operations are discussed in the last section of this chapter.

A novel concept of optics design using crystal focusing in the FFS region is investigated through simulation studies in Chapter 5. At first, the implementation of the crystal in MAD-X [6] and MAPCLASS [7] environments is described. A first design of a crystal-based FFS optics is presented and compared to the baseline design. Then, luminosity simulations for CLIC 1.5 TeV were done and described in the last section of the Chapter.

Completing this research required 5 visits to the High Energy Accelerator Research Organization (KEK) in Japan and spending 9 weeks working in ATF2. In Chapter 6 all the results obtained during these 9 weeks of operation in December 2017, February 2018 and May 2018 are discussed together with future works.

Acknowledgements

Firstly, I would like to thank and I would like to express my special gratitude to Dr. Rogelio Tomás for giving me the opportunity to work in one of the biggest laboratories for scientific research in the world, the CERN. His unique way of supervision encouraged me to pursue my ideas, to trust my abilities and motivated me to a continuous effort to always obtain new aims on accelerator research studies.

My sincere thanks go to my University supervisor, Prof. Stefania Petracca, for having always believed in my skills since I was in the Bachelor studies and for having helped me to reach my dream of working in the accelerator physics branch.

A special acknowledgement goes to all the ATF2 collaborators, starting from the KEK ones to the CERN, LAL, LAPP and Oxford University ones. I would especially like to thank Toshiyuki Okugi for the help during the machine operation and my CERN colleagues who not only taught me a lot but also shared with me so many experiences. Thanks to Fabien, Jonas, Pierre, Neven and Andrii.

I would also like to say thank you to all my friends that were always there to support me in all my decisions. Many thanks to Annalisa, Maria Letizia, Debora, Emanuela and Raffaella.

Most importantly I would like to express my deep thankfulness to my mother, my sister, my fiancé, my uncle Giovanni and all my beautiful family for their endless support, infinite encouragement and for believing in me all this time.

Contents

List of Abbreviations

CERN	**E**uropean **O**rganization for **N**uclear **R**esearch
KEK	**H**igh **E**nergy **A**ccelerator **R**esearch **O**rganization
LHC	**L**arge **H**adron **C**ollider
CLIC	**C**ompact **LI**near **C**ollider
ILC	**I**nternational **L**inaer **C**ollider
ATF	**A**ccelerator **T**est **F**acility
ATF2	**A**ccelerator **T**est **F**acility **E**xtention
FFS	**F**inal **F**ocus **S**ystem
BDS	**B**eam **D**elivery **S**ystem
DR	**D**amping **R**ing
IP	**I**nteraction **P**oint
MAD-X	**M**ethodical **A**ccelerator **D**esign
PTC	**P**olymorhic **T**racking **C**ode
FD	**F**inal **D**oublet
SR	**S**ynchrotron **R**adiation
BBA	**B**eam **B**ased **A**lignement
BPMs	**B**eam **P**osition **M**onitors
GM	**G**round **M**otion
FF	**F**eed **F**orward

Chapter 1

Introduction

During the last decades, particle accelerators have become highly effective machines to discover and study new particle physics. They have contributed to the formation and consolidation of the Standard Model of particle physics [8] and in particular, the physics potential of future linear colliders has been studied since the Standford Linear Collider (SLC) [9]. The advantage of a linear lepton collider with respect to the LHC is the cleanliness of the events where two elementary particles with known kinematics and spin define the initial state. The resulting precision of the measurements is achievable because of the high resolution possible in the detector due to a clean experimental environment, ability to scan systematically in c.o.m energy and possibility of high degree of polarization. The confirmation of the Standard Model has been achieved through a combination of analyses from LEP, SLC, HERA, B-factories, Tevatron and the LHC. In this model the Higgs mechanism is responsible for the electroweak symmetry breaking and the masses of other particles. A linear collider can be used to conclude if the boson found at LHC has the properties predicted by the Standard Model or if it is part of an extended Higgs sector as in SUSY [10, 11]. An other aspect is that a linear collider can study the presence of composite structure of the Higgs particle and can measure precisely the electroweak coupling of the top quark by directly measuring the top quark mass.

1.1 CLIC Project

There exist two proposals for an e^+e^- linear collider, the International Linear Collider (ILC) [12] promoted by a Global International Collaboration of laboratories and universities, and the Compact Linear Collider (CLIC) led by CERN with an important collaboration of different worldwide laboratories and universities. The Compact Linear Collider is a proposal of the future generation of linear colliders that extends over 48 km. Its goal is to collide e^+e^- beams with a centre-of-mass energy of 3 TeV and delivering a luminosity above $10^{34}\,\mathrm{cm}^{-2}\mathrm{s}^{-1}$. The physics potential of CLIC is reported in [13]. The two main linacs of CLIC accelerate electrons and positrons beams from an energy of about 6 GeV up to 1.5 TeV in a single pass. A

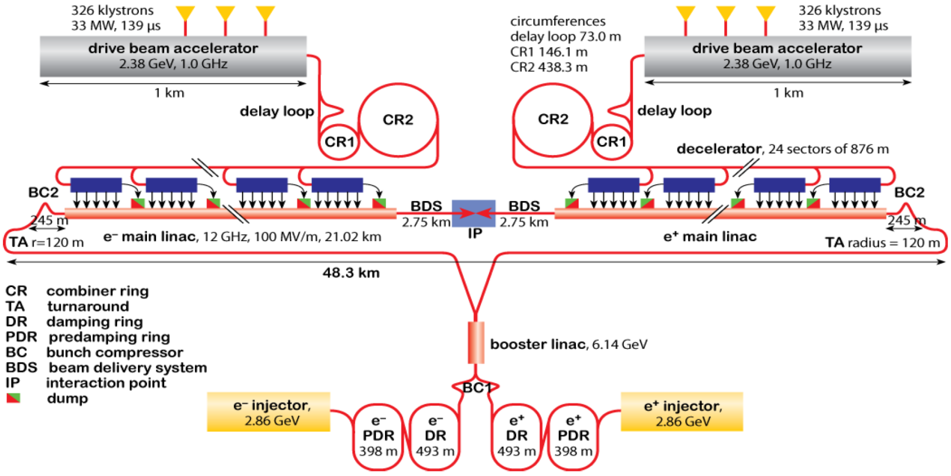

FIGURE 1.1: General scheme of the CLIC 3 TeV machine (figure taken from [15]).

large accelerating gradient of 100 MV/m is foreseen to confine the footprint of the machine within a reasonable scale. CLIC proposes an innovative two-beam acceleration scheme (Main Beam and Drive Beam). It consists of generating first a high intensity and low energy beam (Drive Beam) that runs parallel to the main beam. The Power Extraction and Transfer Structure (PETS) extracts the radio-frequency power of the Drive Beam to build up the high accelerating gradient at the normal-conducting cavities of the main linac. The high current drive beam is obtained by recombining the bunches coming from the drive beam accelerator. This recombination is done in the delay loop and the combiner rings 1 (CR1) and 2 (CR2). Figure 1.1 shows a general layout of CLIC and Table 1.1 summarizes the main parameters of CLIC. Each of the CLIC subsystems source (S), damping ring (DR), main linac (ML) and beam delivery system (BDS) is technically challenging and all of them are of vital importance to reach the required luminosity. In this sense, the test facilities are crucial to study the feasibility of the main linac and the beam delivery system. The Accelerator Test Facilities (ATF and ATF2) are experimental test facilities built at KEK (Japan) meant to address the minimum transverse emittance that can be extracted from the damping ring, and to test the performance of the FFS based on the local chromaticity correction scheme [14].

The CLIC BDS consists of three sections:

- Diagnostics
- Collimation
- Final Focus System

The diagnostics section measures and corrects the beam characteristics at the exit of the linac in order to avoid any mismatch between the ML and BDS subsystems and

Parameter	Symbol	Value	Unit
Center of mass energy	E_{CM}	3.0	[TeV]
Luminosity	$\mathcal{L}$	5.9	$[10^{34} cm^{-2} s^{-1}]$
Peak Luminosity	$\mathcal{L}_{1\%}$	2.0	$[10^{34} cm^{-2} s^{-1}]$
Linac repetition rate	f_{rep}	50	[Hz]
Number of particles/bunch	N_p	3.72	$[10^9]$
Number of bunches/pulse	n_b	312	[-]
Bunch separation	Δt_b	0.5	[ns]
Bunch train length	τ_{train}	156	[ns]
Main Linac RF Frequency	f_{RF}	12.0	[GHz]
Beam power/beam	P_b	14	[MW]
Total site AC power	P_{tot}	392	[MW]
Overall two linac length	l_{linac}	42.16	[km]
Proposed site length	l_{tot}	48.4	[km]

TABLE 1.1: Main parameters of CLIC.

to properly transport the beam towards the FFS. The function of the CLIC collimation section is to protect the down-stream beam line (FFS) and the detector against miss-steered beams from the main linac and to remove the beam halo that enhances the background level in the detector [16].

Final Focus System

The Final Focus System is the last section of the BDS whose main function is to squeeze the horizontal and vertical beam sizes at the IP to the required values. The final part of the FFS is usually formed by a Final Doublet (FD) which is a pair of strong quadrupole magnets located upstream the IP. They are responsible of focusing the transverse beam sizes at the IP. The length of the drift space between the last magnet of the FD and the IP is called L*. The FD focuses the transverse beam size at the IP, moreover the insertion of octupole and decapole magnets as detailed in [17] is required to deliver beam sizes of 45 nm and 1 nm in the horizontal and vertical planes respectively at the IP. The energy spread of the incoming beam leads to a noticeable IP beam size growth due to the fact that the FD quadrupoles focus off-momentum particles to different longitudinal position, this effect is referred to is chromaticity [18] by analogy with light optics. This chromatic effect is corrected by the insertion of sextupole magnets. In order to correct the chromaticity of the lattice two different conceptual FFS designs have been developed over the last decades. The non-local chromaticity correction scheme corrects the transverse chromaticity by two dedicated chromatic sections and afterwards the beam is transported to the final telescope section which demagnifies the beam size (such scheme was experimentally verified by the Stanford Linear Collider (SLC) [19], by the Final Focus Test Beam (FFTB) [20] at SLAC and by B-factories such as KEKB and SuperKEKB

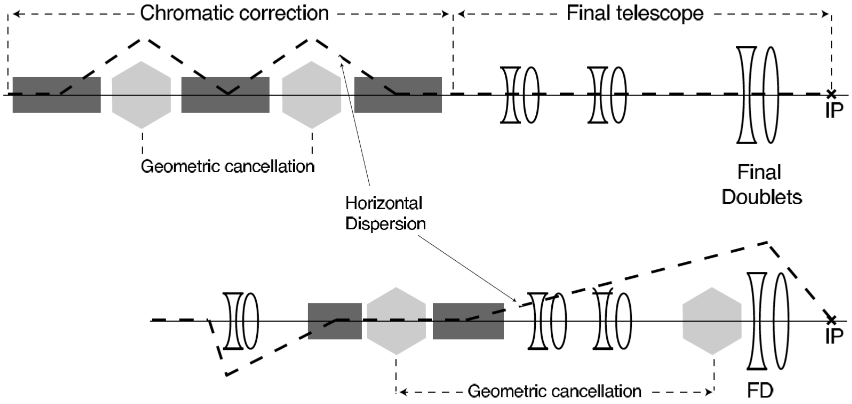

FIGURE 1.2: Scheme of the chromaticity correction with sextupoles located at regions of non zero dispersion due to the presence of dipole magnets. Dash lines represent particle trajectories without chromaticity correction, the continuous lines represent particle trajectories with corrected chromaticity. The upper plot refers to the non-local chromaticity correction scheme, the lower plot shows the local chromaticity correction scheme (figure taken from [14]).

at KEK [21]). An alternative design is the local chromaticity correction proposed in [14] with interleaved sextupole magnets in the FD in order to locally correct the chromaticity. The definition of the chromaticity and details of the local chromaticity correction scheme are given in Section 2.2. Figure 1.2 shows a scheme of both FFS designs. The e^+ and e^- beams cross at the IP at an angle of 20 mrad to allow the extraction of the beams after collision. To preserve the luminosity obtained by head-on collision, the insertion of a crab cavity is mandatory in order to rotate the bunches at the IP recovering the luminosity. In the baseline design of the CLIC BDS 3 TeV, L* is equal to 6 m. In this configuration the last quadrupole magnet (QD0) is placed inside the detector (see figs. 1.3 and 1.4). To avoid a significant luminosity loss due to ground motion described in Chapter 3 and technical vibrations, the limit for the integrated root-mean-square (rms) [22] vertical displacement was set at 0.2 nm above 4 Hz for the final doublet magnets. This requirement is extremely challenging if the quadrupole is supported on the detector, therefore it is foreseen to hold QD0 by a cantilever that relies on a massive pre-insulator located in the cavern wall. With this configuration QD0 avoids the noise from the detector, and vibrates within the tolerances [23]. Increasing L* allows to place QD0 outside the CLIC detector leading to a simpler, more robust and more stable solution of the interaction region. Among the possible lattices, the CLIC BDS with L*=6 m is one of the most attractive solutions in terms of performance. The design and optimization processes of the CLIC BDS with L*=6 m are reported in [23]. This is the current baseline design after CLIC BDS (see fig. 1.3). The obtained beam sizes at the IP for the CLIC BDS L*=6 m design are 40 nm and 0.9 nm in the horizontal and vertical planes, respectively, while for the

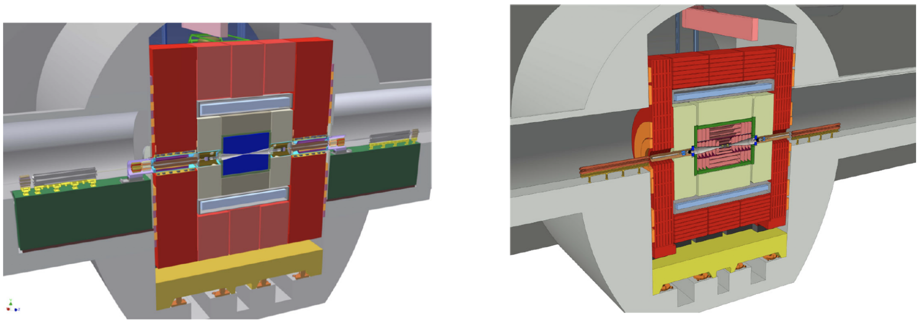

FIGURE 1.3: *Left*: QD0 is located inside the detector and partially supported by the preinsulator (green block) in the tunnel. *Right*: Vertical cut through the new detector model CLICdet allowing QD0 to be located outside of the experiment. No preinsulator or QD0 shielding are needed as opposed to the short L* design in the left figure (figure taken from [23]).

CLIC BDS with L*= 3.5 m σ_x^*=40 nm and σ_y^*=0.7 nm. Table 1.2 summarizes the main parameters of the alternative lattice [16].

			CLIC L*=3.5m	**CLIC L*=6m**
Center of mass energy	E_{CM}	[TeV]	3.0	3.0
Luminosity	$\mathcal{L}$	$[10^{34} cm^{-2} s^{-1}]$	5.9	5.9
Peak Luminosity	$\mathcal{L}_{1\%}$	$[10^{34} cm^{-2} s^{-1}$	2.0	2.0
Linac repetition rate	f_{rep}	[Hz]	50	50
Bunch population	N_e	$[10^9]$	3.72	3.72
Number of bunches	n_b	[-]	312	312
Bunch length	σ_z	$[\mu s]$	44	44
Rms energy spread	δ_p	[%]	0.3	0.3
IP beam size	σ_x^*/σ_y^*	[nm]	40/0.7	40/0.9
Beta function (IP)	β_x^*/β_y^*	[mm]	7/0.068	7/0.12
Normal emittance	$\gamma\epsilon_x/\gamma\epsilon_y$	[nm]	660/20	660/20
FFS length	l_{FFS}	[m]	450	770

TABLE 1.2: CLIC 3 TeV design parameters in both L* options.

1.2 ATF2

The Accelerator Test Facility (ATF) [24] is an accelerator at the High Energy Accelerator Research Organisation (KEK) in Tsukuba, Japan. The ATF is designed as an R&D platform for future linear colliders. The beam operation started in 1997 and the original goal of the facility was to achieve the extremely low vertical beam or emittance required for linear accelerators. The design emittance was achieved in 2001 [4, 5]. The ATF accelerator facility is composed of a photocathode giving electrons to a linac accelerating the particles to 1.3 GeV followed by a damping ring (see fig. 1.4). In 2008 the facility was upgraded to the ATF2 project [25]. The existing machine was

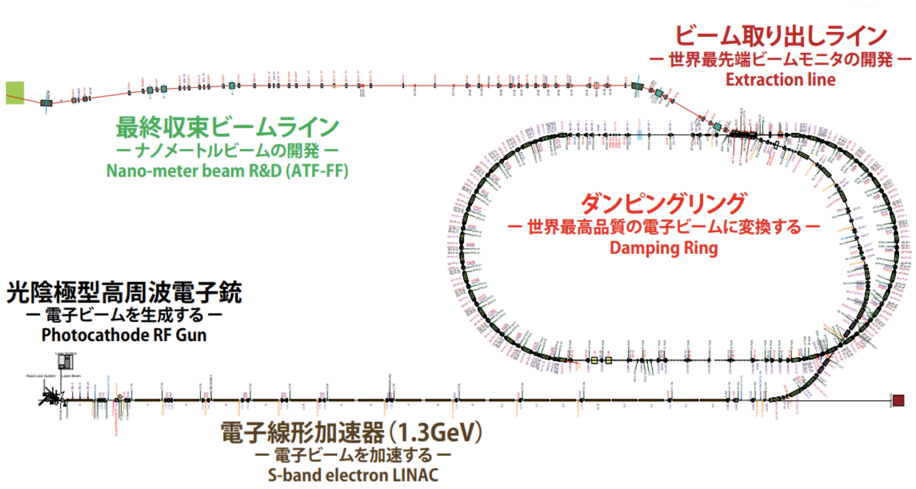

FIGURE 1.4: Schematic layout of the Accelerator Test Facility.

extended with a 100 m beam delivery system consisting of an extraction line and final focus line which are an energy-scaled version of the FFS design for the ILC (see fig. 1.5). The goals of the ATF2 project are to achieve a 37 nm vertical beam size at the IP (goal 1) and to stabilize the IP beam position at the level of few nanometers (goal 2) [25]. The main ATF2 design parameters are given in Table 1.3.

Parameter	Symbol	ATF2 design
Beam energy	$\sqrt{s}[GeV]$	1.3
Energy spread	$\sigma_\delta[\%]$	[0.06,0.08]
Final quad to IP distance	L*[m]	1
Normalized horizontal emittance	$\epsilon_{x,N}[\mu m]$	2.8
Normalized vertical emittance	$\epsilon_{y,N}[nm]$	31
Horizontal emittance	$\epsilon_x[nm]$	2
Vertical emittance	$\epsilon_y[pm]$	12
Horizontal β function at the IP	$\beta_x^*[mm]$	4
Vertical β function at the IP	$\beta_y^*[\mu m]$	100
Horizontal beam size at the IP	$\sigma_x^*[\mu m]$	2.8
Vertical beam size at the IP	$\sigma_y^*[nm]$	37
Natural vertical chromaticity	ξ_y	10000

TABLE 1.3: ATF2 design parameters.

The main parts of ATF2 are:

- **Source and Linac**
  The 88 m long ATF linac consists of an 18 m long 80 MeV pre-injector section and a 70 m long regular accelerator section with energy compensation structures. The RF gun with a 1.6 cell S-Band CsTe photocathode driven by a multi-bunch UV laser generates an electron beam with intensities up to 3.2 nC per

bunch. Eight RF units of accelerating gradient of 35.2 MeV/m are used to accelerate the particle trains containing up to 20 bunches of up to 2×10^{10} particles per bunch. The beam energy at the linac exit is tunable up to a maximum energy of 1.54 GeV, while 1.3 GeV is the usual beam energy in recent operation. The linac is operated at a repetition rate of 25 pps (pulses per second) to accommodate 5 circulating bunch trains in the damping ring [26].

- **Damping Ring (DR)**
  The ATF damping ring is a race-track shaped storage ring with an 138.6 m circumference. The ring arcs are based on the FOBO type cells, where B stands for a combined function bending magnet with horizontal defocusing. The dispersion function is minimized in the bending magnet which helps in reaching a small equilibrium emittance [27]. The beam energy loss due to the synchrotron radiation is compensated by the 714 MHz RF cavity giving harmonic number of 330 and 165 buckets with 2.8 ns spacing [26].

- **Extraction Line (EXT)**
  The EXT extends over 52 m and it comprises an extraction and a diagnostics section. The diagnostics section is used for measuring the emittance and the Twiss parameters and for correcting the dispersion and transverse coupling of the electron beam [28]. The beam is horizontally extracted from the damping ring straight section using a pulsed kicker (KEX1) and a current-sheet septum magnet (BS1X). The septum magnet is followed by two strong dipole magnets (BS2X and BS3X) that bend the extracted beam at an angle of about 20°. A dogleg inflector is located downstream from the septum dipoles comprising two approximately 10° bends (BH1X and BH2X) that offset the beam by 6 m from the damping ring. Downstream from the inflector is the x-y coupling cor-

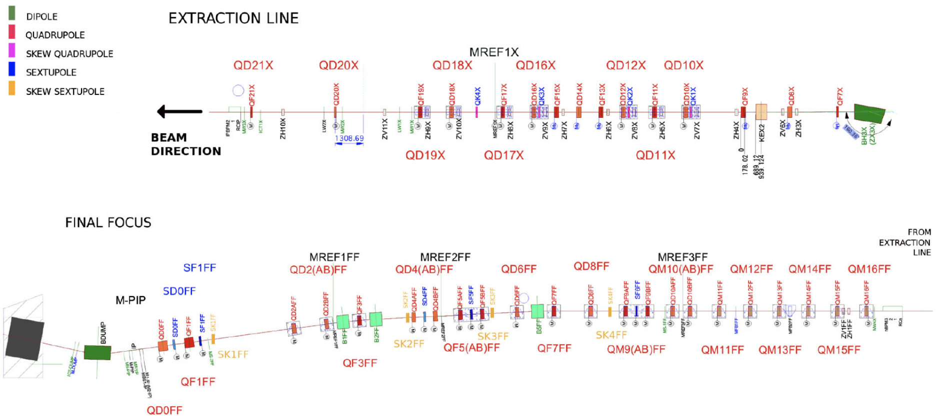

FIGURE 1.5: Scheme of the ATF2. The beam line on the left represents the extraction beam line (EXT). The beam line on the right represents the FFS as the continuation of the EXT line (figure taken from [23]).

rection section consisting of four skew-quadrupoles with appropriate betatron phase advance to make the effects of the skew-quadrupoles orthogonal. The required conditions are that the first and second and also the third and fourth skew-quadrupoles are separated by 90° of phase advance in both planes, and the second and third skew-quadrupoles are separated by 180° in a horizontal plane and 90° in a vertical plane. In consequence, the first skew-quadrupole controls the x-y phase, the second controls the x′-y′ phase, the third the x′-y phase, and the fourth the x-y′ phase. The coupling correction section is followed by the emittance diagnostic section. Because of tight space constraints, the optics for this system is a short, modified FODO structure. The transverse beam emittances are reconstructed by measuring the transverse beam sizes using four Optical Transition Radiation (OTR) monitors [29]. These monitors provide fast single-shot measurements with full ellipse-fitting, allowing simultaneous measurement of the projected x and y spot sizes and the x-y tilt of the beam. Beam sizes at the measurement locations for the ATF2 nominal emittances (ϵ_x =2 nm, ϵ_y = 12 pm) range from 75 to 155 mm in x and from 7 to 20 mm in y [27]. The beam orbit diagnostic in the extraction line is handled by 46 beam position monitors (BPMs). There are 13 stripline BPMs, located mainly in the inflector, with a single-shot resolution of about 10 µm, 33 C-band cavity BPMs [30], with sub-micron single-shot resolution and 2 button-type BPMs located near the septum [26].

- **Final Focus System (FFS)**
  The ATF2 FFS beam line extends over 40 m and it is responsible for transporting and vertically focusing the beam at the IP to tens of nanometers. It consists of a matching section composed of six quadrupole magnets (denoted by QM16FF, QM15FF, QM14FF, QM13FF, QM12FF, and QM11FF) whose function is to match the β functions measured in the EXT diagnostics section. In addition there are 14 quadrupole magnets which transport the beam to the FD that include one focusing (QF1FF) and one defocusing (QD0FF) quadrupoles meant to focus the transverse beam size at the IP. The last nine quadrupoles of the EXT beam line plus the transport quadrupoles of the FFS are referred to as QEA magnets. Three bending magnets, namely B1FF, B2FF, and B5FF, generate the required dispersion to correct the chromaticity by means of the five normal sextupoles, namely SF6FF, SF5FF, SD4FF, SF1FF, and SD0FF. In addition four skew-sextupoles, namely SK1FF, SK2FF, SK3FF, and SK4FF, have been installed in the FFS [31]. Figure 1.6 shows the $\beta_{x,y}$ and η_x functions along the FFS beam line [28].

- **Interaction Point (IP)**
  The ATF2 focal point is called an interaction point (IP) by analogy with particle

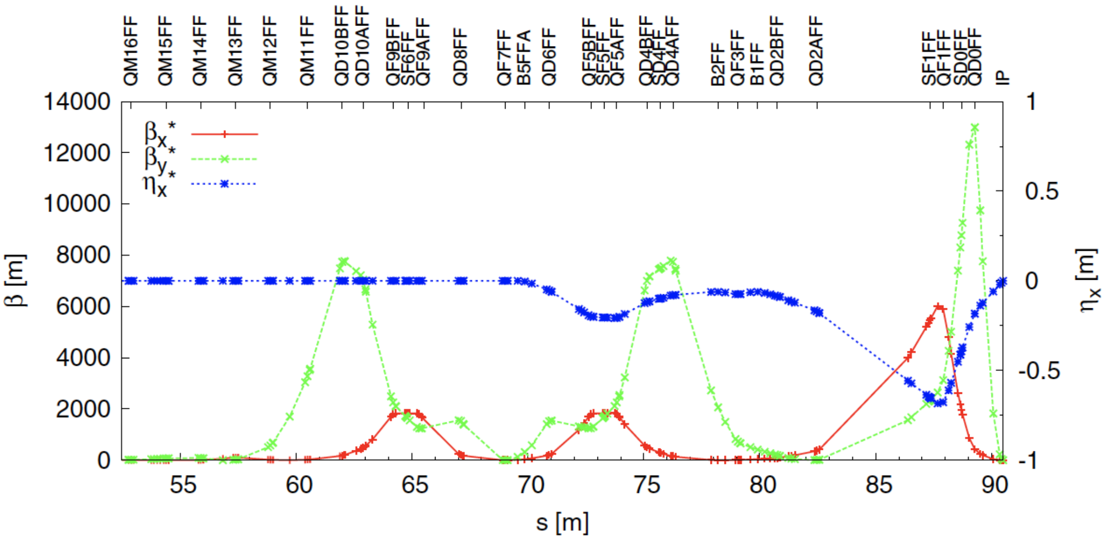

FIGURE 1.6: The $\beta_{x,y}$ functions and the η_x function for the ATF2 nominal lattice throughout the ATF2 final focus line (figure taken from [23]).

colliders. In fact, the ATF2 provides just one particle beam, so no collisions occur there. Instead, the ATF2 performance is verified by measuring the IP beam sizes using the so-called Shintake monitor [32, 33]. It is an interference monitor where two laser beams cross in the plane transverse to the electron beam in order to form a vertical interference pattern, see fig. 1.7. The fringe pattern vertical distribution is modified by changing the phase of one laser-path in the optical delay line. The beam size is inferred from the modulation of the resulting Compton scattered photon signal detected by a downstream photon detector, see equation:

$$\begin{aligned} M &= C\,|\cos\theta|\, exp\left[-2(k_y\sigma_y)^2\right], \\ k_y &= \pi/d, \quad d = \frac{\lambda}{2\sin(\theta/2)}, \end{aligned} \tag{1.1}$$

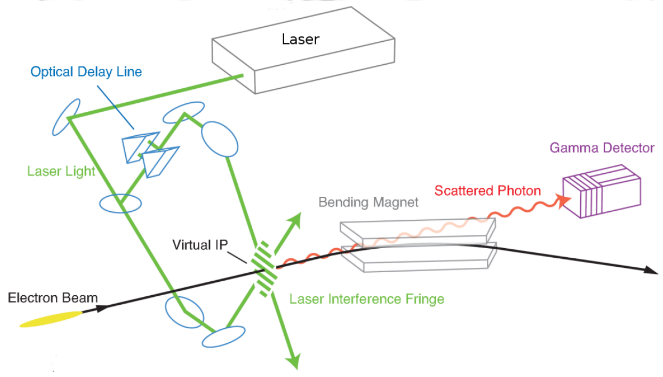

FIGURE 1.7: Shintake monitor schematic design. The electron beam interacts with a transverse interference pattern generated by two crossing laser beams. The number of scattered photons varies with the fringe size and the particle beam size (figure taken from [26]).

where C is the modulation reduction factor which represents the overall systematic effect causing a decrease of the observed modulation due to the monitor imperfections, θ is the crossing angle and $\gamma = 532\,\mathrm{nm}$ is the laser wavelength. Three laser crossing angle modes (2-8 degree, 30 degree, 174 degree) extend the dynamic range from 5 µm to 20 nm, see fig. 1.8. Larger beam sizes are measured by a wire scanner installed at the IP. It consists of a carbon wire 5 µm in diameter that when moved across the beam generates bremsstrahlung gamma rays. The number of photons is proportional to the charge of the slice interacting with the wire at each position setting. Profiles are constructed from the number of photons as a function of wire position [34].

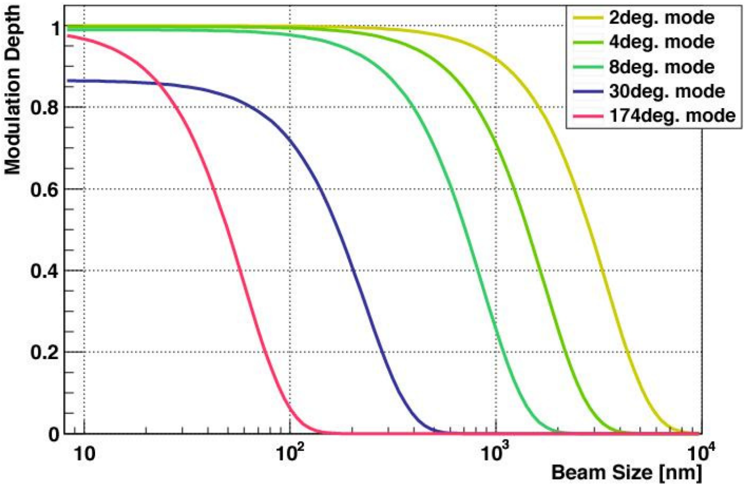

FIGURE 1.8: Modulation depth of the Compton signal as a function of σ_y^* for 5 different operation modes (θ_{ls}=2, 4, 8, 30, 174 degrees) of the ATF2 Shintake monitor (figure taken from [35]).

Octupole magnets for ATF2

Two octupole magnets were added to the ATF2 beamline in 2017 in order to correct the multipolar field errors [23] and quadrupolar fringe fields [36] in the case of the ultra-low β_y^* optics (details in Chapter 4). The octupole magnets design and manufacturing was done at CERN [37, 38]. One of the octupoles is installed in a dispersive location and the other in a non-dispersive location, with a phase advance of 180° between them. The proposed and the actual locations for the octupole magnets are: OCT1FF (weaker octupole and the closest to the IP) between QD2AFF and SK1FF and OCT2FF (stronger octupole and furthest to the IP) between QD6FF and SK3FF.

Chapter 2

Beam Dynamics in a FFS

2.1 Basic Concepts of Transverse Beam Dynamics

This section contains the main beam dynamics concepts which are used in this thesis. Figure 2.1 shows an illustration of the coordinate system. Each particle at any location along a beam transport line is represented by a point in a six-dimensional phase space co-moving with the reference particle with coordinates x, x', y, y', z and δ_p, where x, y and z coordinates refer to the horizontal, vertical and the longitudinal coordinates respectively. The x' and y' coordinates are the horizontal and vertical slopes defined as $x' = \frac{dx}{ds}$ and $y' = \frac{dy}{ds}$ respectively, being s the distance along the reference trajectory. The relation between s and z is given by $z = s - \int v_z(t)dt$ where $v_z(t)$ is the reference particle velocity. Hence z measures deviations on the longitudinal coordinate with respect to the reference particle. Inside of a bending magnet the coordinate s is curvilinear with a radius of curvature ρ_r, while the z coordinate is rectilinear and tangent to the reference trajectory. The δ_p coordinate refers to the particle momentum deviation normalized to the ideal momentum p_0. The reference particle is the particle with the ideal momentum and describes the reference trajectory.

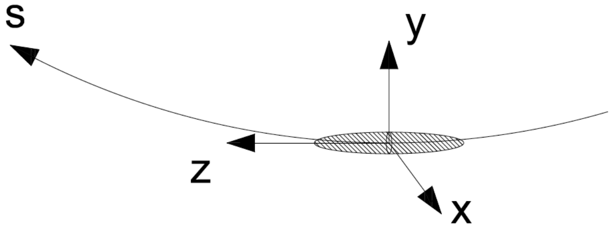

FIGURE 2.1: Illustration of the coordinate system used to describe the motion of an ensemble of particles.

2.1.1 Twiss Functions

The motion of an ensemble of particles along the beam line is usually described by the Twiss functions $\beta_{x,y}(s)$, $\alpha_{x,y}(s)$, $\gamma_{x,y}(s)$ and $\phi_{x,y}(s)$, the dispersion function, $\eta_{x,y}(s)$, and its derivative $\eta'_{x,y}(s)$ which are defined in [39]. The horizontal and vertical emittances $\epsilon_{x,y}$ are defined as the area occupied by the beam in the phase spaces (x, x') and (y, y') over π respectively. The normalized emittance ϵ_N is defined as $\epsilon_N = \gamma \cdot \epsilon$ where γ is the Lorentz factor. The $\beta_{x,y}(s)$ functions characterize the envelope of the beam, while $\alpha_{x,y}(s)$ refers to the divergence of the beam as described by equation (see [39]):

$$\alpha_{x,y}(s) = -\frac{1}{2}\frac{d\beta_{x,y}(s)}{ds}. \tag{2.1}$$

The dispersion takes into account the effect of different deflection of the particles with energy deviating from the reference energy. The product $\delta_p \eta_{x,y}(s)$ determines the offset of the off-momentum particle from the reference trajectory. The x and y coordinates of an off-momentum particle are related to the Twiss functions as (see [39]):

$$x(s)_{(p \neq p_0)} = \sqrt{\hat{\epsilon_x}\beta_x(s)}\cos(\phi_x(s) + \Phi_x) + \delta_p \eta_x(s), \tag{2.2}$$

$$y(s)_{(p \neq p_0)} = \sqrt{\hat{\epsilon_y}\beta_y(s)}\cos(\phi_y(s) + \Phi_y) + \delta_p \eta_y(s), \tag{2.3}$$

where $\hat{\epsilon_x}, \hat{\epsilon_y}$ are the single particle emittance, Φ_x and Φ_y are the initial phases at $s = 0$. The phase function $\phi_{x,y}(s)$ is related to the $\beta_{x,y}(s)$ function as (see Ref. [39]):

$$\phi_{x,y}(s) = \int_0^s \frac{d\hat{s}}{\beta_{x,y}(\hat{s})}. \tag{2.4}$$

Neglecting the synchrotron radiation present in a FFS, the particles travel under the influence of conservative forces. In this scenario Liouville's theorem [40] ensures that the density of the particles in the six-dimensional phase space remains constant [16].

2.1.2 Beam size and Luminosity

Beam Size: The particle distribution of the beam is usually represented by a Gaussian distribution in all six-dimensions. The expected beam size $\sigma_{x,y}$ from the Twiss parameters is given by:

$$\sigma_{x,y}(s) = \sqrt{\epsilon_{x,y}\beta_{x,y}(s) + \delta^2 \eta^2_{x,y}(s)}, \tag{2.5}$$

where $\epsilon_{x,y}$ are the emittances that contain 1σ of the Gaussian particle distribution of the beam and δ is the relative energy spread of the beam. Anyway different beam size definitions may be of interest depending on the purpose of the study, in this sense the core of the beam is of special interest when referring to linear colliders, since it is the part of the beam that largely contributes to the luminosity. The Shintake beam size is used when referring to the vertical beam size at the IP obtained by a laser-interferometer or Shintake monitor (see Section 1.2). Another definition is the rms beam size σ_{rms} defined as the root mean square of the particle distribution. In the following we can find a description of how the beam size is evaluated for the three definitions:

- CORE (σ_{core}): Defined as the Gaussian σ obtained from the Gaussian distribution fitted to the histogram of a bunch of particles. The beam size error is the given error by the fit.
- SHINTAKE (σ_{Shi}): Defined from the convolution between the bunch of particles and the interference pattern of the laser.
- RMS (σ_{rms}): It is evaluated as:

  $$\sigma_{rms} = \sqrt{\int_{-\infty}^{\infty} (u - \bar{u})^2 \rho dv}, \tag{2.6}$$

  where u stands for x, x', y, y' and ρ is the particle density distribution.

The σ_{core} is the smallest value of the three beam size definitions because it almost neglects the tails of the bunch, while σ_{rms} is the largest beam size because it takes into account the tails of the bunch. The three beam size are usually sorted as:

$$\sigma_{core} \leq \sigma_{Shi} \leq \sigma_{rms}, \tag{2.7}$$

the equalities are satisfied when the beam can be represented by a Gaussian distribution, that occurs if the beam size expected from the Twiss parameters equals the σ_{rms} [41].

Luminosity: Luminosity and center-of-mass energy are the key parameters that quantify the performance of a high-energy collider. The luminosity $\mathcal{L}$ in a linear collider is proportional to the square of the number of particles in a bunch (charge of the bunch) N_b^2, the number of bunches per train n_b, the repetition frequency f_{rep} of the trains, and inversely proportional to the effective transverse beam area. Assuming that the two colliding bunches have the same transverse spot sizes, same charge and the two beams collide head-on, $\mathcal{L}$ can be written as:

$$\mathcal{L} = \frac{f_{rep} n_b N_b^2}{4\pi\sigma_x^*\sigma_y^*} H_D = \frac{P_{beam} N_b}{4\pi\sigma_x^*\sigma_y^* E_{cm}} H_D, \tag{2.8}$$

where σ_x^* and σ_y^* are the transverse rms spot sizes at the IP and P_{beam} is the power of the beam. The luminosity is expressed in $\mathrm{cm}^{-2}\,\mathrm{s}^{-1}$. H_D is the luminosity enhancement factor caused by the focusing of the particles due to electromagnetic forces of the opposite bunch. In this report we make the distinction between the total luminosity $\mathcal{L}_{\mathcal{T}}$ and the peak luminosity $\mathcal{L}_{peak}$ (or $\mathcal{L}_{\%}$). The $\mathcal{L}_{peak}$ refers to the luminosity from the collisions with energy larger than 99% of the maximum energy ($\mathcal{L}_{peak} < \mathcal{L}_{\mathcal{T}}$) [42].

2.2 Chromaticity

A quadrupole magnet focuses particles at different longitudinal positions according to their momentum, as it is shown in fig. 2.2 . This effect is referred to chromaticity introduced in Section 1.1. To quantitatively estimate this effect on the beam sizes consider a quadrupole characterized by its normalized gradient K_0. Particles with a relative momentum deviation $\delta_p = \frac{p-p_0}{p_0}$ will see a quadrupole of normalized gradient:

$$K = \frac{e}{p}\frac{\partial B_x}{\partial y} = \frac{e}{p_0(1+\delta_p)}\frac{\partial B_x}{\partial y} \approx K_0(1-\delta_p). \tag{2.9}$$

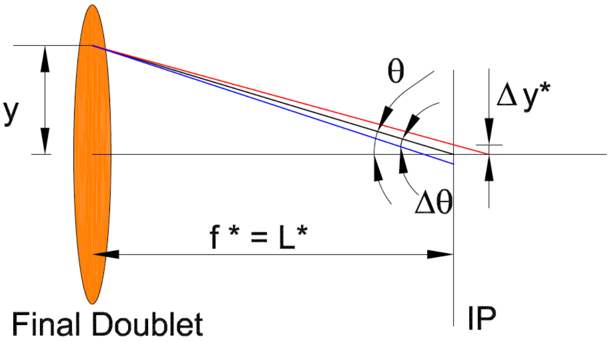

FIGURE 2.2: Scheme of the chromatic aberration induced by the final doublet which is approximate as a unique thin lens of focal length (f^*) defined by $f^* = \frac{1}{K_0 l_q}$ which coincides with L^*. The red, blue and black lines show the trajectory of particles arriving at the FD with the same y coordinate but with larger, smaller and equal momentum respectively than the reference one (figure taken from [37]).

The integrated normalized gradient k of a quadrupole is defined by $k = Kl_q$. If the length of the quadrupole l_q satisfies the condition $l_q \ll (Kl_q)^{-1}$ it is a good approximation to treat the quadrupole magnet as a thin lens of zero length while keeping finite its k. The horizontal and vertical kicks $\Delta x', \Delta y'$ received by an off-momentum particle into a focusing thin lens quadrupole are given by:

$$\Delta x' = -kx = -k_0(1-\delta_p)x = -k_0 x + k_0 x\delta_p, \tag{2.10}$$

$$\Delta y' = +ky = +k_0(1-\delta_p)y = +k_0 y + k_0 y \delta_p. \tag{2.11}$$

Since y is typically of the order of millimetres and L^* is of the order of meters, the IP angle $\theta \approx \frac{y}{f^*} = \frac{y}{L^*}$ as fig. 2.2 shows. Therefore the displacement at the IP can be expressed as $y^* \approx L^*\Delta\theta$. Identifying the terms proportional to δ_p in eq. (2.10) and eq. (2.11) as sources of $\Delta\theta$, it can be obtained that:

$$\Delta y^* \approx L^* k_0 y \delta_p, \tag{2.12}$$

assuming $y \approx L^*\theta$ and considering that $k_0 = 1/L^*$, eq.(2.12) becomes:

$$\Delta y^* \approx L^*\theta\delta_p. \tag{2.13}$$

To estimate the impact of this aberration on the rms vertical beam size it is assumed that there is no correlation between the energy and the angle, eq.(2.13) becomes:

$$\Delta y^*_{rms} \approx L^*\theta_{rms}\Delta_{p(rms)}, \tag{2.14}$$

where θ_{rms} is the rms angle or equivalently the divergence of the beam at the IP, $\Delta_{p(rms)}$ is the energy spread. The relative vertical beam size increase at the IP is related to the design IP vertical beam size σ^*_y as:

$$\frac{\Delta y^*_{rms}}{\sigma^*_y} \approx L^* \frac{\theta_{rms}}{\sigma^*_y} \Delta_{p(rms)}. \tag{2.15}$$

Replacing θ_{rms} by the divergence $\sqrt{\epsilon/\beta^*}$ and since $\eta^*_{x,y} = 0$ and σ^*_y is given by $\sqrt{\epsilon_y\beta^*_y}$, therefore eq.(2.15) can be expressed as:

$$\frac{\Delta y^*_{rms}}{\sigma^*_y} \approx \frac{L^*}{\beta^*_y}\Delta_{p(rms)} \approx \xi_y \Delta_{p(rms)}, \tag{2.16}$$

where $L^*/\beta^*_{x,y}$ is the leading term of the natural chromaticity $\xi_{x,y}$ introduced by the FD, which in a FFS it is the most important source of chromaticity. A more general definition of the natural chromaticity is given by:

$$\left(\frac{\sigma^*}{\sigma^*_0}\right)^2 = 1 + \xi^2\Delta^2_{p(rms)} + O\left(\Delta^4_{p(rms)}\right), \tag{2.17}$$

where the natural chromaticity is identified as the coefficient of the quadratic term in the approximation. In order to avoid this detrimental effect due to the energy spread, the chromaticity needs to be corrected [16].

2.2.1 Chromaticity Correction

We distinguish two classes of aberrations, geometric aberrations and chromatic aberrations. The geometric aberrations come from the betatron oscillations and become significant when the amplitude of the oscillation increases. As we said in the previous section, particles with different energies are focused at different longitudinal positions according to their momentum. When passing through a quadrupole, higher energy particles are focused less than the ideal energy particles and lower energy particles are overfocused. For a correction of this focusing errors we need a sextupole which focuses higher energy particle and defocuses lower energy particles as shown in fig. 2.3. The definition of the chromaticity ξ shows that sextupoles must be located at non-zero dispersion to correct the chromaticity. In order to minimize their strength, sextupoles should be located near quadrupoles where $\beta_x\eta_x$ and $\beta_y\eta_x$ are maximum:

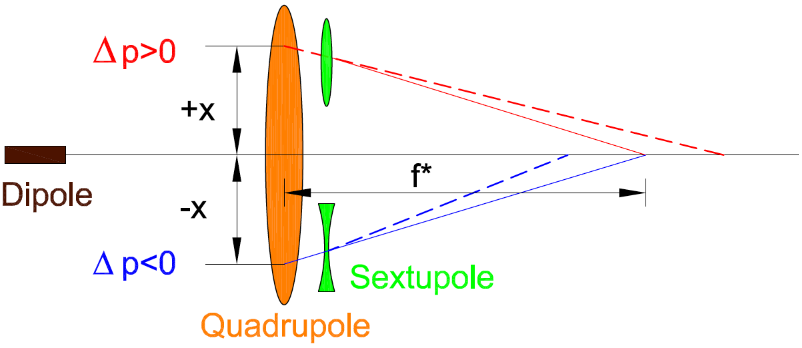

FIGURE 2.3: Chromaticity correction by sextupoles. Dash lines represent particles trajectories without chromaticity correction while continuous lines represent particles trajectories taking into account the effect of the sextupole (figure taken from [37]).

$$\xi_x = \int \beta_x(k_1 - k_2\eta_x)ds, \tag{2.18}$$

$$\xi_y = \int -\beta_y(k_1 - k_2\eta_x)ds. \tag{2.19}$$

Bending magnets generate dispersion and sort the particles according to their energy, then the sextupole provides an extra focusing to particles with different energy (see fig. 2.3). However, the non-linear field of the sextupole generates geometric aberrations which lead to an increase of the beam size. To cancel these geometric aberrations we use sextupoles in pairs separated by π phase advance between them. The kicks inflicted on particles trajectories by a sextupole are given by:

$$\Delta x' = -\frac{1}{2}k_2 l_s(x^2 - y^2), \tag{2.20}$$

$$\Delta y' = k_2 l_s xy. \tag{2.21}$$

To correct the geometric terms generated by sextupoles we use pairs of sextupoles separated by a $-I$ transformation in order to obtain a complete cancellation of geometric aberrations. The kick provided by the first sextupole (which generates the geometric aberration) is compensated by another equal kick at the second sextupole which cancels the geometric aberration (see fig. 2.4). To get this $-I$ transformation between the sextupoles the following conditions between two location s_1, s_2 in the lattice must be matched: $\beta_2/\beta_1 = 1$ and $\Delta\phi_{x,y} = \pi$. It is worth noticing that dipoles introduce emittance growth and energy loss due to synchrotron radiation, the optimization of the FFS needs to balance between these competing effects: need high dispersion to correct chromaticity and small dipole fields to avoid too much synchrotron radiation. Despite the previously described corrections, aberrations remain that deteriorate the performance of the Final Focus due to non-linearities from linear quadrupoles, sextupoles and higher order multipoles [42].

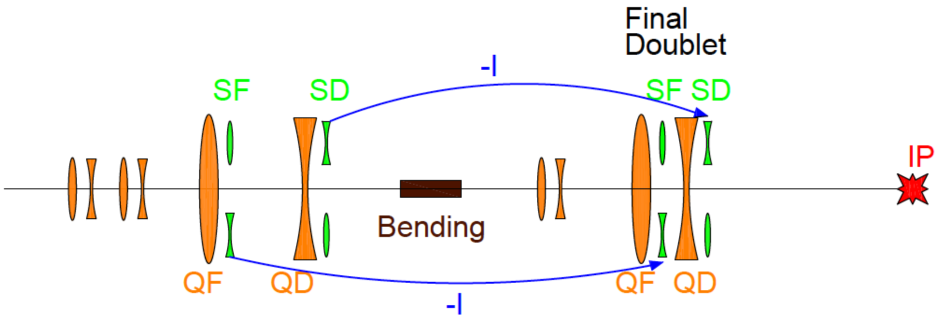

FIGURE 2.4: Optical layout of the FFS based on the local chromaticity correction. QF and QD stand for a focusing and a defocusing quadrupole magnets respectively. SF and SD stand for a focusing and a defocusing sextupole magnet. The unlabelled elements refer to quadrupole magnets meant to transport the beam (figure taken from [37]).

2.3 Maps Formalism

Excluding the sextupoles and higher order multipole magnets the beam transport along the machine is described by a product of the transport matrices R. The global transport of a particle through several magnets and drift spaces is $u_f = Ru_0$ where R is the matrix product of the individual matrices and u_0 and u_f are the initial and final state vectors. The R matrix maps the initial coordinates of the particle $u_0 = (x_0, x'_0, y_0, y'_0, \delta_p)$ to the coordinates at the final position u_f as:

$$u_f = Ru_0 = \begin{pmatrix} R_{11} & R_{12} & R_{13} & R_{14} & R_{15} \\ R_{21} & R_{22} & R_{23} & R_{24} & R_{25} \\ R_{31} & R_{32} & R_{33} & R_{34} & R_{35} \\ R_{41} & R_{42} & R_{43} & R_{44} & R_{45} \\ 0 & 0 & 0 & 0 & 1 \end{pmatrix} \begin{pmatrix} x_0 \\ x'_0 \\ y_0 \\ y'_0 \\ \delta_p \end{pmatrix} \tag{2.22}$$

This matrix formalism is effectively used to describe the linear system. The two dimensional transfer matrix from two longitudinal locations s_0 to s_f in a transport beam line can be written as [43]:

$$\begin{pmatrix} \sqrt{\frac{\beta_{f,i}}{\beta_{0,i}}}(\cos\Delta\phi_i + \alpha_{0,i}\sin\Delta\phi_i) & \sqrt{\beta_{0,i}\beta_{f,i}}\sin\Delta\phi_i \\ -\frac{1+\alpha_{0,i}\alpha_{f,i}}{\sqrt{\beta_{0,i}\beta_{f,i}}}\sin\Delta\phi_i + \frac{\alpha_{0,i}-\alpha_{f,i}}{\sqrt{\beta_{0,i}\beta_{f,i}}}\cos\Delta\phi_i & \sqrt{\frac{\beta_{0,i}}{\beta_{f,i}}}(\cos\Delta\phi_i - \alpha_{f,i}\sin\Delta\phi_i) \end{pmatrix}, \tag{2.23}$$

where i stands for the horizontal or vertical planes, $\beta(s)$ and $\alpha(s)$ are the Twiss functions and $\Delta\varphi_i = \varphi_i(s_f) - \varphi_i(s_0)$ is the phase advance between the final and initial locations, s_f and s_0 respectively. The R_{12} and R_{34} coefficients are of special interest since they relate the initial angular kicks at the start x'_0 and y'_0 with the change in final coordinates x_f and y_f, respectively. However this matrix formalism cannot be applied to describe the higher order elements of the system such as the sextupole magnets. In order to include the non-linear elements a new framework is required. The map is extended by additional transfer tensors (T, U) [44] as suggested in [45]. The coordinates at the final position $u_{f,i}$ are related to the initial ones $u_{0,i}$ by:

$$u_{f,i} = \overbrace{\sum_{j=1}^{5} R_{i,j}u_{0,j}}^{1^{st}order} + \overbrace{\sum_{j,k=1}^{5} T_{i,jk}u_{0,j}u_{0,k}}^{2^{nd}order} + \overbrace{\sum_{j,kl=1}^{5} U_{i,jkl}u_{0,j}u_{0,k}u_{0,l}}^{3^{rd}order} + \overbrace{O(\geq 4)}^{N^{th}order}, \tag{2.24}$$

This map can also be expressed in a more compact way as:

$$u_{f,i} = \sum_{jklmn} X_{i,jklmn} x_0^j p_{x_0}^k y_0^l p_{y_0}^m \delta_p^n, \tag{2.25}$$

where the coordinates x' and y' are replaced by p_x and p_y respectively, being $u_1 = x, u_2 = p_x, u_3 = y, u_4 = p_y$ and $u_5 = \delta_p$. The Polymorphic Tracking Code (PTC) [46] [47] provides the $X_{i,jklmn}$ coefficients for a given beam line defined in the MAD-X environment. The accuracy of the model is determined by the user who defines the maximum order, N_{order}^{MAX}. The sum of the indices j, k, l, m and n in eq. (2.25) is equal to N_{order}^{MAX}. For instance for $N_{order}^{MAX} = 2$ the map coefficients $X_{i,jklmn}$ are evaluated including up to the sextupole components and neglecting the higher multipole components of the beam line. The MAPCLASS code [7] can use the calculation of the $X_{i,jklmn}$ coefficients from PTC or compute them in MAPCLASS2 to transport a distribution of particles with density ρ. The distribution of particles is characterised by its moments $\langle u_i^n \rangle$ which are calculated by:

$$\langle u_i^n \rangle = \int_{-\infty}^{\infty} u_i^n \rho dv. \tag{2.26}$$

The first moment defined by eq. (2.26) can be rewritten as:

$$\begin{aligned}\langle u_{f,i}\rangle &= \int_{-\infty}^{\infty} u_{f,i}\rho_f dv_f = \int_{-\infty}^{\infty} \sum_{jklmn}^{N_{order}^{MAX}} X_{i,jklmn} x_0^j p_{x0}^k y_0^l p_{y_0}^m \delta_{p,0}^n \rho_0 dv_0 = \\ &= \sum_{jklmn}^{N_{order}^{MAX}} X_{i,jklmn} \int_{-\infty}^{\infty} x_0^j p_{x0}^k y_0^l p_{y_0}^m \delta_{p,0}^n \rho_0 dv_0,\end{aligned} \tag{2.27}$$

where it has been assumed that the beam line transport is symplectic, this implies $\rho_f dv_f = \rho_0 dv_0$ along the BDS. The rms beam size is obtained from the quadratic standard deviation of the final density distribution given by:

$$\begin{aligned}\sigma_{f,i}^2 = \langle u_{f,i}^2\rangle - \langle u_{f,i}\rangle^2 = \sum_{\substack{j\,k\,l\,m\,n \\ j'k'l'm'n'}}^{N_{order}^{MAX}} X_{i,jklmn} X_{i,j'k'l'm'n'} \int_{-\infty}^{\infty} x_0^{j+j'} p_{x0}^{k+k'} y_0^{l+l'} p_{y_0}^{m+m'} \delta_{p,0}^{n+n'} \rho_0 dv_0 + \\ - \left(\sum_{jklmn}^{N_{order}^{MAX}} X_{i,jklmn} \int_{-\infty}^{\infty} x_0^j p_{x0}^k y_0^l p_{y_0}^m \delta_{p,0}^n \rho_0 dv_0 \right)^2 .\end{aligned} \tag{2.28}$$

When a large enough value of N_{order}^{MAX} is used, the result is equivalent to the σ_{rms} definition given in Section 2.1.2. According to eq. (2.17) and considering only the purely chromatic contributions to ξ_y the natural chromaticity can be re-written as:

$$\begin{aligned}\xi_y^2 &= \frac{1}{12(\sigma_y^*)^2}\left(X_{y,00101} X_{y,00101} \sigma_{y0}^2 + X_{y,00011} X_{y,00011\sigma_{p_{y0}}}^2 \right) = \\ &= \frac{1}{12}\left(X_{y,00101} X_{y,00101} \frac{\beta_{y0}}{\beta_y^*} + X_{y,00011} X_{y,000111} \frac{1}{\beta_y^* \beta_{y0}} \right),\end{aligned} \tag{2.29}$$

a centred Gaussian beam in the coordinates x, p_x, y, p_y and a rectangular distribution in δ_p is assumed. In the case of the ATF2 lattices, a centred Gaussian beam in the coordinates x, p_x, y, p_y, δ_p is assumed. Again considering only the purely chromatic contributions to ξ_y, the natural chromaticity is expressed as:

$$\begin{aligned}\xi_y^2 &= \frac{1}{(\sigma_y^*)^2}\left(X_{y,00101} X_{y,00101} \sigma_{y0}^2 + X_{y,00011} X_{y,00011\sigma_{p_{y0}}}^2 \right) = \\ &= X_{y,00101} X_{y,00101} \frac{\beta_{y0}}{\beta_y^*} + X_{y,00011} X_{y,000111} \frac{1}{\beta_y^* \beta_{y0}},\end{aligned} \tag{2.30}$$

where β_{y0} and β_y^* are the values of vertical β-function at the beginning and at the IP of the beam line respectively [16].

Chapter 3

Mitigation of Ground Motion Effects using Feed-Forward Control at ATF2

The high luminosity requirement for a future linear collider sets a demanding limit on the beam quality at the Interaction Point (IP). One potential source of luminosity loss is the motion of the ground itself [48, 49]. The resulting misalignments of the quadrupole magnets cause distortions to the beam orbit and hence an increase in the beam emittance [50, 51]. This Chapter describes a technique for compensating this orbit distortion by using seismometers to monitor the misalignment of the quadrupole magnets in real-time [52, 53].

Nowadays, orbit feedback systems [54] and transverse damping systems [55] are used to mitigate ground motion effects and other dynamic imperfections. The beam position is constantly measured via beam position monitors (BPMs) and actuations for corrector magnets are calculated to resteer the beam onto its reference orbit. The main limitation of such systems is that dynamic imperfections can only be suppressed if their frequencies are significantly smaller (factor 20 can be used as a rule of thumb) than the beam repetition rate f_R. This limit is due to considerations about the stability and noise amplification behavior of the applied feedback controllers. In rings, the repetition rate is usually much higher (from kHz to MHz) than the relevant ground motion components (below 100 Hz), and the according beam oscillations can be damped. In linear accelerators, and especially in linear colliders, the repetition rate is much lower than in rings. Important examples are the Compact Linear Collider (CLIC) [15, 56] with $f_R = 50$ Hz, the International Linear Collider (ILC) with $f_R = 5$ Hz, and the Accelerator Test Facility (ATF2) [57, 58] at KEK with $f_R = 3.12$ Hz. Because of these low repetition rates, orbit feedbacks are not sufficient to suppress all relevant ground motion effects and other mitigation methods have to be added for higher frequencies.

The technique of compensation of orbit distortion due to quadrupole motion using feed-forward control [53] is similar in concept to beam orbit feedback but instead of using the position of the beam to determine the deflection to provide, the displacement of the quadrupole is used instead (see fig. 3.1). The primary benefit of such a system is that it can correct frequencies higher than the beam repetition rate. A theoretical framework for such a system is presented in detail in [53].

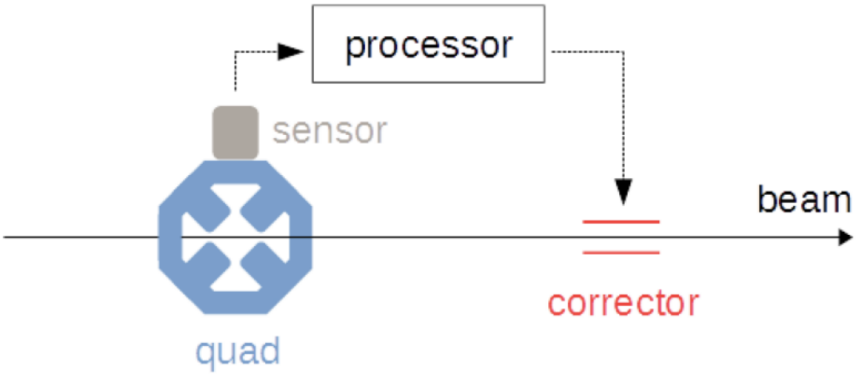

FIGURE 3.1: Schematic illustrating the principle of compensation of orbit distortion due to quadrupole (figure taken from [52]).

To demonstrate the prediction part of the feed-forward mitigation scheme, experimental studies have been carried out at ATF2 (described in Section 1.2). The conditions at ATF2 are very favorable for ground motion studies, since the beam line is relatively sensitive to these effects compared to other machines in operation. The necessary number of vibration sensors and their optimal locations were determined via simulation studies [53].

3.1 Experimental Ground Motion and Feed-Forward Setup at ATF2

The experiments have been conducted at ATF2 in KEK. The ATF2 beam line (see fig. 3.2) is very well suited for ground motion experiments due to its relatively high sensitivity compared to other machines. This sensitivity to ground motion effects originates from the very small beam emittances. Additionally, the available high-resolution BPM system makes it possible to observe the small transverse beam oscillations induced by ground motion [53]. As the beam required for a future linear collider is so much smaller in the vertical axis than in the horizontal, small vertical displacements of the quadrupoles will have a much greater impact on the luminosity compared to horizontal displacements. The analysis presented here thus concerns only the vertical positions of the quadrupoles and the beam [52].

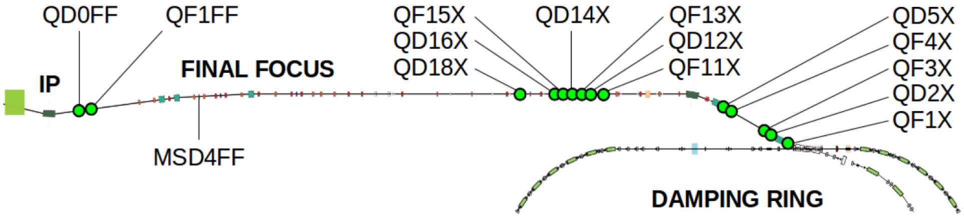

FIGURE 3.2: Schematic illustration of ATF2 beam line.

The experimental setup at ATF2 is depicted in fig 3.1. It consists of three parts:

- Measure position of the quadrupole magnet,
- Calculate a correction (thanks to the processor that calculates the compensatory kick),
- Apply the correction to the beam (stripline kicker).

3.1.1 Ground Motion Hardware

The ground motion hardware consists of three parts: (1) BPM system to measure the orbit jitter; (2) ground motion data acquisition system; (3) synchronization signal. Two types of BPMs are installed: stripline BPMs and cavity BPMs. For the experiment mainly the cavity BPMs are used, with a resolution better than 1 µm [30], since the stripline BPMs are not sensitive enough for the ground motion effects.

The raw BPM signals are processed in real time and the results are published to an EPICS database at the machine repetition rate of 3.12 Hz. This database also contains a measurement of the beam intensity which is logged on a pulse-by-pulse basis alongside the beam position data. The collected data are then used in the offline data analysis [52].

To measure the ground motion vibrations, 14 seismometers (GM) of the type CMG-6T from Güralp have been installed along the beam line by LAPP, Annecy, France. The nominal locations of the seismometers at ATF are indicated in fig. 3.2 [59]. The issue of their exact placement is explained in [52] and the conclusion is that they are optimally located on top of the quadrupole magnets as depicted in fig. 3.3. Each seismometer produces an output proportional to their velocity in both directions perpendicular to the direction of beam travel. These seismometers are specified to measure in a frequency range from 0.03 Hz to 100 Hz [53]. The seismometer outputs are digitized and logged using a National Instruments PXI system provided by CERN. This system consists of a PXI-1042 chassis with a PXI-8108 controller and two PXI-6289 multi-function data acquisition (DAQ) modules to provide the necessary analogue-to-digital converters (ADCs). The measured voltages are logged to file

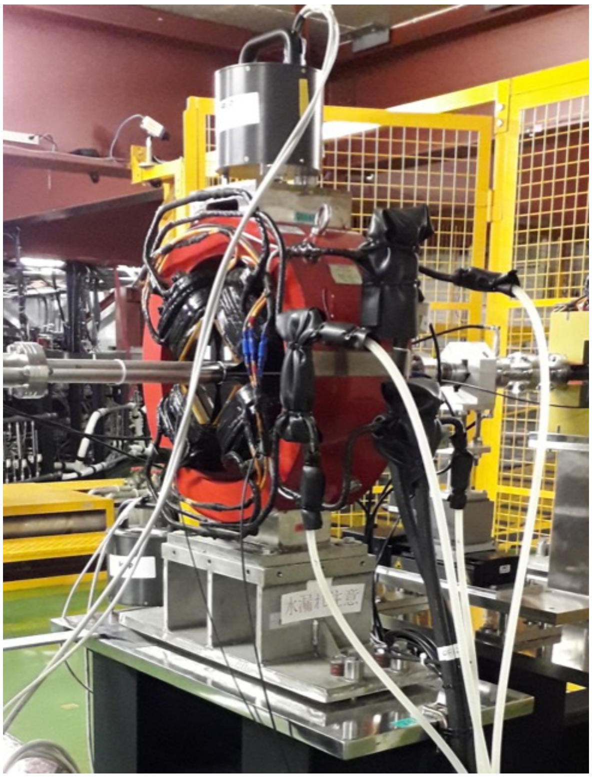

FIGURE 3.3: Photograph of the seismometer mounted on quadrupole QD14x.

and the position is determined by first converting the measured voltage to a velocity using the sensor calibration constant and then integrating the result. A LabVIEW program is used to control the acquisition process.

The stored ground motion data are used in the offline analysis together with the BPM data. It should be mentioned that below 0.2 Hz, the sensor noise contributions are high [60]. Therefore, lower frequencies have been suppressed by applying a second-order Butterworth high-pass filter in the offline analysis [53].

3.1.1.1 Data Acquisition

The BPM measurements are triggered by the beam arrival that occurs at a repetition rate f_R of 3.12 Hz. The ground motion digitization, on the other hand, is triggered by the internal clock of the National Instruments at a repetition rate of 1024 Hz. It is necessary to select the recorded ground motion data that are closest in time to the beam arrival times.

To achieve a secure synchronization the experiment is conducted in the following way. The beam is only turned on after the data acquisitions of the BPMs and ground motion sensors with synchronization signal have already been started. This switching on of the beam is clearly visible in the data of both measurement systems. The ground motion measurements as well as the synchronization signal are recorded. In the offline analysis, these recorded pulses can be detected and the corresponding ground motion data can be extracted (downsampling from 1024 Hz in the case of using the PXI or 1000 Hz in the case of using the cRIO to 3.12 Hz). Before the end of the data acquisition the beam is turned off, which leaves a second clear signature in the measurement data.

3.1.2 Feed-Forward Hardware

The role of the feed-forward processor is filled by a National Instruments CompactRIO (cRIO) system. This FPGA-based unit consists of a cRIO-9064 controller chassis with a cRIO-9205 module for analogue input and a cRIO-9401 module for digital output. The control software is depicted schematically in fig. 3.4.

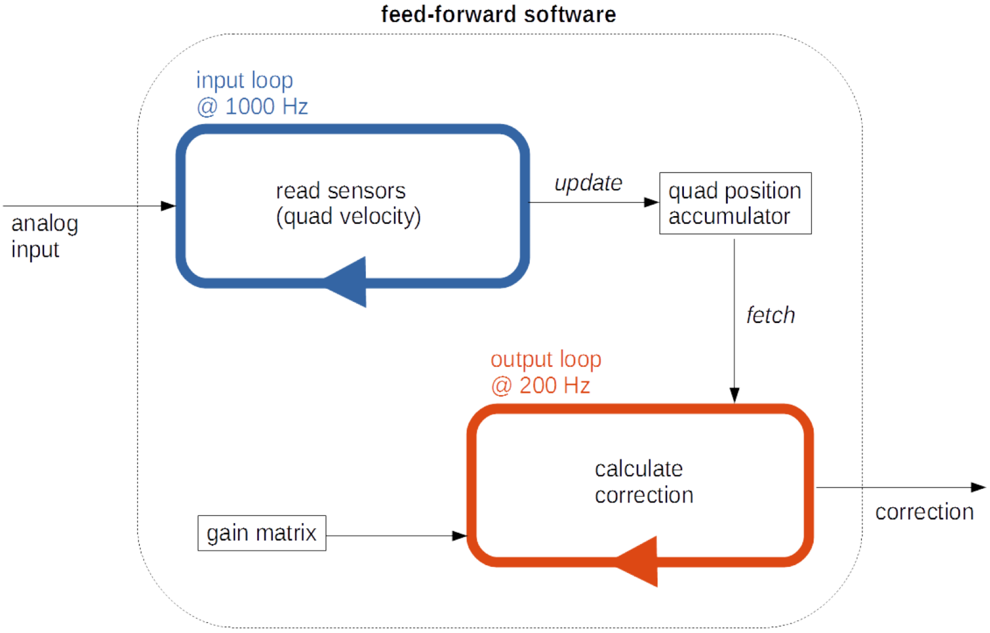

FIGURE 3.4: Schematic of the software running on the feed-forward processor (figure taken from [52]).

The firmware on the FPGA was written in LabVIEW and performs the low-level input and output tasks. The analogue inputs are sampled at a frequency of 1000 Hz and then transferred to the real-time LabVIEW operating system on the cRIO where they are integrated to give the current position of each seismometer. The vector of seismometer positions is then filtered and multiplied by the matrix of gain coefficients to yield the value for the corrective kick. These gain coefficients are determined from a fit of the position at the BPM of interest as a function of the seismometer positions. In the simplest case, the beam position at a single BPM is fitted as a function of the position of a single quadrupole so that there is only one non-zero gain coefficient. The calculated value for the kick is then sent back to the FPGA where it is transmitted as a digital code at a rate of 200 Hz so that the correction is never more than 5 ms out of date. The real-time LabVIEW data acquisition software is also able to store data locally for later transfer to a personal computer for analysis [52].

3.1.2.1 Kickers

The actuator selected for use with the feed-forward system is a simple stripline kicker originating from the SLAC National Accelerator Laboratory [61]. This kicker deflects the beam using the electric field generated when a potential difference is applied across the vertical axis. An ultra-fast, high power amplifier developed by TMD Technologies generates the voltage signals required for this purpose. This amplifier is well beyond the requirements of the feed-forward system but was retained in order to avoid disturbing the existing arrangement of hardware inside the accelerator area. A custom-made FPGA-based control unit ("FONT5 board" [62]) uses signals from the ATF timing system to produce a trigger for the amplifier that is synchronized with the beam arrival time. When used for its original purpose, the FONT5 board also provides a kicker drive signal based on BPM signals. Here it is noted that the FONT5 board was already capable of generating constant kicker drive signals for calibration purposes. The only extra functionality required was thus a means of updating this constant value with the current value of the correction calculated by the feed-forward processor. This was performed by modifying the firmware of the FONT5 board to update the amplitude of the kicker drive signal according to the digital code received over the direct connection to the cRIO system [52].

3.1.3 Data Analysis

The analysis is performed using the numerical computation software Octave [63]. A single data run includes the seismometer position data as a function of time (which represents the position offsets of the quadrupoles) and the beam position data y_m. Both are measured over a period of approximately 15 minutes. The seismometer data is gathered at a frequency of 1024 Hz and the synchronization signal is used to down-sample it to 3.12 Hz to match the BPM data. As an offset quadrupole imparts a kick to the beam proportional to the magnitude of the offset, the analysis fits the vector y_r which is the reconstruction of the beam position as a linear combination of the quadrupole offsets. The potential of the feed-forward system can then be judged by the Pearson correlation coefficient r calculated between this reconstruction of the beam position and the actual measurement:

$$r = \frac{cov(y_r, y_m)}{\sigma_{y_r}\sigma_{y_m}} \tag{3.1}$$

where $cov(y_r, y_m)$ is the covariance of the two variables and σ_{y_r} and σ_{y_m} are the standard deviations of the reconstructed beam position and the measured beam position respectively.

Assuming an ideal system that is capable of completely removing the component of the beam position that is correlated with the positions of the quadrupoles, the jitter reduction factor that would be achieved is:

$$\frac{\sigma_f}{\sigma_i} = \sqrt{1 - r^2} \tag{3.2}$$

where σ_f is the jitter of the corrected beam and σ_i is the jitter of the uncorrected beam. Previous studies of the seismometer performance indicated that the coherence between the measured position for a pair of adjacent seismometers is consistent with zero below a cutoff frequency of about 0.2 Hz [64].

This finding, along with the 100 Hz maximum frequency specified by the manufacturer, motivated the application of a band-pass filter with limits of 0.2 Hz and 100 Hz to the seismometer data before attempting to correlate it with the beam position data. A second-order Butter worth filter [65] is used.

In Section 3.2 the measurements results achieved in the second week of February 2018 operation are presented.

3.2 Measurements Results

The goal of these measurements, done between December 2017 and February 2018, was mostly to reproduce the results published in [52], and then start to go towards a global feed-forward scheme that involves using both kickers at the same time. It is also worth noticing that all the results presented in this section were performed using the ultra-low β_y^* optics (for details see Chapter 4), differently from the ones presented in [52] that were performed with the nominal optics.

3.2.1 Ground Motion Results

Figure 3.5 shows the power spectral density of the full 100 Hz data set from the seismometer at QD2x taken in February 2018 operations. In [52] the results of previous studies carried out with seismometers at ATF2 were shown, where we can identify a series of four narrow peaks at frequencies of 24.14 Hz, 24.29 Hz, 24.40 Hz and 24.60 Hz. In addition, it is also possible to see a peak at 11.55 Hz.

How it is explained in [52], the vibration sources at ∼24 Hz were caused by a pair of cooling water pipes in the QD2x region. However, instead of four narrow peaks and the peak at 11.55 Hz, this newer data (data of 20180208-1659) shows in that region a series of three narrow peaks at frequencies of 24.14 Hz, 24.29 Hz and 24.40 Hz, plus three additional maximum at 15.11 Hz, 8.67 Hz and 6.9 Hz. These peaks are

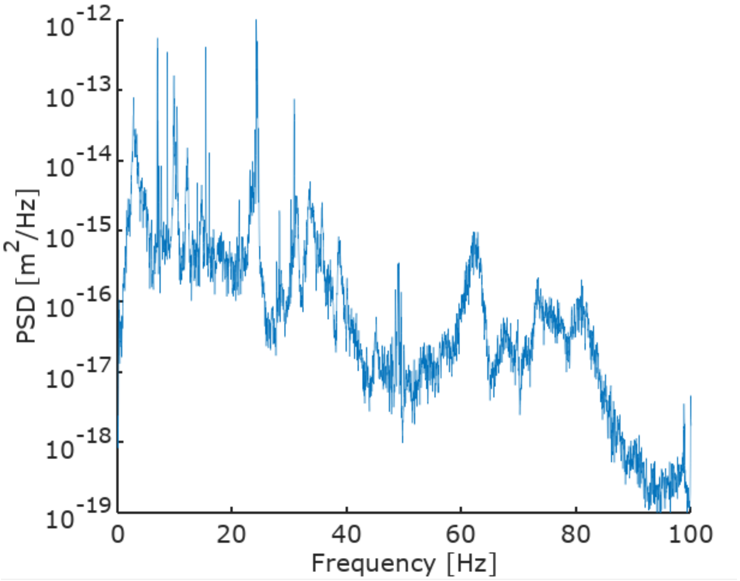

FIGURE 3.5: Power spectral density of the seismometer at QD2x. Files: data-20180208-1659.

clearly visible in fig. 3.6, which shows the region from 5 Hz to 30 Hz in more detail.

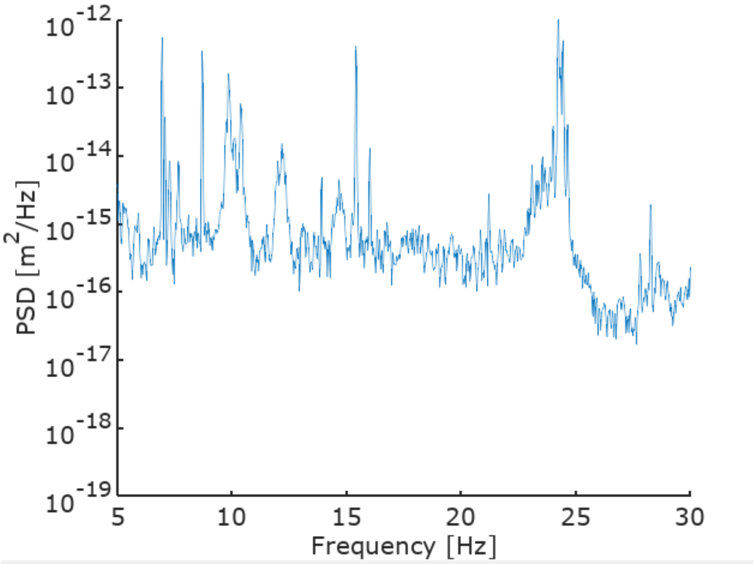

FIGURE 3.6: Power spectral density of the seismometer at QD2x in the 5 Hz to 30 Hz range. Files: data-20180208-1659.

The known frequency response of the seismometers suggests that a band-pass filter with limits of 0.2 Hz and 100 Hz should be applied to the seismometer data at the very least.

To better understand how much the real displacement of the quadrupole is, it is possible to calculate the integrated Root Mean Square for a relative motion in a given frequency range. The Integrated displacement RMS is defined as below, with k_1 and k_2 being the lower and upper bounds of the Frequency range where relative

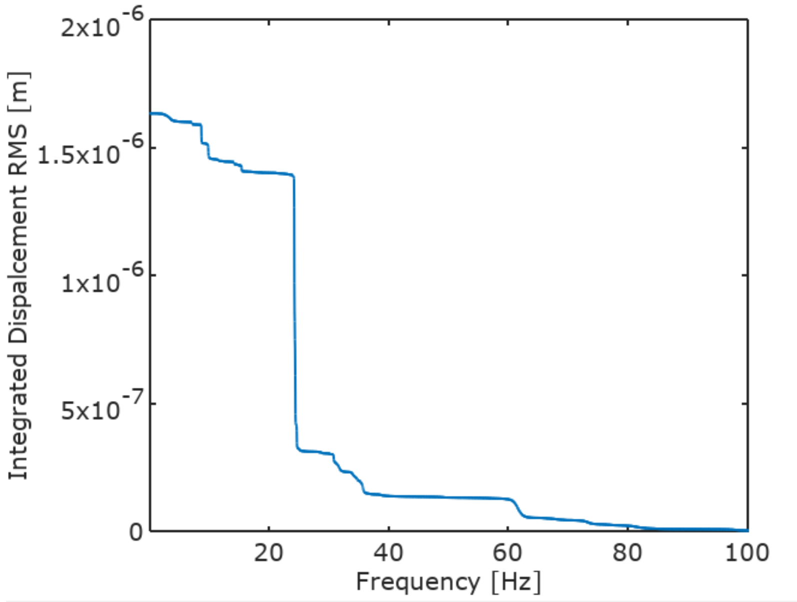

FIGURE 3.7: Integrated displacement RMS of the seismometer QD2x. Files: data-20180208-1659.

motion is integrated:

$$RMS_{int}\ (k) = \sqrt{\sum_{k_1}^{k_2} PSD(k)\Delta f}. \tag{3.3}$$

Assuming Δf equal to 0.2 Hz and considering the PSD calculated before (see fig. 3.5), in fig. 3.7 we can see that the quadrupole rms displacement is around 1.6 µm in frequency range 0-100 Hz.

Figure 3.8 compares the power spectral density of the position of the beam at MQD4BFF (BPM39) to that of the position of the seismometer at QD2x. Note that the power spectral density is calculated using Welch's method [52]. At this point, in order to compare the seismometers results with the BPM ones and to avoid overlap of replicated signals in frequency domain, we need to down-sample the seismometers and the BPM data for a spectra from 0 to 1.506 Hz. Overlap in frequency domain (i.e., aliasing) is avoided if:

$f_{3.12}$ [Hz]	f_{1024} [Hz]
0.43	15.11
0.62	8.67
0.71	24.29
0.80	6.90

TABLE 3.1: Frequencies of peaks from the down-sampled seismometer spectrum with matches in the BPM spectrum ($f_{3.12}$) and their analyzed source frequency (f_{1024}).

$$\frac{1}{T} - f_{bw} \geq f_{bw} \Longrightarrow \frac{1}{T} \geq 2 f_{bw} \tag{3.4}$$

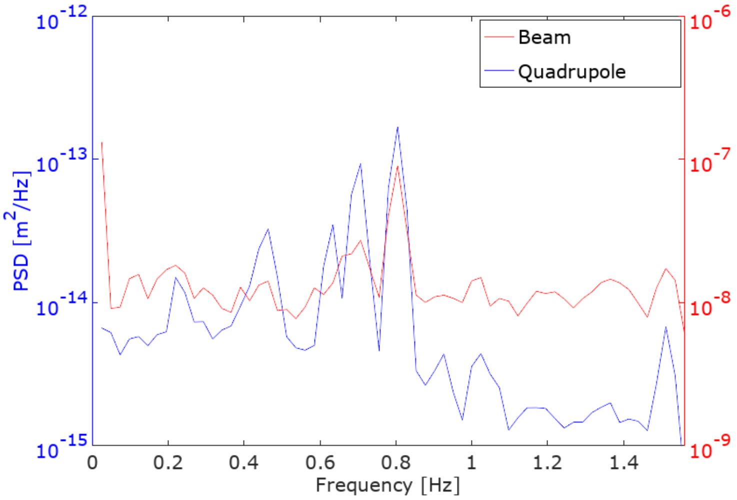

FIGURE 3.8: Power spectral density of the position of the beam at MQD4BFF (BPM39) and the down-sampled to 3.12 Hz position of the seismometer at QD2x. A 0.2 Hz-100 Hz band-pass filter was applied to the seismometer data prior to down-sampling. The axes on the right corresponds to the quadrupole data. BPM39, Files: data-20180208-1659.

where f_{bw} is the frequency width of the signal and $1/T$ is the *Nyquist* sampling frequency that is the minimum that avoids aliasing. The down-sampling process can be extended also for a sequence of N samples (like in our case).

After the down-sampling of the data (the alias frequencies from down-sampling can be found in Table 3.1), in [52] it was found that the dominant 0.85 Hz and 0.95 Hz peaks in the down-sampled spectrum were due to the vibration sources at 24.14 Hz and 11.55 Hz respectively. Instead, from the newer data (see fig 3.8) we can see that the 0.80 Hz and 0.71 Hz peaks in the down-sampled spectrum are due to the vibration sources at 6.90 Hz and 24.29 Hz respectively.

3.2.2 Feed-Forward Results

The feed-forward system was most recently tested in February 2018. Before running the feed-forward, it was necessary to perform a kicker calibration for both kicker 1 (K1) and kicker 2 (K2) in order to see if the kickers are sufficiently decoupled for feed-forward correction. Figures 3.9 and 3.10 show the results of the kicker calibration for BPM20 and BPM39. From Table 3.2 we can see the fit results of the kicker calibration.

Kicker	BPM20	BPM39
K1	0.033	-1.038
K2	0.019	3.395

TABLE 3.2: Calculated kicker calibration constants on 08 February 2018.

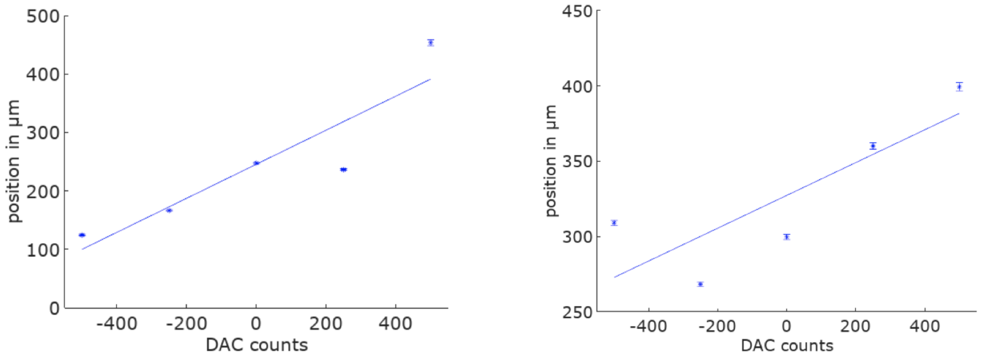

FIGURE 3.9: *Left*: Kicker 1 calibration for BPM39. Files: data-20180208-1416/1427. *Right*: Kicker 2 calibration for BPM39. Files: data-20180208-1200/1210.

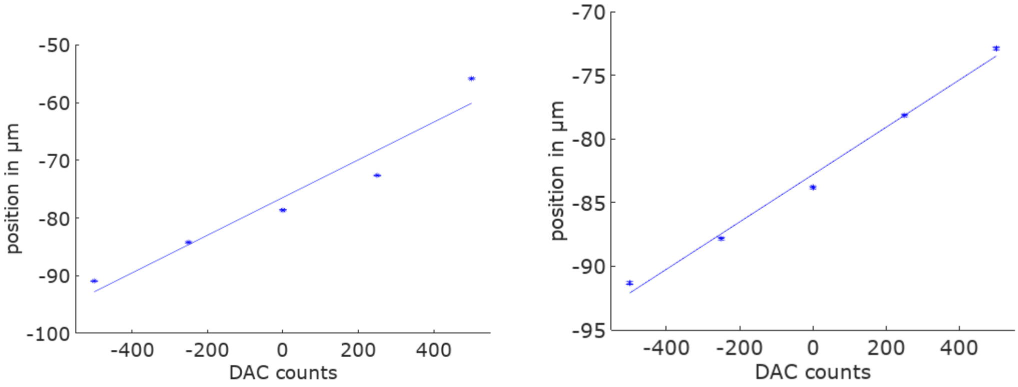

FIGURE 3.10: *Left*: Kicker 1 calibration for BPM20. Files: data-20180208-1416/1427. *Right*: Kicker 2 calibration for BPM20. Files: data-20180208-1200/1210.

Each feed-forward data run consisted of a 90 second record of the beam position data (generated at the machine rate of 3.12 Hz) and a slightly longer measurement of the seismometer data (generated at 1000 Hz). The synchronization signal is then used to obtain a set of approximately 250 simultaneous measurements of the position of the beam at MQD4BFF (BPM39) and the position of the quadrupole QD2x. In order to maximize the performance of the feed-forward system, several control runs were taken in an attempt to accurately assess the correlation between the quadrupole position and the beam position. During the analysis done in [52], it was found that increasing the lower frequency cutoff of the band-pass filter applied to the quadrupole position data significantly increased the correlation. This is explained in fig. 3.11 where we could define the pattern of the filters which have to be used as function of the magnet positions. In fact, all the data with a coherence of 1 Hz (length of 80 m) have to be filtered out. So the frequencies from 0.2 to 2 Hz are really the ones that make the entire machine move, so not useful in the analysis. The feed-forward algorithm was therefore set to use a 2-100 Hz band-pass filter. Figures 3.12 and 3.13 show the quadrupole motion of QD2x and the beam motion correlation (given by the BPM39) for a data recording of 15 minutes and the BPM/GM correlation as a function of the frequency domain for both GM off and GM on at the optimum gain (50).

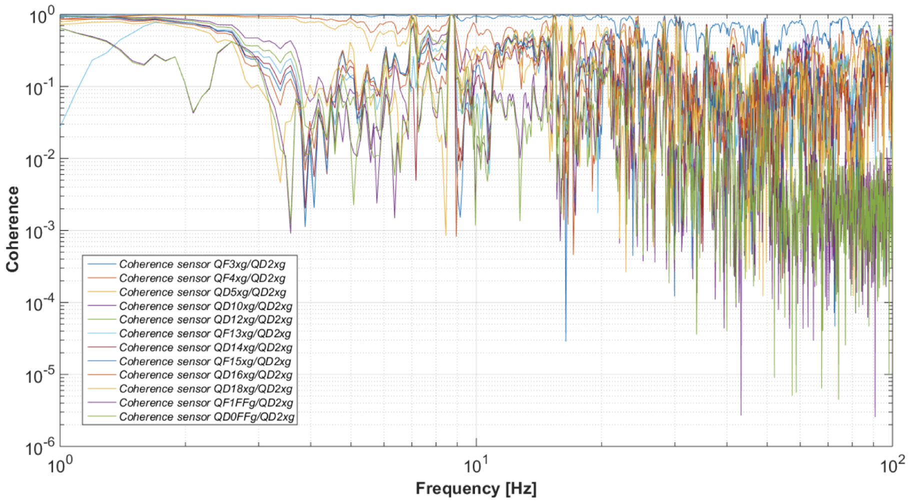

FIGURE 3.11: Coherence vs. Frequency as a function of QD2x. Files: data-20171205. Measurement G.Balik during December 2017 operation.

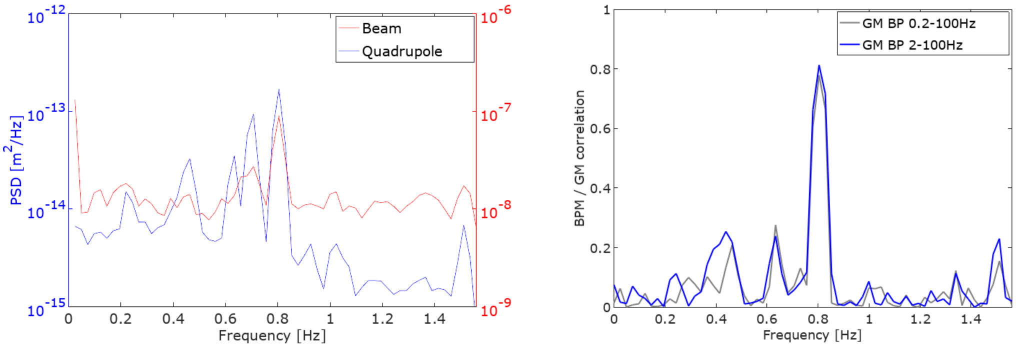

FIGURE 3.12: GM feed-forward affecting PSD and frequency dependence correlation. GM FF off. Files: data-20180208-1659.

Figure 3.14 shows, instead, the correlation as a function of all the BPMs used for the study in order to see that the BPM39 is the one that has the correlation more close to 0 (this is the value that we are looking to reduce the beam jitter) in the optimum filtering case. It is also possible to notice that not all the BPMs are completely functioning at the time of the data taking (there are some missing signals from the BPMs), and this problem is in course of being resolved. Figure 3.15 shows the phase advance between the BPM39, BPM20, Kicker 1, Kicker2 and QD2x and their position along the beamline (the optics used during the February shifts was the ultra-low β_y^*).

Figure 3.16 shows the beam motion with the calibration constant for both Kicker 1 and Kicker 2 and the beam position jitter before and after drift removal in both kickers case. To summarize this results in the fig. 3.16, a more clarifying table was

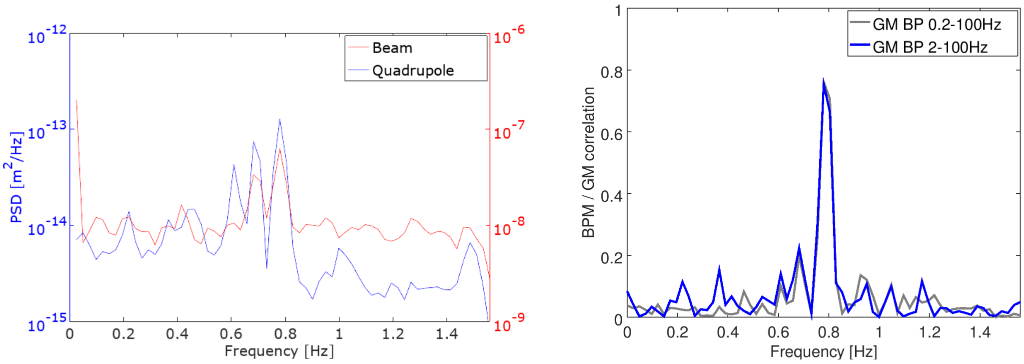

FIGURE 3.13: GM feed-forward affecting PSD and frequency dependence correlation. QD2x to Kicker2 FF on, gain 50 (optimum). Files: data-20180208-1612.

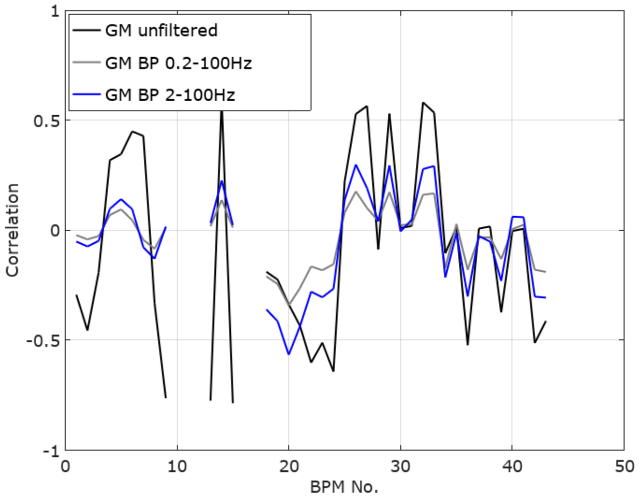

FIGURE 3.14: Correlation vs. Bpm Number for GM unfiltered and filtered data. cRio Channel 2, Files: data-20180208-1659.

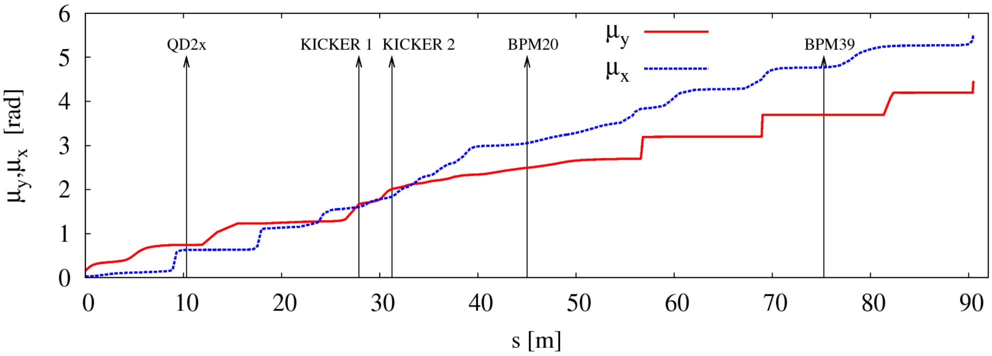

FIGURE 3.15: Horizontal and vertical phase advance as a function of the position along the beamline. The arrows represents the position of the QD2x, Kicker 1, Kicker 2, BPM20 and BPM39 in the beamline.

created. Table 3.3 shows the values of the vertical jitter and the correlation in the zero gain case and the optimal one at BPM39. Similarly to the description in [52] we can say that the feed-forward system was able to remove over 80% of the correlated component of the jitter also in February 2018 beam operations runs with ultra-low β_y^* optics. Furthermore, fig. 3.17 shows the gain parameter g and the corresponding value of the Pearson correlation coefficient r between the reconstructed beam position (y_r) and the measurement (y_m) as it is explained in Section 3.1.3. For both kicker 1 and kicker 2 was done a gain scan from -300 to 300 by steps of 100. The optimal gain (50) was determined only for kicker 2 by a fine gain scan (from 0 to 100 by steps of 20), while for kicker 1 can be seen from fig. 3.17 a potential optimum at 210 (there was no time for a fine scan for kicker 1). The expected behavior (we are looking for a zero correlation in order to find the optimum gain that reduces the beam jitter) was found only for QD2x as the fig. 3.17 shows.

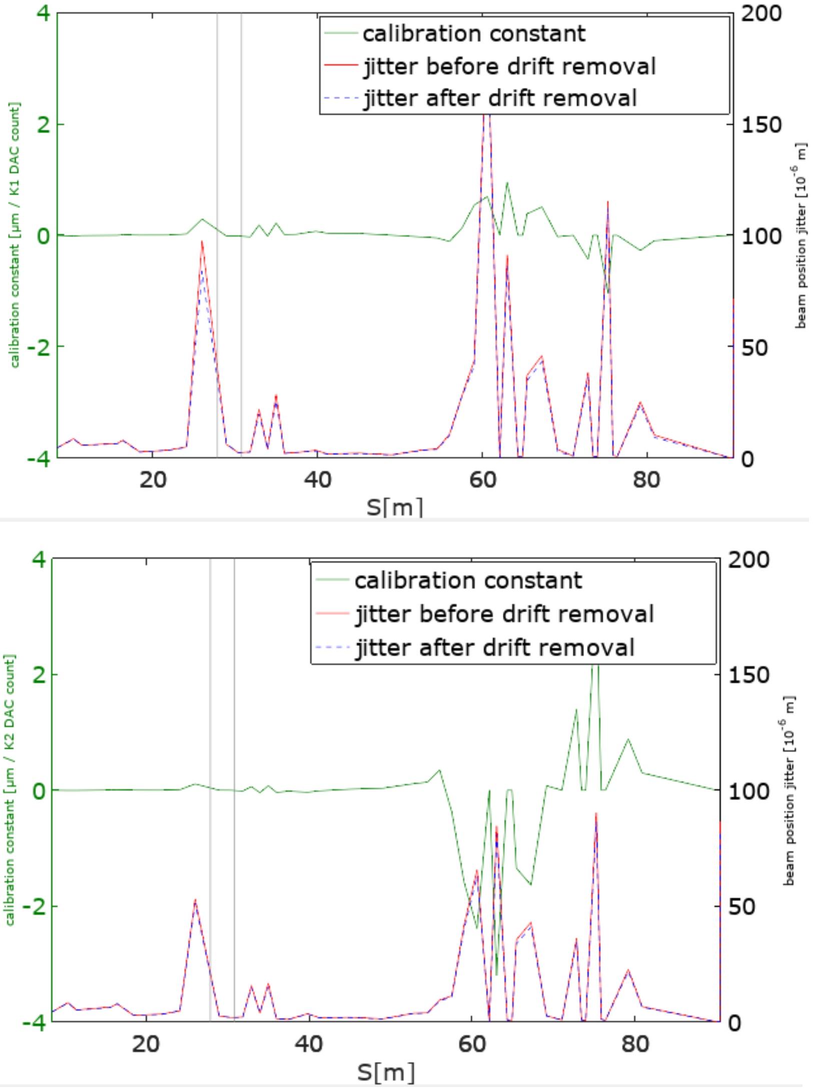

FIGURE 3.16: *Top*: Beam motion (calibration constant) and jitter before and after drift removal for Kicker 1 and BPM39. Files: data-20180208. *Bottom*: Beam motion (calibration constant) and jitter before and after drift removal for Kicker 2 and BPM39. Files: data-20180208.

Gain	σ_b	r
Zero	110.4	-0.23
Optimal	88.8	-0.03

TABLE 3.3: Feed-forward results from the shift on 08 February 2018. σ_b is the average of the vertical jitter of the beam at BPM39, r is the average of the Pearson correlation coefficient between the beam position and the linear reconstruction from the filtered position of quadrupole QD2X. Optimal gain refers to 50.

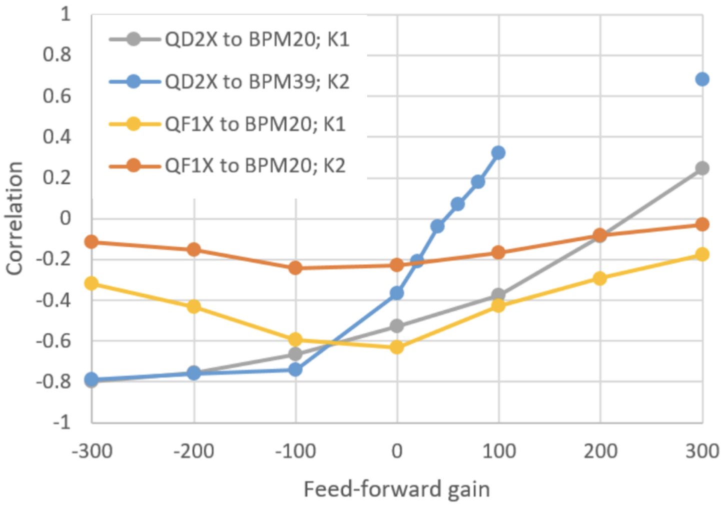

FIGURE 3.17: GM feed-forward gain scan. Correlation between the measured beam position y_m and the reconstructed beam position y_r as a function of the gain parameter g. Files: data-20180208.

Future work will examine the possibility of introducing additional sensors and actuators to the feed-forward system. The actual system involves three sensors (QF1x, QD2x and QF3x) and two kickers (K1 and K2) in the feed forward analysis, so the future challenge would be optimizing up to 2 × 14 gain parameters (include all the 14 sensors) to make the feed-forward a global system in all ATF2 machine. One of the possible path to reach this aim could be to use beam dynamics simulations to: (1) reproduce quadrupole position related to orbit distortion, (2) reproduce kicked orbit, (3) understand orbit response and the required feed-forward gain for orbit correction.

Chapter 4

Experimental Studies on IP Beam Tuning with ultra-low β_y^* optics in ATF2

Feasibility and performance of the ATF2 final focus system with β_y^* values below design has been studied in order to investigate the limits of beam focusing at the IP and the behavior of more chromatic optics as in the CLIC FFS. Three sets of optics were designed in terms of β_y^* (see Section 2.1.1) value: nominal β_y^* (100 µm), half β_y^* (50 µm) and ultra-low β_y^* (25 µm) [66].

The nominal beam optics of ATF2 is a scaled down design of the ILC FFS based on the local chromaticity correction scheme, with equivalent beam energy spread, natural chromaticity and tolerances of magnetic field errors. The vertical beam size was focused to 41±2 nm at the bunch population of 0.7×10^9 at the virtual IP [67]. The achieved beam size is close to the ATF2 target value of 37 nm. The bunch population at the recent ATF2 beam operation is much smaller than ILC due to the strong intensity dependence of vertical beam size at the IP. The candidate of the intensity dependence source is IP angle jitter via wakefield. The IP horizontal and vertical beta-functions (β_x^*, β_y^*) of ATF2 were originally designed to generate the same horizontal and vertical chromaticities as ILC, referred to as $1\beta_x^* \times 1\beta_y^*$ optics. However, since the ATF2 beam energy is much smaller than ILC, the geometrical aberrations of ATF2 and the effect of the multipole errors are also larger. Therefore, in recent ATF2 beam operation, the ATF2 beamline was operated with a 10 times larger horizontal IP beta-function than that of original optics ($10\beta_x^* \times 1\beta_y^*$ optics) in order to reduce the sensitivity to the multipole errors. The ATF2 important parameters, compared with CLIC and the ILC, are presented in the Table 4.1. The local chromaticity correction scheme is considered as a baseline for ILC and a strong candidate for CLIC. However, for CLIC the expected level of chromaticity is higher by about a factor 5.

The ATF2 ultra-low β_y^* lattice is a proposal [68] to test the feasibility for an even larger chromaticity lattice as the CLIC 3 TeV BDS. The ultra-low β_y^* design is an even more advanced optics with a value of β_y^* =25 μm, which represents a quarter of that one of the ATF2 nominal lattice. The expected minimum beam size achievable, after high order optimization of the ultra-low β_y^* FFS design, is 20 nm when optimized with a pair of octupoles.

Operating the ATF2 FFS with lower β_y^* optics would also allow to study the FFS tuning difficulty as function of the IP beam spot size, the impact of the measured multipolar errors, the impact on intensity dependence via wakefield and the compatibility of the IP beam size monitor (Shintake monitor) with a probably enlarged halo. Both the ILC and CLIC projects will benefit from the ATF2 experience at these ultra-low IP betas. The ILC project will benefit from this test by gaining experience in exploring larger chromaticities and facing increased tuning difficulties for smaller beam size.

	ϵ_y [pm]	β_x^* [mm]	β_y^* [μm]	$\sigma_{y,design}^*$ [nm]	L^* [m]	ξ_y ($\sim L^*/\beta_y^*$)
ILC	0.07	11	480	5.9	3.5/4.5	7300/9400
CLIC L^*=3.5m	0.003	7	68	0.7	3.5	50000
CLIC L^*=6m	0.003	7	120	0.9	6	50000
ATF2 nominal	12	4	100	37	1	10000
ATF2 nominal β_y^*, $10\beta_x^*$	12	40	100	37	1	10000
ATF2 half β_y^*	12	4	50	30.5, 25[a]	1	20000
ATF2 half β_y^*, $10\beta_x^*$	12	40	50	26	1	20000
ATF2 ultra-low β_y^*	12	4	25	27, 20[a]	1	40000
ATF2 ultra-low β_y^*, $10\beta_x^*$	12	40	25	21	1	40000

TABLE 4.1: Some of the FFS parameters for ATF2, CLIC and ILC ([a] using octupole magnets). Values of the table taken from [23, 28].

In December 2017 there was the starting of the experimental work towards lowering the β_y^* value by a factor 4 (ultra-low β_y^*) in the ATF2. The objectives of the initial low β_y^* experiments were to gain the experience with the beam operation in the machine, the optics implementation and control, and to identify potential obstacles and address them. The IP beam tuning with ultra-low β_y^* optics was performed in February 2018. In the following sections we describe in detail the machine tuning with the ultra-low β_y^* optics done with 6 machine-shifts (8 hours each) in the last week of February 2018 operation.

4.1 Beam size Optimization for the ultra-low β_y^* optics in ATF2

Ultra-low β_y^* optics allows to decrease the beam size at the IP and therefore study the focusing limits of the ATF2 final focus system. It also increases the strength of chromatic aberrations, that is especially important for developing the FFS for CLIC. The decrease of the β_y^* value causes an increase of the β_y function in the final focus region as shown in fig. 4.1. In consequence, the beam is more sensitive to any beamline imperfections like for instance alignment errors, magnet mispowering, additional dispersion, multipolar field errors, ground motion, wake-fields and others. These effects can cause a significant vertical beam size growth at the IP and so some of them (additional dispersion and multipolar field errors) are corrected with MAPCLASS first.

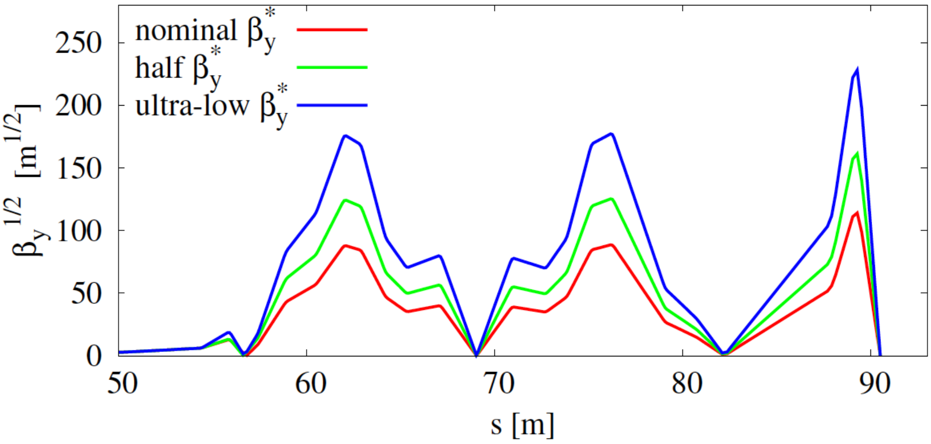

FIGURE 4.1: β_y function along the ATF2 beamline in case of nominal β_y^*, half β_y^* and ultra-low β_y^* optics (figure taken from [66]).

One considered solution to obviate to these errors and imperfections is to increase the β_x^* value in order to lower the β_x function along the FFS and therefore decrease the beam sensitivity to the beamline imperfections in the horizontal plane. However, it causes a horizontal IP beam size increase and therefore it is not a favorable solution for linear colliders as it may reduce the luminosity. In some operations $10\beta_x^*$ (40 mm) has been used as it better corresponds to the expected strength of the optical aberrations in the ILC.

The second considered method is the installation of two octupole magnets in the ATF2 beamline. Some optical aberrations are corrected with the use of sextupole magnets, but detailed analysis of the multipole components at the ATF2 [37] revealed the strong third order contribution coming from the QD0 magnet (last quadrupole before the IP). Also the FD fringe fields give mainly third order kicks which justifies the use of octupole magnets. For all considered sets of optics the IP vertical beam size was minimized using the proposed mitigation methods and the MAD-X model of the machine, that are represented in fig. 4.2. One can see that for the nominal β_x^* value (blue curve) the IP vertical beam sizes are much larger than the ideal minimum beam sizes (black curve) especially for half β_y^* and ultra-low β_y^* optics. Both increasing the β_x^* value by a factor 10 (orange curve) and installing the octupole magnets (red curve) helps in bringing the IP vertical beam sizes close to their limits. The second solution is preferred as it does not cause the horizontal beam size growth at the IP. As a result of this study, the installation of two octupole

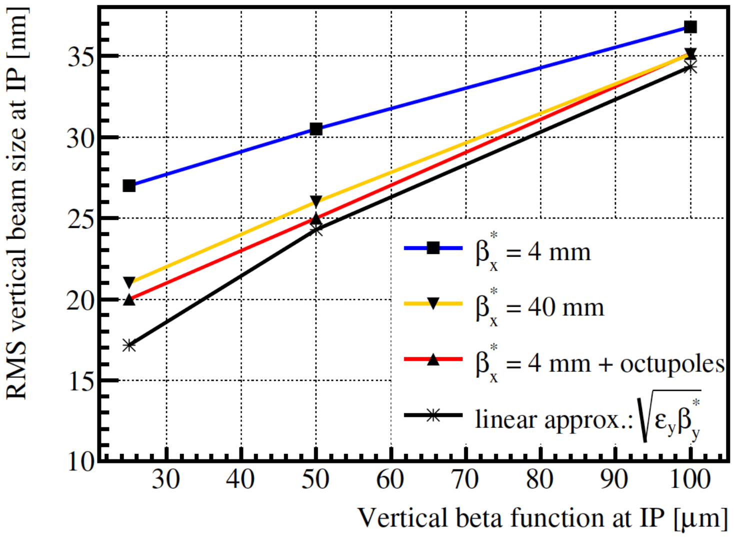

FIGURE 4.2: Expected vertical beam size in the ATF2 for three considered β_y^* values and proposed mitigation methods (figure taken from [66]).

magnets in the ATF2 has been done in 2017 in order to support the ultra-low β_y^* experiment.

4.2 Machine Tuning

Machine tuning is a process of adjusting the beamline parameters in order to obtain beam parameters as close as possible to the design. The general tuning procedure of ATF2 reported in [69] consists of the following steps:

1. Orbit steering: using the orbit correction algorithm, the beam is steered flat using the available EXT line correctors and the FFS magnet movers.
2. Orbit response and jitter modeling: validation of the current online model by cross checking with the orbit response at the BPMs.
3. Beam based alignment (BBA): mostly it refers to classical methods used to correct the beam trajectory along the beamline (for example Dispersion free steering (DFS)).
4. Vertical dispersion and coupling correction: the dispersion and coupling generated in the EXT and FFS is measured and corrected as described in [70].
5. Twiss parameters modeling and emittance measurement: before entering into the IP beam tuning, the measurement of the Twiss parameters is carried out in order to avoid any miss-match between the EXT beam line and the FFS. In addition, the emittance measurement [71] determines the minimum achievable IP spot size according to the given Twiss parameters, as eq. (2.5) shows.

6. Linear and non linear knobs are then applied in order to squeeze the beam to reach the nanometer beam size. They will be explained better in section 4.2.2.

The following section describes the tuning procedures, namely the dispersion matching, coupling correction with linear and non linear tuning knobs and results of the measurements will be presented.

4.2.1 Dispersion Matching

The orbit is corrected using horizontal and vertical steering dipoles to minimize the beam offset at the BPMs located along the FF beamline. After flattening the orbit, dispersion is measured in the ATF2 beamline by changing the beam energy in the damping ring and observing the orbit change at the BPMs. Each measurement involved recording the horizontal and vertical position shifts $\Delta x, y$ of the wire scanner signal distributions for different settings of the damping ring rf frequency and fitting linear dependencies to the data to extract the dispersions [72]:

$$D_{x,y} = \frac{\Delta x, y}{\Delta p / p} \tag{4.1}$$

where $\Delta p / p$ is the momentum shift related to the frequency change Δf by

$$\frac{\Delta p}{p} = \frac{\Delta f}{f_{DR}} \frac{1}{\alpha} \tag{4.2}$$

where α = 0.00214 is the ATF DR momentum compaction factor. During dispersion measurements the damping ring frequency is changed by ±2 kHz leading to a relative beam energy change of about 1.3%. The dispersion correction procedure at

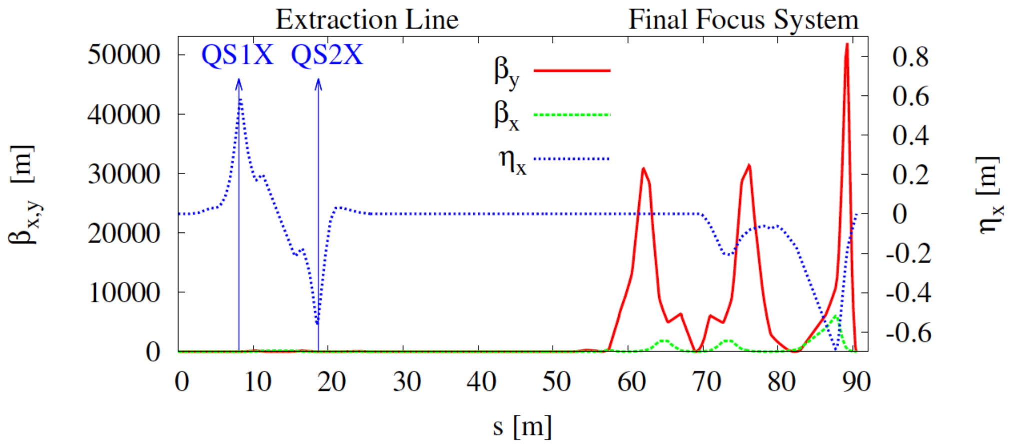

FIGURE 4.3: Optical functions along the extraction and the FF beamline with the location of the pair of skew quadrupoles (QS1x and QS2x) used to correct horizontal dispersion and $< x, y >$ coupling.

ATF2 uses quadrupole strength variations. In order to correct the dispersion along the FFS while not affecting too much other parameters, the quadrupoles used for the correction are located at the peaks of dispersion in the extraction line. The vertical dispersion is corrected using a pair of skew quadrupoles QS1x and QS2x that generates vertical dispersion via coupling from the horizontal dispersion. Their locations are shown in fig 4.3. The same strength variations of QS1x and QS2x are applied during correction. The $< x, y >$ coupling generated by QS1x is canceled by QS2x thanks to the -I transfer matrix in poth planes. The horizontal dispersion is corrected using 2 normal quadrupoles QF1x (located close to QS1x) and QF6x (located close to QS2x). Their strengths are varied independently until matching the design horizontal dispersion from February 2018 beam operation.

Figure 4.4 shows the measured and fitted horizontal dispersion, before and after correction, compared with the design dispersion.

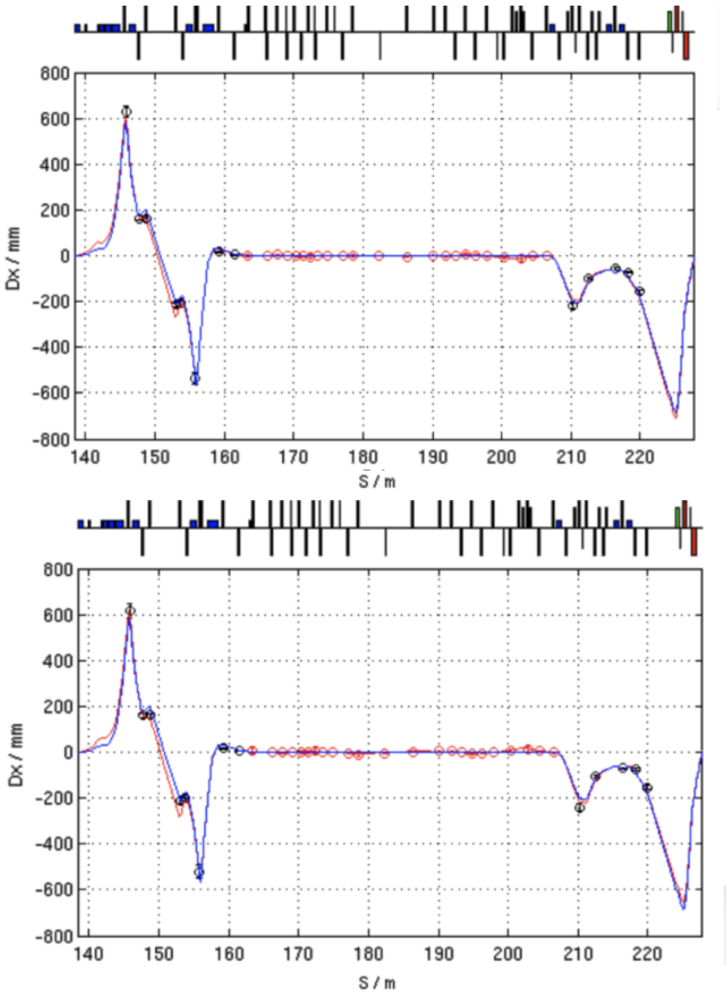

FIGURE 4.4: Measured (black circles), fitted (red) and design (blue) horizontal dispersion in the ATF2 before (top) and after (bottom) correction.

The ATF2 line is by design free of vertical dispersion, so any observed vertical dispersion is anomalous and requires correction. The usual practice is that the vertical dispersion is initially corrected at the mOTR location in order to perform reliable emittance measurements and later the FFS dispersion is minimized with the variation of the difference knob (QS1x and QS2x) as said before, see fig. 4.5.

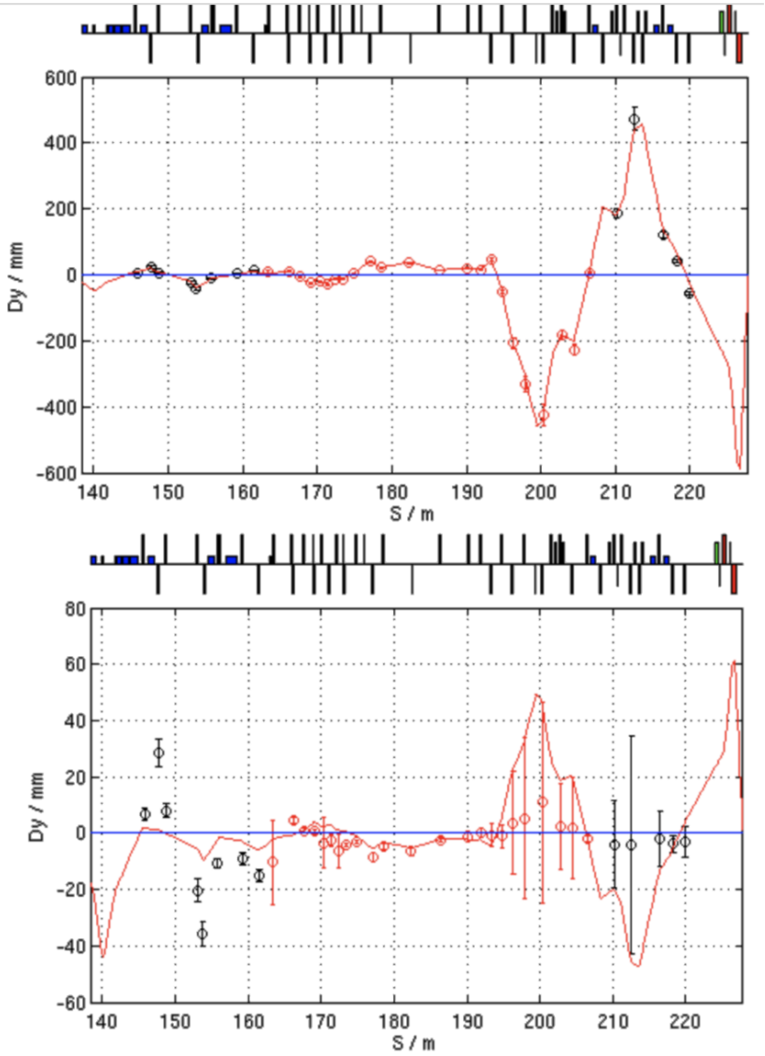

FIGURE 4.5: Measured (black circles), fitted (red) and design (blue) vertical dispersion in the ATF2 before (top) and after (bottom) correction. Please mind the different vertical scales.

4.2.2 Tuning Knobs

In the tuning process, knobs are combinations of multipole magnets displacements meant to control a chosen set of beam aberrations in order to reach the desired beam size at the IP. The knobs are constructed to be orthogonal in order to preserve the correction provided by each knob when scanning the whole set of knobs. While the BBA technique is focused on the beam trajectory correction, the orthogonal knobs method targets aberrations that affect the beam size at the IP. In our case, sextupole displacements are chosen to create orthogonal knobs. Sextupole displacements in horizontal and vertical plane control IP β-functions, waist shift, dispersion and coupling. Each knob ideally corrects only one parameter and the optimum setting of the knob during a correction process is found by fitting a parabola to the measured modulation of the Shintake monitor versus knob strength, so the modulation increases after each knob optimization. The 5 sextupole magnets present in the FFS, namely SF6, SF5, SD4, SF1 and SD0, are used for construction of the orthogonal knobs. Therefore up to 10 knobs can be obtained by horizontal and vertical displacements. The set of knobs to be applied are denoted as: β_x^*, β_y^*, α_x^*, α_y^*, η_x^*, $< x, y >$, $< p_x, y >$, $< p_x, p_y >$, η_y^* and $\eta_y^{'*}$. These knobs are iteratively scanned until the vertical beam size at the IP measured by the Shintake monitor converges to its minimum value.

Knob	Horizontal displacements				
	SF6 [μm]	SF5 [μm]	SD4 [μm]	SF1 [μm]	SD0 [μm]
β_x^*	-5.6	-8.1	0.1	-1.7	-0.3
σ_x^*	0.3	-1.7	-2.7	5.5	7.6
β_y^*	-8.2	5.4	0.4	1.4	0.1
σ_y^*	-0.5	0.4	-9.7	-0.2	-3.1
η_x^*	0.0	1.5	-1.6	-8.0	5.5
Knob	Vertical displacements				
	SF6 [μm]	SF5 [μm]	SD4 [μm]	SF1 [μm]	SD0 [μm]
$< x, y >$	0.4	6.7	1.1	-6.6	-3.0
$< p_x, y >$	-9.7	-0.5	2.1	-1.2	0.9
$< p_x, p_y >$	-0.6	7.2	1.4	6.2	2.9
η_y^*	-0.6	1.2	-7.1	-2.8	6.3
$\eta_y^{'*}$	2.4	-1.1	6.5	-2.8	6.5

TABLE 4.2: Coefficients for each sextupole magnet displacement according to the horizontal and vertical knob (table taken from [16].

4.3 Tuning Results

A detailed description of the experimental tuning results performed during December 2017, February 2018 and May 2018 is given in the following sections.

4.3.1 Tuning Results: December 2017

The last week of December 2017 beam operation was the first long tuning attempt using ultra-low β_y^* optics with a $\beta_y^* = 25\,\mu\text{m}$ at ATF2. The FFS was running with a target of $\beta_x^* = 100\,\text{mm}$ ($25\,\beta_x^* \times 0.25\beta_y^*$ optics) in order to reduce the impact of multipole error fields and to ease the tuning. The ultra-low β_y^* optics requires the use of octupoles to reduce σ_y^* down to 20 nm in the design. The other goal of the ultra-low study is to quantify the benefit on the beam size of using the new pair of octupoles installed at ATF2. In fig. 4.6 it is possible to see the position of the octupoles along the beamline. The $25\beta_x^* \times 0.25\beta_y^*$ optics was applied by using the matching tool

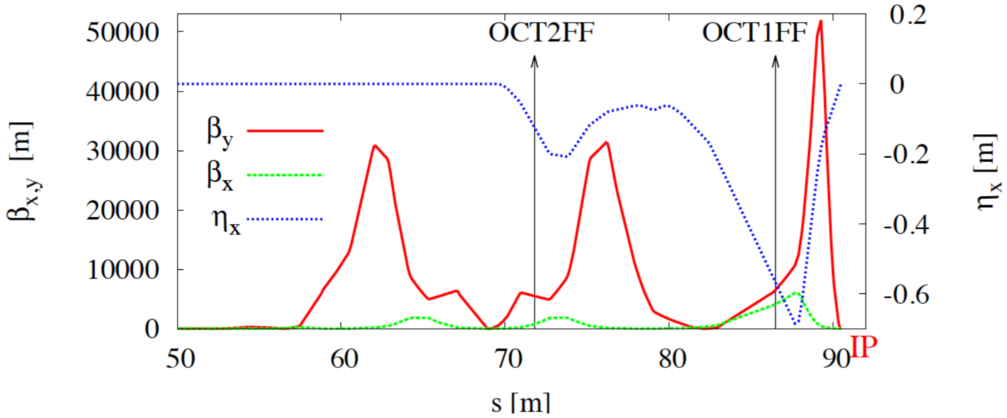

FIGURE 4.6: Ultra-low β_y^* lattice design in terms of β functions and horizontal dispersion. The arrows represents the octupoles position along the beamline.

	k MAD-X model	k in Ampere
kQF19x	3.028	27.50
kQD20x	-2.558	28.74
kQF21x	4.988	56.53
kQM16FF	0	0
kQM15FF	5.666	51.64
kQM14FF	-8.999	-82.65
kQM13FF	5.302	48.51
kQM12FF	-1.371	-12.34
kQM11FF	0.831	7.47

TABLE 4.3: Values of the strengths converted with the SAD program in the control room for February 2018 run.

in the control room, in fact we use the SAD program to convert the strengths of the magnets from the one given by the MAD-X model to have their values in Ampere (see Table 4.3) and then we re-matched the optics by varying QF21x, QD20x (EXT line) and the matching quadrupoles (QM16FF $\longrightarrow$ QM11FF). As the required strength of QM14FF calculated was above the maximum current of the magnet, the upstream QD19x quadrupole had to be used and several optics changes were needed before matching the desired β_y^* measured using QD0FF scan. The multi-OTR used to measure and correct the vertical emittance ϵ_y in the matching section of the FF beamline could not be used during both ultra-low β_y^* tuning operations because 2 of the 4 OTRs were broken. The vertical emittance was thus measured upstream in the

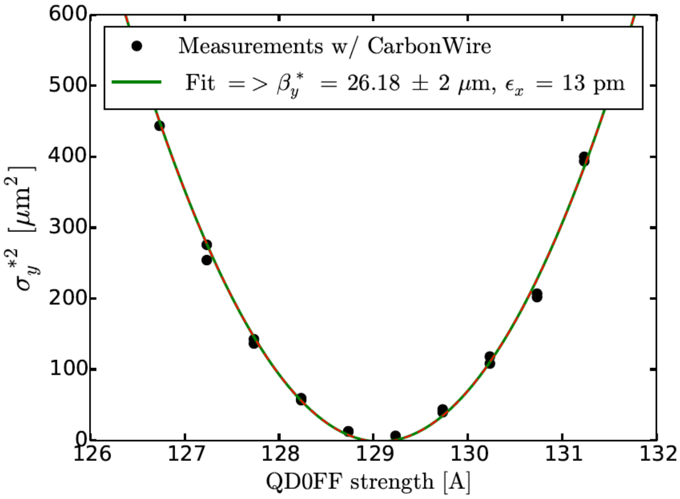

FIGURE 4.7: QD0 scan during the last week of December 2017 beam operation. Vertical beam size as a function of the QD0FF strength.

damping ring but could not be matched at the entrance of the FFS. The measured emittance in the DR of 13 pm and was assumed for the evaluation of the β_y^* value.

Figure 4.7 shows that β_y^* was well matched to 25 µm assuming $\epsilon_y = 13$ pm. However the measurement of β_x^* from QF1FF scan has shown a β_x^* of 85 mm but a fitted ϵ_x^* twice the design value indicating that the scan was biased by large horizontal dispersion at the IP. The measured η_x^* was around 34 mm so, β_x^* was smaller than the one measured. After 5 shifts (5 × 8 hours) of tuning, no clear modulation at the Shintake monitor was found at 174 degree mode. Linear and nonlinear knobs were applied iteratively and sextupoles strengths were changed before the tuning according to our ultra-low β_y^* optics model.

In December 2017 operation the beam size could not be tuned below 100 nm (the minimum beam size reached was 93 ± 12 nm) and that it was difficult to observe the impact of the octupoles when we tuned at 30 degree mode while it was not possible to tune the beam at 174 degree mode as the modulation was close to the noise level ($M \approx 0.1$).

4.3.2 Tuning Results: February 2018

After the first attempt of December 2017, we had five consecutive shifts during the last week of February 2018 beam operations. Before this week we had two more shifts during the second week of February 2018 to find the best optics to use directly for the ultra-low β_y^* week. For the second attempt the 25 $\beta_x^* \times 0.25\beta_y^*$ optics was re-matched in simulation before the run by taking into account the constraints of the FF optics. The sextupoles were re-optimized for the new optics.

Four optics were tested in order to find the best one to use for the second ultra-low β_y^* week. Three of them involve the change of additional upstream magnets in the extraction line: QD16x, QF17x, QD18x and QF19x (+ QD20x, QF21x and QM15FF $\longrightarrow$ QM11FF). The proposed optics were:

- optics with QD16x, QF17x and QD18x unchanged as in December 2017 (same for nominal optics);
- optics with QD16x, QF17x and QD18x changed as in the MAD-X model;
- $\beta_y^* = 15\,\mu\text{m}$ and $\beta_x^* = 100\,\text{mm}$;
- $\beta_y^* = 10\,\mu\text{m}$ and $\beta_x^* = 100\,\text{mm}$.

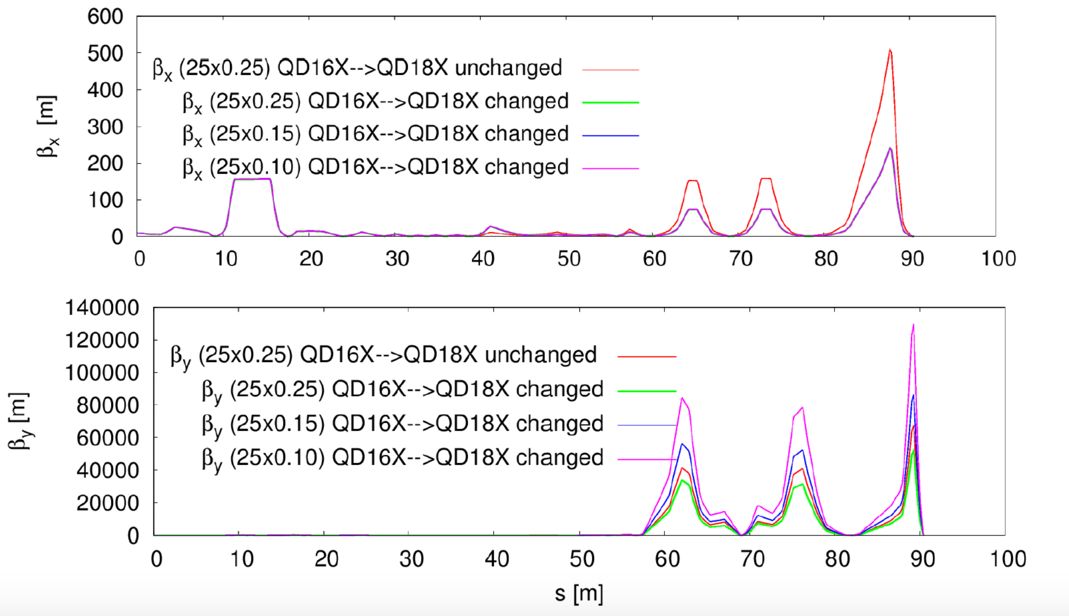

FIGURE 4.8: Horizontal and Vertical beta function β_x, β_y as a function of the position along the beamline for the different optics proposed.

In fig. 4.8 we can see the difference in terms of beta function among the four optics proposed for the ultra-low β_y^* week. For each optics the orbit and the dispersion were corrected and QF1FF and QD0FF scans were performed to estimate the beta-functions at the IP. The dispersion at the IP was measured and its contribution was removed from the measured beam size during the scan. What we noticed is that while the horizontal beta-function falls closely to the model after dispersion correction, the vertical beta-function is systematically higher than the model. This can be seen in Table 4.4 that shows the values of the beta functions at the IP for the four different proposed optics. Smaller β_y^* target (15 µm) was needed to measure β_y^* of $\approx$36 µm but β_x^* was very consistent with the optics model and matched directly $\approx$ 100 mm. This is the reason why we decided to choose the third optics proposed. Residual dispersion was corrected from the fit of the quadrupoles scans. The measured η_x^* was around 3 mm. Figure 4.9 shows the result of QD0FF and QF1FF scans.

Optics	Simulation β_x^*	Measured β_x^*	Simulation β_y^*	Measured β_y^*
$12.5\beta_x^* \times 0.25\beta_y^*$ (QD16x–QD18x unchanged)	50 mm	53 mm	25 μm	(ϵ/β=0.3) ϵ= 13 pm 43 μm
$25\beta_x^* \times 0.25\beta_y^*$ (QD16x–QD18x changed)	100 mm	130 mm	25 μm	(ϵ/β=0.26) ϵ= 13 pm 50 μm
$25\beta_x^* \times 0.15\beta_y^*$	100 mm	132 mm	15 μm	(ϵ/β=0.33) ϵ= 13 pm 39 μm
$25\beta_x^* \times 0.10\beta_y^*$	100 mm	135 mm	10 μm	(ϵ/β=0.36) ϵ= 13 pm 36 μm

TABLE 4.4: Simulation and measured values of the beta functions in the case of the four different optics proposed.

Then, in order to check that the QD0FF scan was not biased by $< x, y >$ coupling which would lead to an over-estimation of the measured divergence, a quick scan of the QS1x-QS2x difference knob was performed (see fig. 4.10).

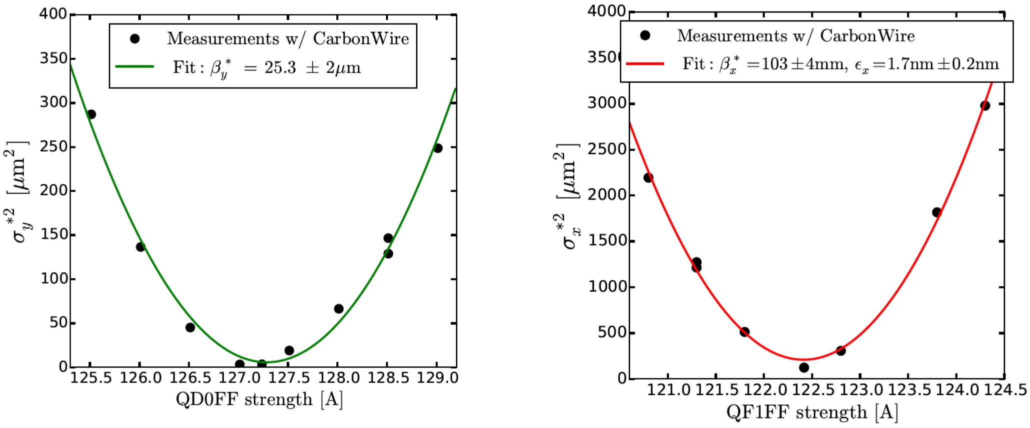

FIGURE 4.9: *Left*: QD0FF scan done during February 2018 operation. Vertical beam size as a function of the QD0FF strength. *Right*: QF1FF scan done during February 2018 operation. Vertical beam size as a function of the QF1FF strength.

The tuning time was reduced compared to December 2017 run due to multiple reasons:

- set up of the ATF2 collimator to reduce the large background from the larger beam size along the FF;
- charge drift coming from temperature variation caused by the cooling system;

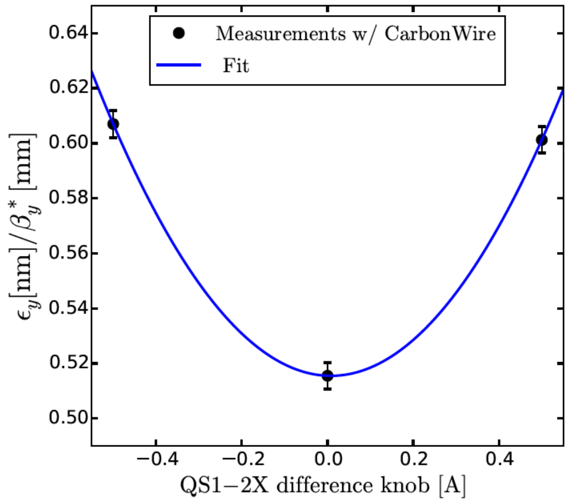

FIGURE 4.10: Divergence squared, measured after QD0FF scan, versus QS1x-QS2x difference knob done during February 2018 operation.

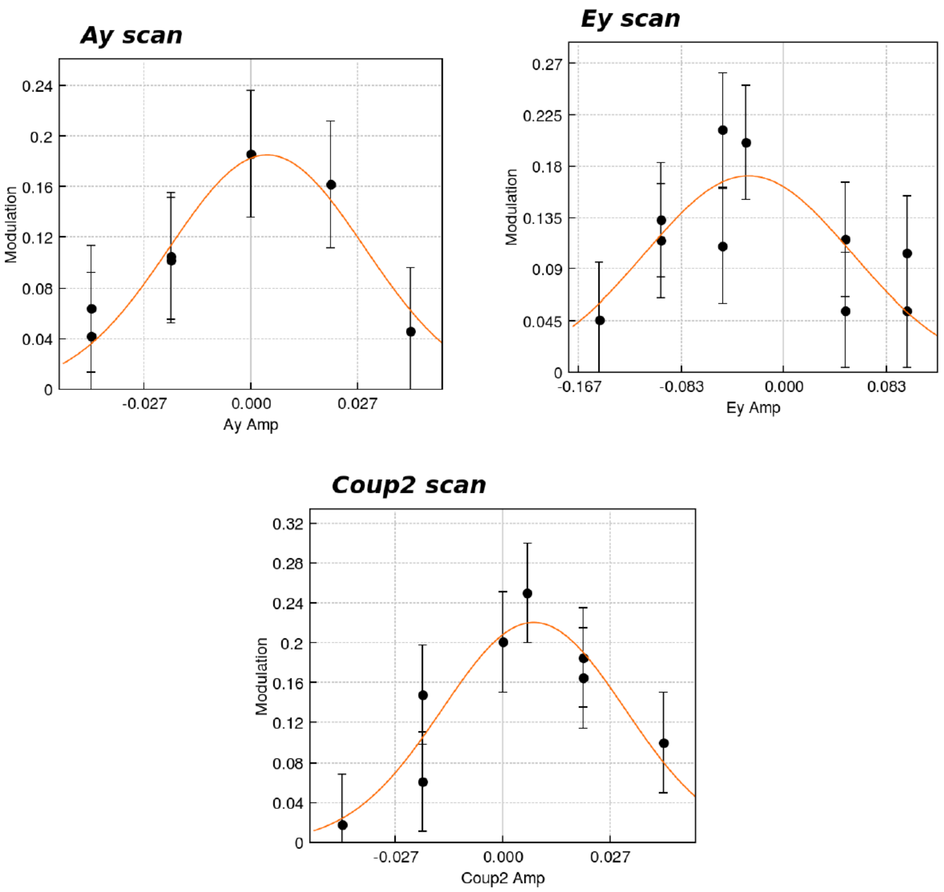

FIGURE 4.11: Linear Knobs Ay (α_y^*), Ey (η_y^*) and Coup2 ($< x, y >$) scans done during February 2018 operation at 30 degree mode with the Shintake monitor.

- rematch and re-tune the Shintake laser after 4 shifts tuning and also the optics because the QF1FF strength was not reset to its original value. This problem led to a large increase of σ_y^*. 1.5 shifts were left for tuning with the Shintake monitor.

Fortunately, we could find a large modulation at 6.4 and 30 degree modes with only two iterations of linear knobs. The ultra-low β_y^* sextupole strength from MAD-X model was applied while we did not apply nonlinear knobs. The skew sextupoles were not set to nominal at this time. Despite the shorter tuning time and without applying 2^{nd} order sextupole knobs or octupoles, the beam size could be squeezed rapidly and modulation could be observed at 174 degree mode. The minimum beam size measured at 174 degree mode was $\sigma_y^* = 64 \pm 2$ nm (see fig. 4.12) by applying only linear knobs (see fig. 4.11) so there was an improvement in the optics and in performance compared to December 2017 operation.

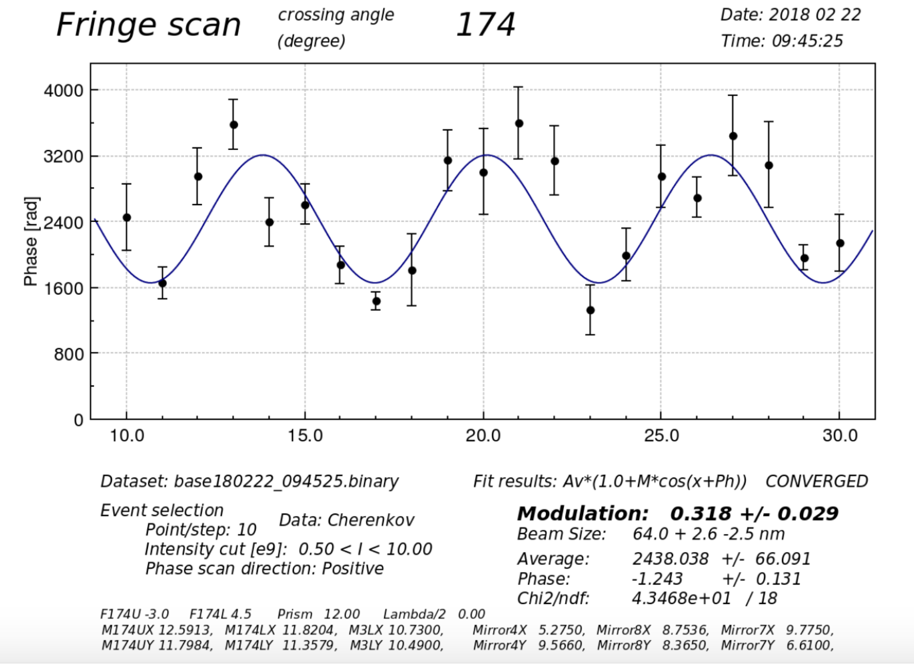

```
Fringe scan    crossing angle    174              Date: 2018 02 22
               (degree)                           Time: 09:45:25

Dataset: base180222_094525.binary          Fit results: Av*(1.0+M*cos(x+Ph))    CONVERGED

Event selection                            Modulation:   0.318 +/- 0.029
      Point/step: 10    Data: Cherenkov    Beam Size:    64.0 + 2.6 -2.5 nm
      Intensity cut [e9]:  0.50 < I < 10.00
      Phase scan direction: Positive       Average:      2438.038  +/-  66.091
                                           Phase:        -1.243    +/-  0.131
                                           Chi2/ndf:     4.3468e+01  / 18
F174U -3.0    F174L 4.5    Prism  12.00    Lambda/2  0.00
M174UX 12.5913,  M174LX 11.8204,  M3LX 10.7300,     Mirror4X  5.2750,  Mirror8X  8.7536,  Mirror7X  9.7750,
M174UY 11.7984,  M174LY  11.3579,  M3LY 10.4900,    Mirror4Y  9.5660,  Mirror8Y  8.3650,  Mirror7Y  6.6100,
```

FIGURE 4.12: Fringe scan that shows the best modulation at 174 degree mode and the best beam size achieved during the February 2018 operation.

To conclude, during the second tuning attempt of the $25\beta_x^* \times 0.25\beta_y^*$ FF lattice, the performance of the system in terms of beam size achieved was improved despite the shorter tuning time and the fact that nonlinear knobs were not applied. These results confirm the suspicion raised during the December 2017 operation about the applied optics. The tuning performance of the updated lattice optimized for the February 2018 run could be further improved if more tuning time is allocated on this optics. All 2^{nd} order sextupole knobs are needed to achieve beam sizes below 30 nm (as in simulation). An important limitation for the tuning of the optics was the absence of multi-OTR (measurements of the emittance and couplings and the matching of the Twiss at the entrance of the FFS). Moreover, it is very important to highlight that with this optics we can observe modulation at 174 degree mode, and during future operations, it would be possible to use and optimize the octupoles for 3^{rd} order correction on the IP beam size.

4.3.3 Tuning Results: May 2018

One of the biggest problem faced during December 2017 and February 2018 runs was the not availability of the multi-OTR software to measure the value of the emittance at the entrance of the FFS. During May 2018 beam operations, the multi-OTR was ready to be operating again.

During this ultra-low β_y^* run it was used the same optics of February 2018 but with the advantage of measuring the emittance. However, the time allocated for the ultra-low β_y^* study was too little to perform a complete machine tuning. So, the results presented here only include the emittance measurements with m-OTR, that provides a first experience for the next ultra-low β_y^* runs in winter operations.

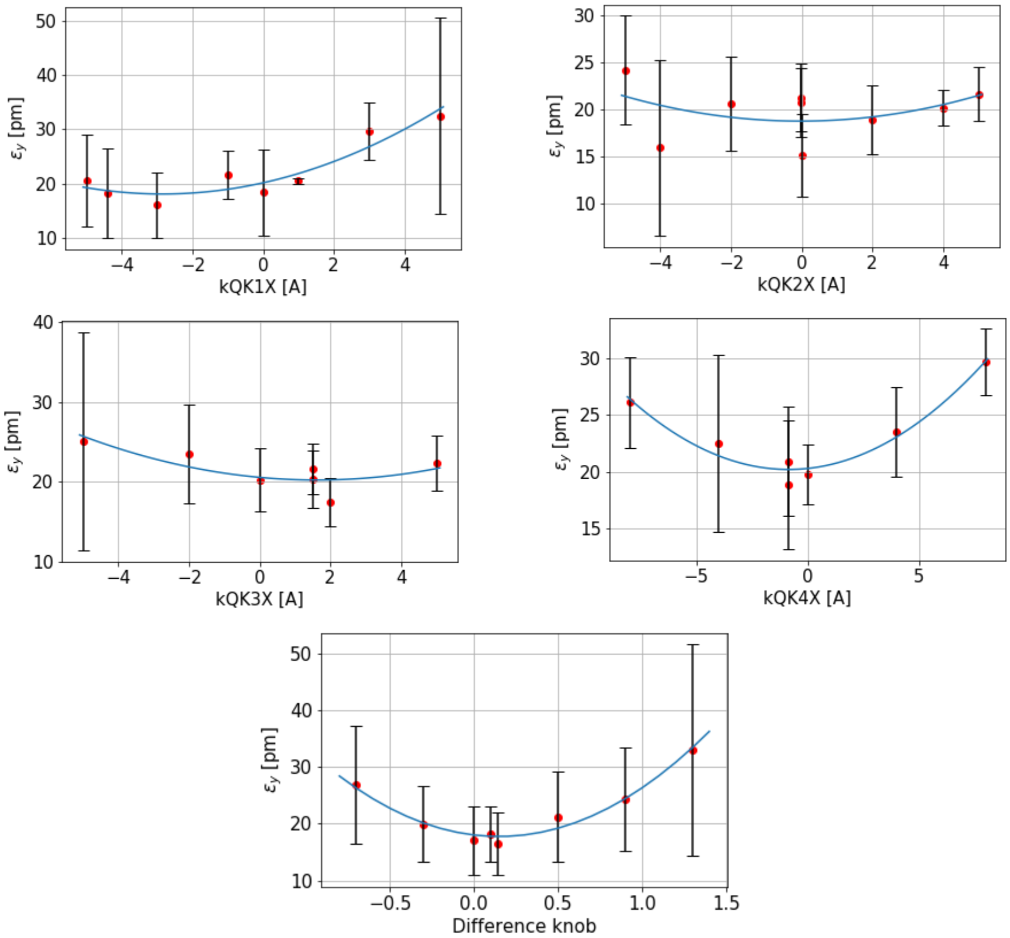

FIGURE 4.13: Scans of the skew quadrupoles and the Δ-knob by varying the emittance done during May 2018 shifts.

Emittance Measurements

After the dispersion matching (explained in Section 4.2.1) in the OTRs region, the dispersion in the vertical plane should be maximum around ±10 mm, a first measurement of the emittance is performed. The emittance evaluated was 23 ± 4 pm. In order to reduce this value, a coupling correction was performed.

Coupling Correction

The xy coupling correction is performed by scanning the strength of four skew quadrupoles (QS1x, QS2x, QS3x and QS4x) in the extraction line and by applying the Σ-knob with the vertical emittance measured by the multi-OTR system being a figure of merit. Figure 4.13 shows the scans performed to correct the coupling.

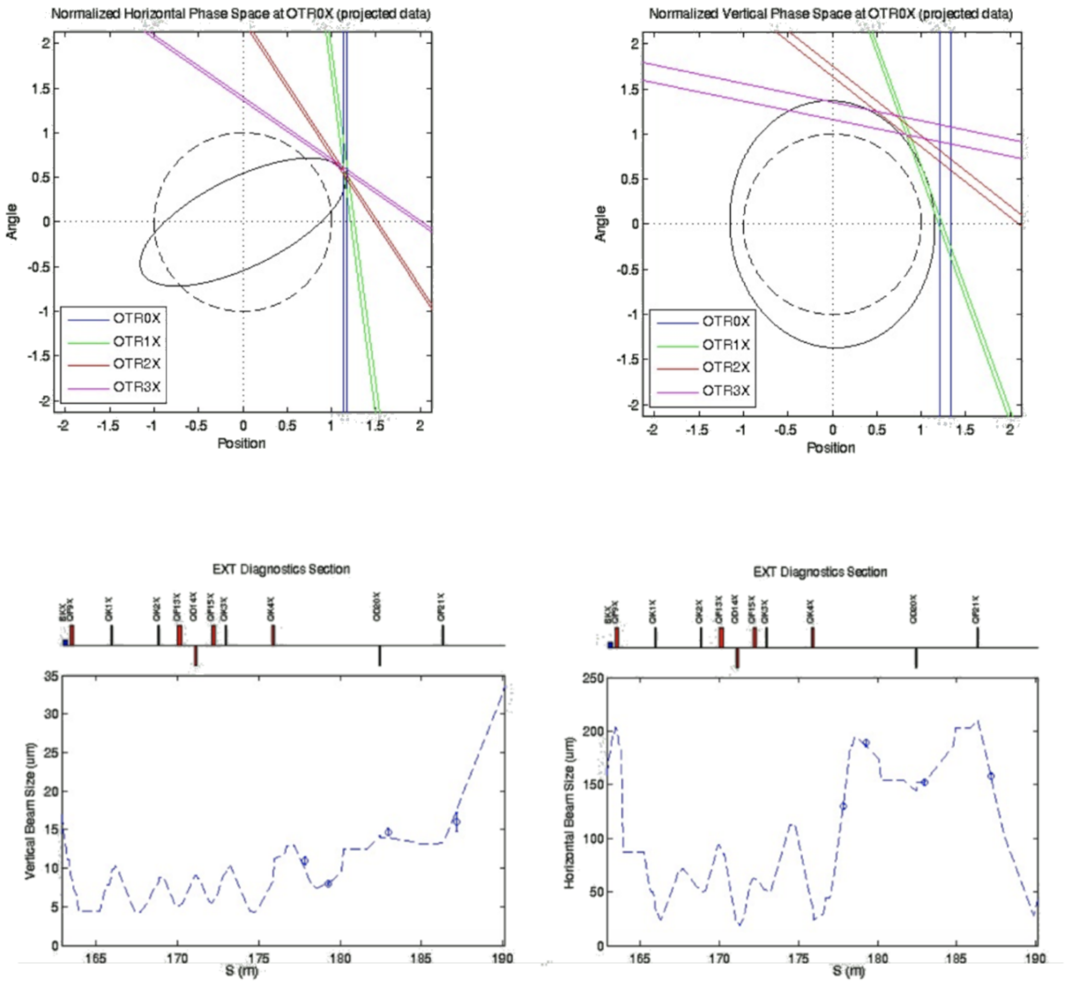

FIGURE 4.14: Fitting of the emittance measurements results obtained using the multi-OTR software during May 2018 shifts.

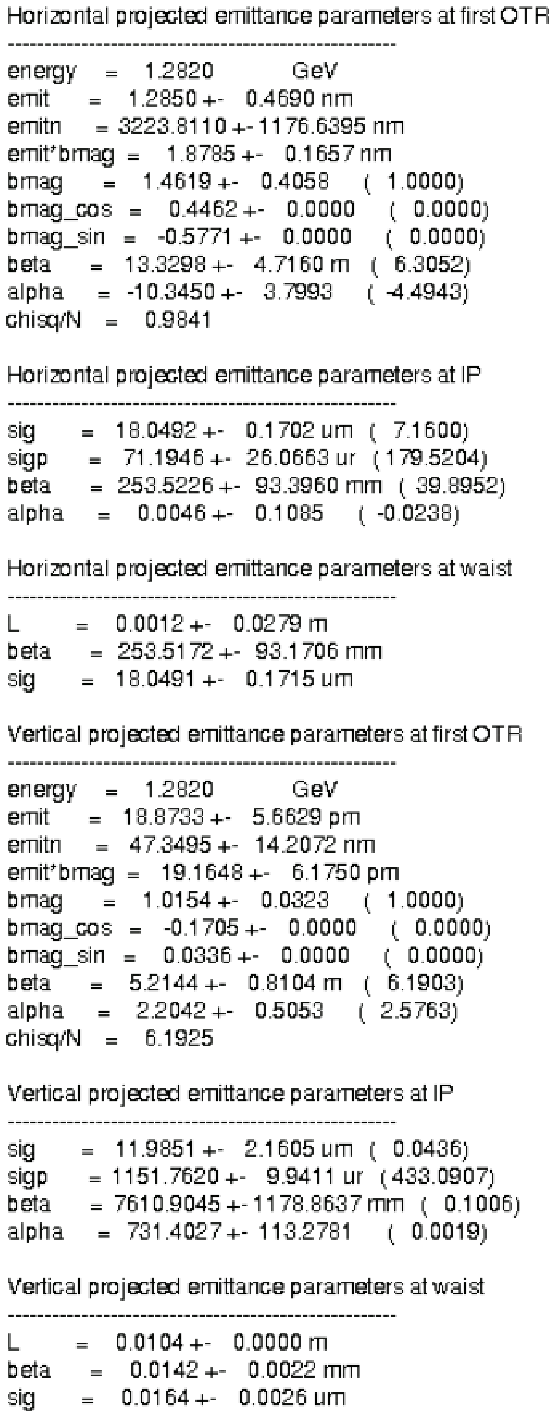

```
Horizontal projected emittance parameters at first OTR
----------------------------------------------------
energy    =   1.2820          GeV
emit      =   1.2850 +-   0.4690 nm
emitn     = 3223.8110 +- 1176.6395 nm
emit*bmag =   1.8785 +-   0.1657 nm
bmag      =   1.4619 +-   0.4058    (  1.0000)
bmag_cos  =   0.4462 +-   0.0000    (  0.0000)
bmag_sin  =  -0.5771 +-   0.0000    (  0.0000)
beta      =  13.3298 +-   4.7160 m  (  6.3052)
alpha     = -10.3450 +-   3.7993    ( -4.4943)
chisq/N   =   0.9841

Horizontal projected emittance parameters at IP
----------------------------------------------------
sig       =  18.0492 +-   0.1702 um (  7.1600)
sigp      =  71.1946 +-  26.0663 ur (179.5204)
beta      = 253.5226 +-  93.3960 mm ( 39.8952)
alpha     =   0.0046 +-   0.1085    ( -0.0238)

Horizontal projected emittance parameters at waist
----------------------------------------------------
L         =   0.0012 +-   0.0279 m
beta      = 253.5172 +-  93.1706 mm
sig       =  18.0491 +-   0.1715 um

Vertical projected emittance parameters at first OTR
----------------------------------------------------
energy    =   1.2820          GeV
emit      =  18.8733 +-   5.6629 pm
emitn     =  47.3495 +-  14.2072 nm
emit*bmag =  19.1648 +-   6.1750 pm
bmag      =   1.0154 +-   0.0323    (  1.0000)
bmag_cos  =  -0.1705 +-   0.0000    (  0.0000)
bmag_sin  =   0.0336 +-   0.0000    (  0.0000)
beta      =   5.2144 +-   0.8104 m  (  6.1903)
alpha     =   2.2042 +-   0.5053    (  2.5763)
chisq/N   =   6.1925

Vertical projected emittance parameters at IP
----------------------------------------------------
sig       =  11.9851 +-   2.1605 um (  0.0436)
sigp      = 1151.7620 +-   9.9411 ur (433.0907)
beta      = 7610.9045 +- 1178.8637 mm (  0.1006)
alpha     = 731.4027 +- 113.2781    (  0.0019)

Vertical projected emittance parameters at waist
----------------------------------------------------
L         =   0.0104 +-   0.0000 m
beta      =   0.0142 +-   0.0022 mm
sig       =   0.0164 +-   0.0026 um
```

FIGURE 4.15: Summary table of the values calculated by the multi-OTR software during May 2018 shifts.

After the coupling correction another emittance measurement was performed and the final value of the emittance resulted to be 19 ± 6 pm. Figure 4.14 shows the fitting results of the emittance measurement and also it is shown an estimation of the beam size at the IP both in horizontal and vertical direction. Furthermore, fig. 4.15 shows the summary table given by the multi-OTR software with all the values of the interesting parameters. In this table we can especially read the emittance value and predicted values of the β-functions at the IP. The step forward would have been the evaluation of the twiss parameters at the IP with the carbon wire scans (see fig. 4.9).

The next steps would be to rerun the same optics and try to do a proper tuning using also the 2^{nd} order sextupole knobs in order to reach the lowest beam size achievable with this optics.

Chapter 5

Crystal Focusing For FFS

The possibility to use single bent crystals for deflection of positively charged particle beams proposed and studied in [73–75] has proven to be very fruitful. Moreover, it has been shown that bent single crystals could be used for focusing beams of positively charged particles because positive charges (e^+ and p) are better channeled than negative particles (e^-) [76–78]. This Chapter is devoted to exploring crystal focusing in FFS, considering the optics aspects using ATF2 as a possible facility for experiments and by evaluating the luminosity for CLIC 1.5 TeV. Conventional beam optics is based on beam focusing with quadrupole lenses whose fields are not at all comparable in strength with the electrostatic field of a bent crystal (the equivalent field is as high as $\sim 1000\,\mathrm{T}$) [75].

It is important to notice that when a beam passes through a bent crystal it is mostly divided into three beams: channeled, dechanneled and volume reflected as shown in fig. 5.1. The volume reflection effect takes place in bent crystals when particles with initial incoming angles greater than the channeling angle, defined as $\theta_{ch} = \sqrt{\frac{2U_0}{pv}}$ (that is, with a transverse energy large enough not to be trapped in an atomic planar channel) have a tangency point with respect to the bent planes inside

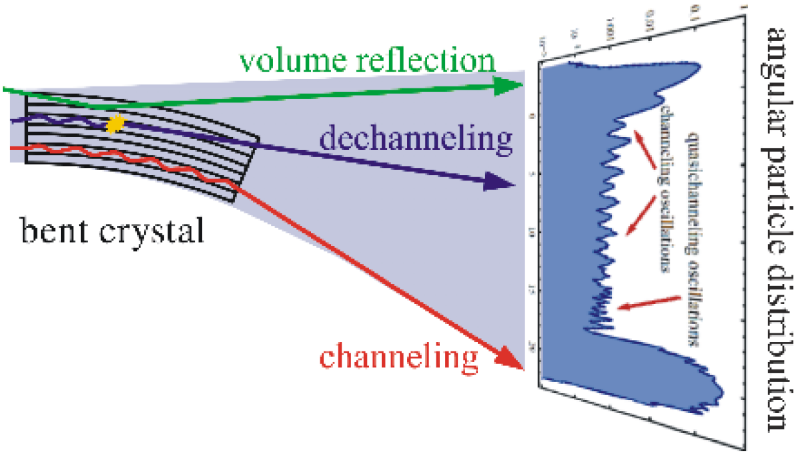

FIGURE 5.1: Sketch of the angular particle distribution of particles passed through a bent crystal (figure taken from [79]).

the crystal volume. A particle that impinges on the crystal with an angle larger than the critical one ($\theta_c = \sqrt{\frac{2U_{max}}{pv}}$, where U_{max} is the maximum value of the potential barrier, evaluated from the critical transverse energy E_C that for example is equal to 6, 12 or 48 GeVcm^{-1} for (110) planes in silicon, germanium and tungsten respectively; p is the particle momentum; and v the velocity) cannot be channeled because of the high transverse momentum: in this case, the angle between the particle and the crystal plane decreases, according to the curvature [80]. So, the volume reflection can be described as the reversing of the particle transverse momentum direction at a turning point in the effective potential [77].

Another important effect in the bent crystal is the radiation emitted by particles (in particular electrons and positrons) in the channeling regime and in the volume reflection regime. The radiation mechanism is a result of the emission by the charged particle accelerated due to the bending of the particle's trajectory in the field of the crystal. This radiation is very similar to the traditional synchrotron radiation of the particle moving in the uniform magnetic field. The radiation emitted by a relativistic particle can be described [81] with the ρ parameter:

$$\rho = 2\gamma^2 \langle v_t^2 - v_m^2 \rangle / c^2 \tag{5.1}$$

where γ is the particle Lorentz factor, $\langle v_t^2 - v_m^2 \rangle$ is the squared mean deviation over the trajectory of the transverse velocity from its mean value v_m, and c is the speed of light. If $\rho \ll 1$ the radiation intensity is the result of interference over a large part of the particle trajectory and depends on the peculiarities of the particle motion. If $\rho \gg 1$, the particle radiates during a small part of the trajectory (its motion direction does not change with the angle $1/\gamma$) and the contributions from far parts can be neglected. The case $\rho \approx 1$ is an intermediate one. In a bent crystal, the planar angle θ changes during the particle motion; if volume reflection occurs (the point where occurs is defined as reflection point), the radiation type during the particle motion is also modified. In other words, far from the reflection point, $\rho \ll 1$ and the radiation is due to coherent bremsstrahlung [82]. Approaching the reflection point, the ρ parameter increases: if the bending radius is significantly greater than the channeling critical one, the mean volume reflection angle θ_{VR} is $\theta_{VR} \approx \sqrt{2}\theta_{ch}$ for positrons and $\theta_{VR} \approx \theta_{ch}$ for electrons [83]. This process is usually described in terms of energy loss instead of radiation intensity [80]. For low-mass particles (electrons and positrons) radiation in a crystal greatly exceeds the usual bremsstrahlung at energies $E > 1$ GeV in the crystal. So to conclude, we can say that for $e^{\pm}$ with $E > 1$ GeV energy loss is dominated by photon radiation; for example for $e^{\pm}$ traveling for 5 mm in the crystal lose 5% energy.

Beam particles can be focused at a point if some specific conditions are fulfilled. The principle of focusing can be illustrated by the diagram in fig 5.2. A cut view of the crystal in the xz projection before it is bent is shown at the top. The particle beam is directed along z axis and it is incident orthogonally on the face of the bent crystal. Under this condition, the particles are easily captured into the channeling mode.

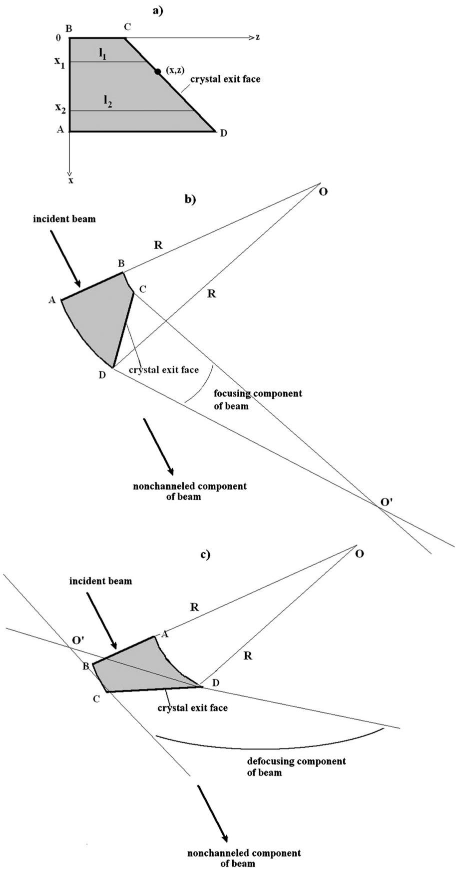

FIGURE 5.2: (a) Geometry of a straight crystal, (b) the diagram showing the principle of beam focusing and (c) the diagram showing the principle of beam defocusing. Points O and O′ correspond to the center of the bend and the focal point, respectively (figure taken from [73]).

As shown before, bent crystals can not only deflect a beam, but also focus it. In principle, there are several ways of doing this. One of them is the focusing of a beam by a thin bent crystal oriented normally to the crystallographic planes. Another possible approach is based on the deformation of planes in a thick crystal when it is compressed. A shortcoming of these two methods is the presence of a background of the unchannelled fraction of the beam. In the middle eighties A.I. Smirnov (LINP) put forward a promising method for focusing a parallel beam into a line and simultaneously deflecting the beam through a considerable angle, so as to form 'clean' focused beams. In this method the surface of the exit face of a bent crystal is shaped so that the tangents to the crystallographic planes on this surface pass through the same line and, consequently, the particles in the deflection plane are collected in a line focus because of the difference between the deflection angles. When the crystallographic planes are bent to form a cylinder of radius R (see fig. 5.3), it is essential to

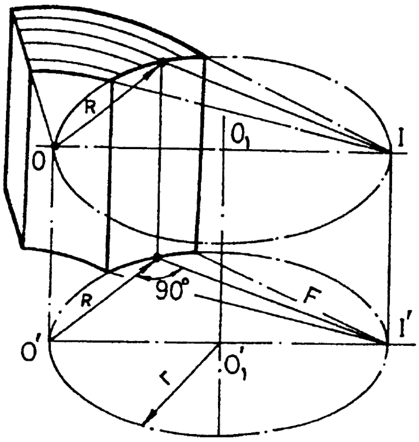

FIGURE 5.3: Principle of focusing of a beam by a crystal. OO' is a line of centres of curveture of the crystallographic planes; $O_1O'_1$ is the axis of a cylindrus of radius r representing the shape which is imposed on the face of the crystal; I and I' are the focal lines where tangents to the bent plane converge (figure taken from [84]).

ensure that the line formed by the centers of curvature OO' is located on the surface of a cylinder of radius r representing the shape of the exit face of the crystal. The focal length f is then $f = (4r^2 - R^2)^{1/2}$. In the case of ideal bending and shaping of a crystal the size of the beam Δx at the focal point is $\Delta x = 2f\theta_c$ and it is governed by its angular divergence within the limits of the critical channelling angle θ_c. Since this critical angle is quite small ($\theta_c = 0.02 - 0.002$ mrad for particles of energies from 100 GeV to 10 TeV in the case of planar channelling in silicon) and the technology used to bend and shape a crystal makes it possible to achieve a focal length of the order of several centimeters, the attainable dimensions of the beam are $\approx 10\,\mu$m for the gigaelectron-volt energies and $\approx 1\,\mu$m for the teraelectron-volt range. The linear magnification in the course of focusing is $q = 2f\theta_c/H$ is the characteristic thickness of a crystal ($\approx$ 1 mm), and it can reach a fraction amounting to, respectively, hundreds and thousands in the two energy ranges [84].

The Chapter is organized as follows. Firstly the implementation of the crystal in MAD-X environment is described for the FFS of ATF2. In the following section simulation results are shown for a design obtained with a bent Si crystal (fig. 5.4) used to replace the last magnet before the IP, referred as QD0FF (the defocusing quadrupole of the FD), and how they are related to β-functions, horizontal dispersion, natural chromaticity and IP beam size. Then simulation results for the luminosity values for CLIC 1.5 TeV are presented.

5.1 Crystal Implementation in the FFS of ATF2

This Chapter reports preliminary studies on the application of a Si crystal on the FFS in ATF2. Two different cases have been studied in simulation:

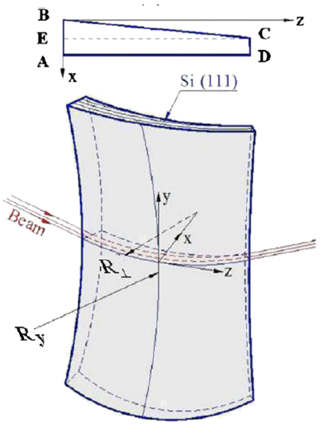

FIGURE 5.4: Example of a bent Si crystal with an edge used in the simulation studies. R_y is the radius of the vertical bending, and $R_\perp$ is the radius of the bending in the horizontal plane, which provides the particle beam bending (figure taken from [75]).

1. Lattice with QD0FF from MAD-X of ATF2, in particular we are referring at the ultra-low β_y^* optics (for details see Chapter 4);
2. Development of a new lattice which includes the Si crystal as a replacement of QD0FF.

The implementation of the crystal in MAD-X and MAPCLASS is done by replacing QD0FF ($L_{QD0FF} = 0.475$ m) with a crystal considered with a thin kick matrix and two drifts (the drifts with L=0.2375 m respectively are necessary in order to maintain the same length of the FFS region since the crystal has been considered to have a zero length), see fig. 5.5. A zoom of the region next to the IP is shown in fig. 5.6 where we can see the L^* values considered in the simulations for both QD0FF and crystal cases.

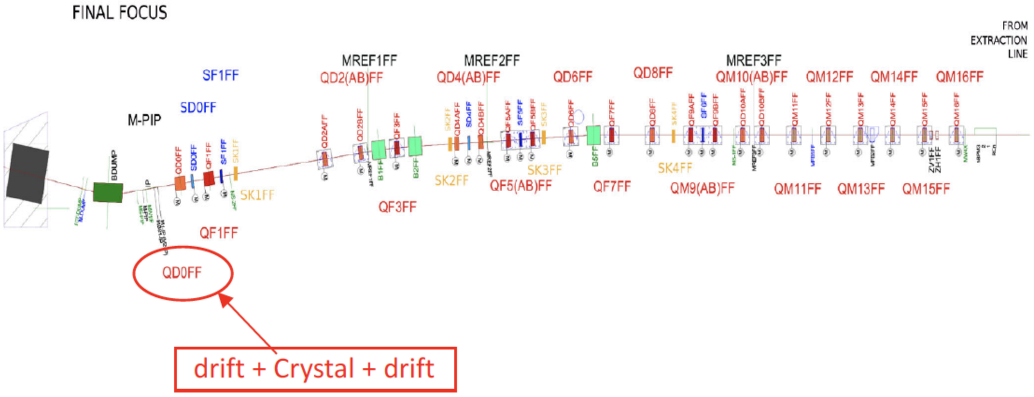

FIGURE 5.5: Final Focus System of ATF2 with QD0FF replacement by the crystal and two drifts.

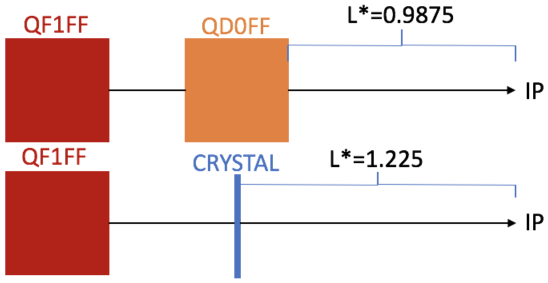

FIGURE 5.6: Zoom of the IP region of the FFS of ATF2. QD0FF has been replaced by a crystal and two drifts. In the figure it is possible to see the different values of L^* used in the simulations for both cases.

In the first stage of the study, some assumptions and approximations were necessary in order to achieve the first simulation results shown in the next sections.

In particular, the crystal can be seen as a thin matrix element that only focuses in the vertical plane and does not act in the horizontal plane, the transfer matrix representing the crystal is:

$$Crystal = \begin{pmatrix} 1 & 0 & 0 & 0 & 0 \\ 0 & 1 & 0 & 0 & 0 \\ 0 & 0 & 1 & 0 & 0 \\ 0 & 0 & -\frac{1}{f} & 1 & 0 \\ 0 & 0 & 0 & 0 & 1 \end{pmatrix}. \tag{5.2}$$

Regarding the assumptions, we are neglecting the bending of the beam by the crystal in the vertical direction. For now, we also neglect the volume reflection and the photon emission, since the channeled beam is studied in this Chapter.

Moreover, there is no chromatic aberration due to the achromatic property of the crystal and we are also neglecting the fact that the particles inside a channel are not focused at the exit of the crystal and the channeled beam size grows with the divergence of the channeled beam. To avoid that this causes a problem, in future studies we will need to be very close to the IP with a short L^* and the initial beam divergence before the crystal should be as small as possible.

The optics matching was done thanks to MAD-X and MAPCLASS programs [7]. In particular, once that the matrix formalism for the crystal description in MAD-X (see fig. 5.7) and MAPCLASS (see fig. 5.8) environments was defined, the matching tool of MAD-X was used to match the twiss parameters at the IP by varying the quadrupoles strengths. The target values for the β-functions at the IP were: β^*_x = 4 mm and β^*_y= 25 μm. The quadrupoles modified were all the matching ones QM16FF → QM11FF and QD10FF, QF9FF, QD8FF, QF7FF, QD6FF, QF5FF, QD4FF, QF3FF, QD2FF and the FD. After some attempts, a solution for the linear part was found and the focusing strength of the crystal ($k_{crystal}$) was set to $-1.17\,\mathrm{m}^{-2}$.

```
CRYSTAL: MATRIX, L=0, RM11=1., RM12=0., RM21=0., RM22=1, RM33=1., RM34=0, RM43:=KCRYSTAL, RM44=1.;
```

FIGURE 5.7: Code line added in MAD-X in order to define the crystal for ATF2.

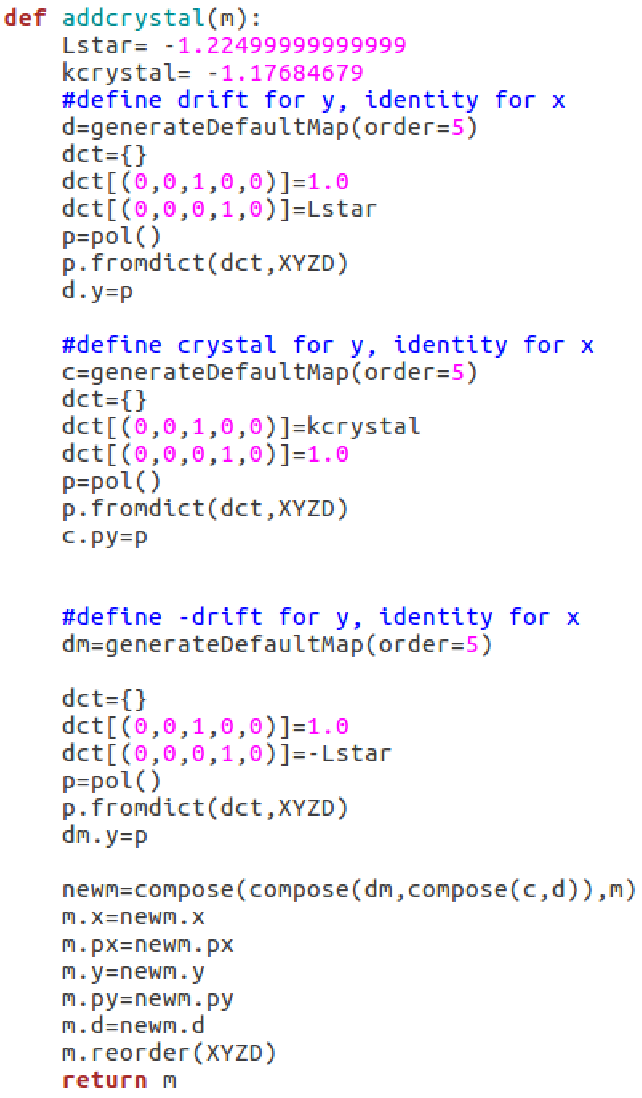

```
def addcrystal(m):
    Lstar= -1.22499999999999
    kcrystal= -1.17684679
    #define drift for y, identity for x
    d=generateDefaultMap(order=5)
    dct={}
    dct[(0,0,1,0,0)]=1.0
    dct[(0,0,0,1,0)]=Lstar
    p=pol()
    p.fromdict(dct,XYZD)
    d.y=p

    #define crystal for y, identity for x
    c=generateDefaultMap(order=5)
    dct={}
    dct[(0,0,1,0,0)]=kcrystal
    dct[(0,0,0,1,0)]=1.0
    p=pol()
    p.fromdict(dct,XYZD)
    c.py=p


    #define -drift for y, identity for x
    dm=generateDefaultMap(order=5)

    dct={}
    dct[(0,0,1,0,0)]=1.0
    dct[(0,0,0,1,0)]=-Lstar
    p=pol()
    p.fromdict(dct,XYZD)
    dm.y=p

    newm=compose(compose(dm,compose(c,d)),m)
    m.x=newm.x
    m.px=newm.px
    m.y=newm.y
    m.py=newm.py
    m.d=newm.d
    m.reorder(XYZD)
    return m
```

FIGURE 5.8: Code lines added to MAPCLASS in order to compute the map of the crystal.

Then, to compute the beam size up to the 5*th* order all the sextupoles (the skew: SK1FF, SK2FF, SK3FF, SK4FF and the normal: SF6FF, SF5FF, SD4FF, SF1FF, SD0FF [31]) were used in MAPCLASS and PTC [46, 47]. An extensive optimization of the sextupole strengths was done in order to get beam size comparable with the QD0FF case. PTC code generates the map (up to the 5^{th} order; the optimization was done order by order) to compute the smallest beam size by varying the sextupole strengths. The beam sizes reached and β-functions, horizontal dispersion and natural chromaticy results are presented in the following section.

5.2 Simulation Results for the Crystal FFS Design

This Section presents the simulation results of the impact of the crystal in comparison with QD0FF case in terms of beta functions, horizontal dispersion, natural chromaticity and beam size.

5.2.1 Beta Function and Horizontal Dispersion

Figure 5.9 shows the beta functions along the beamline. We can see a strong reduction of the β_x function as the crystal does not defocus the horizontal plane as QD0FF would do and a small impact on the β_y function that remains almost the same.

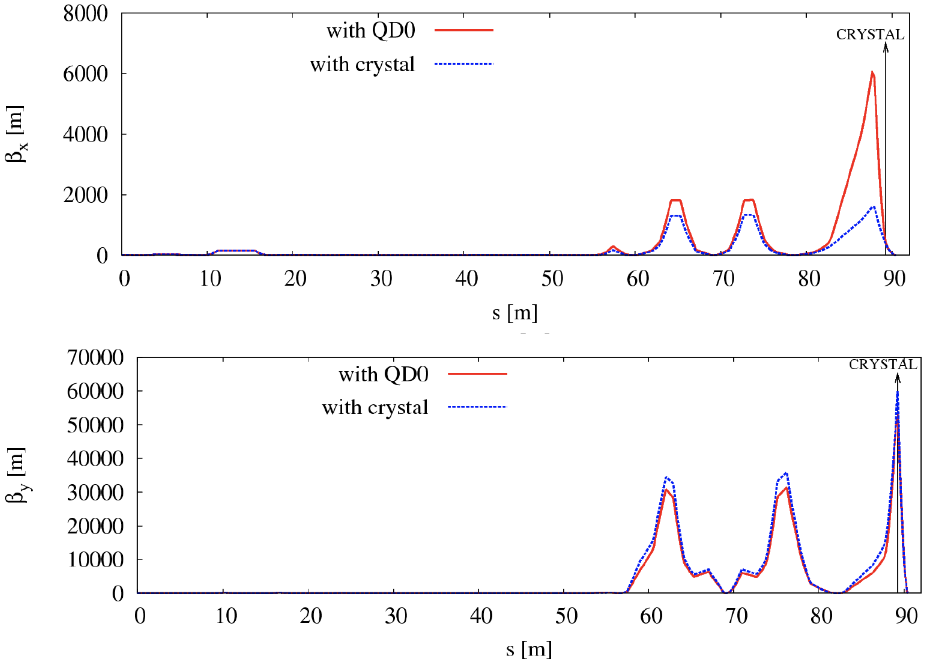

FIGURE 5.9: *Top*: β_x a function of the position along the beam line for QD0FF case and crystal case. *Bottom*: β_y as a function of the position along the beam line for QD0FF case and crystal case. The arrow represents the crystal position along the beamline.

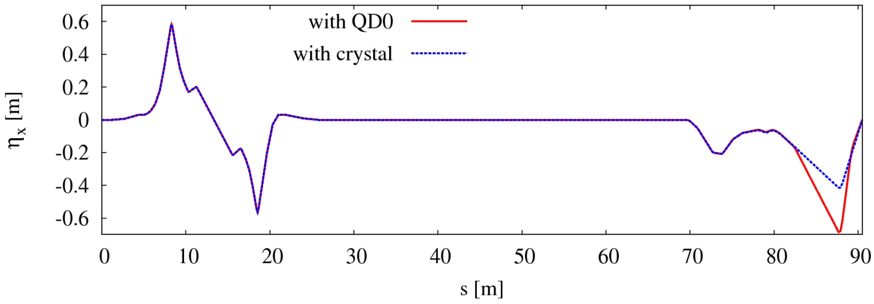

FIGURE 5.10: η_x as a function of the position along the beam line for QD0FF case and crystal case.

Figure 5.10 shows instead the horizontal dispersion in the two different cases. What we can see is a different values of the peaks of η_x function before the IP.

5.2.2 Chromaticity and Beam Size

In order to get the natural chromaticity of quadrupoles the sextupoles are switched off. The natural chromaticity can be computed with Eq. (2.30).

Table 5.1 shows the large impact of the crystal on the natural chromaticity in both planes. We obtain a strong reduction of the chromaticity when using the crystal instead of a normal quadrupole. This can be explained by the fact that we are replacing a quadrupole with an achromatic element.

	QD0FF	Crystal
ξ_x	5868	2639
ξ_y	87888	56734

TABLE 5.1: Values of the chromaticity in both planes for QD0FF and crystal cases.

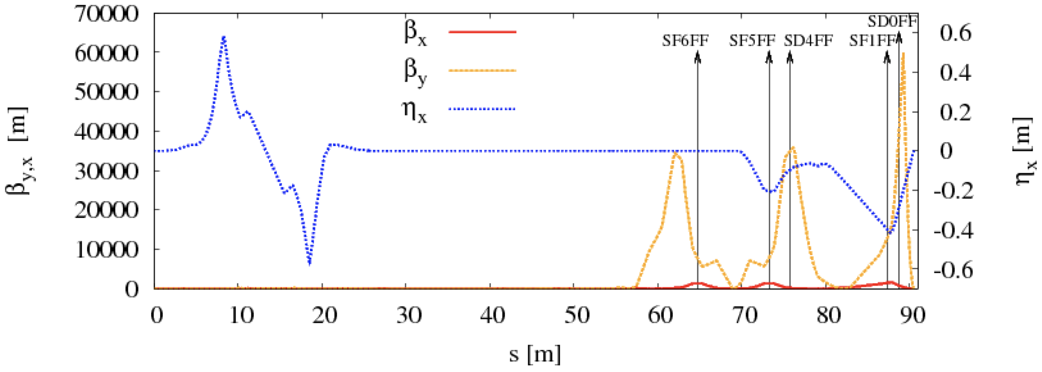

FIGURE 5.11: Lattice design in the crystal case. The arrows indicates the position of the sextupoles along the beamline.

To correct the chromatic aberrations we use sextupoles with positions as in fig. 5.11.

A very important feature of the FFS is that the phase advances between the sextupoles and the IP have to satisfy the condition:

$$\Delta\mu_{x,y} = \frac{\pi}{2} + n\pi, \tag{5.3}$$

where n is an integer. From Table 5.2 we can see the values of the phase advance of the sextupoles SD0FF, SD4FF, SF1FF and SF5FF. The comparison of the phase advance should be done in pairs (SF1FF-SF5FF and SD0FF-SD4FF) and their difference should be equal to 0.5, that in MAD-X units correspond to a π phase advance.

Sextupoles strengths (both for the normal and for the skew sextupoles [31]) used to get the best beam size at the IP in this first attempt in simulation studies are shown in Table 5.3. It is very important to notice the different value especially in SD0FF

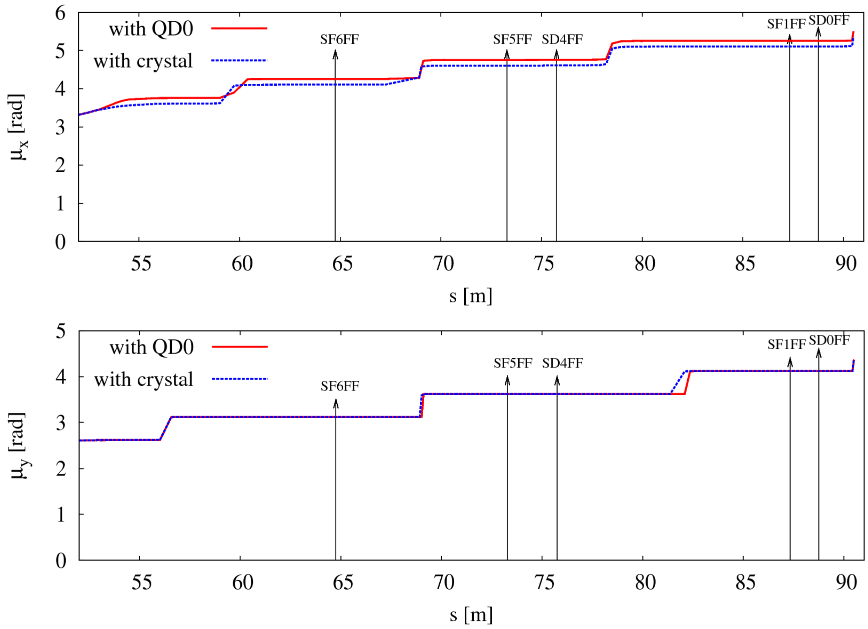

FIGURE 5.12: Phase advance for the horizontal (top) and vertical (bottom) plane. The arrows indicates the position of the sextupoles along the beamline.

μ_x	QD0FF	Crystal
SF1FF	5.25289	5.10608
SF5FF	4.75256	4.60507
SD0FF	5.25295	5.10625
SD4FF	4.75308	4.60577

$\Delta\mu_x$	QD0FF	Crystal
SF1FF-SF5FF	0.50033	0.50083
SD0FF-SD4FF	0.49987	0.50024

μ_y	QD0FF	Crystal
SF1FF	4.11924	4.12171
SF5FF	3.61923	3.62179
SD0FF	4.11926	4.12172
SD4FF	3.61923	3.62182

$\Delta\mu_y$	QD0FF	Crystal
SF1FF-SF5FF	0.50001	0.49994
SD0FF-SD4FF	0.50003	0.49999

TABLE 5.2: Values of the sextupoles phase advances in both planes for QD0FF and crystal cases.

case. In particular, for the crystal we have a bigger value of SD0FF strength and this is not expected since the sextupole should be weaker because the implementation of the crystal had led to a reduction of the chromaticity. A possible cause of this bigger value of the strength could derive from the multipole components [28] of the quadrupoles. So, one of the next steps of the studies includes also the removal of the multipole components of all the matching qudrupoles. Figure. 5.13 shows that the beam sizes reached in the QD0FF case are: σ_x^*= 3.52 μm and σ_y^*= 29.8 nm; while in the crystal case the beam size reached are: σ_x^*= 3.18 μm and σ_y^*= 26.7 nm. So we can say that the crystal could be a very good candidate to achieve the wanted nanometer beam size at the IP.

Figure 5.14 shows the geometric and chromatic aberrations contributions to the beam size where the dpp is the energy spread of the beam that is equal to 0.0008. Going from the dpp$\neq$0 case (that means with chromatic aberrations) to the case of

k_s [m^{-2}]	QD0FF	Crystal
SF6FF	9.08	8.77
SF1FF	-2.62	-7.84
SF5FF	-0.43	1.44
SD0FF	4.33	5.72
SD4FF	15.02	8.82
SK1FF	0.0029	-0.011
SK2FF	-0.12	-0.062
SK3FF	-0.059	-0.022
SK4FF	-0.092	-0.025

TABLE 5.3: Values of the strengths for normal and skew sextupoles in QD0FF and crystal cases.

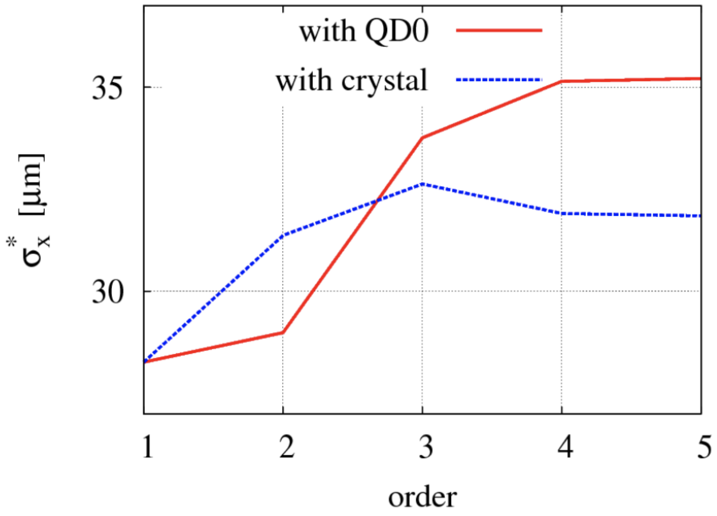

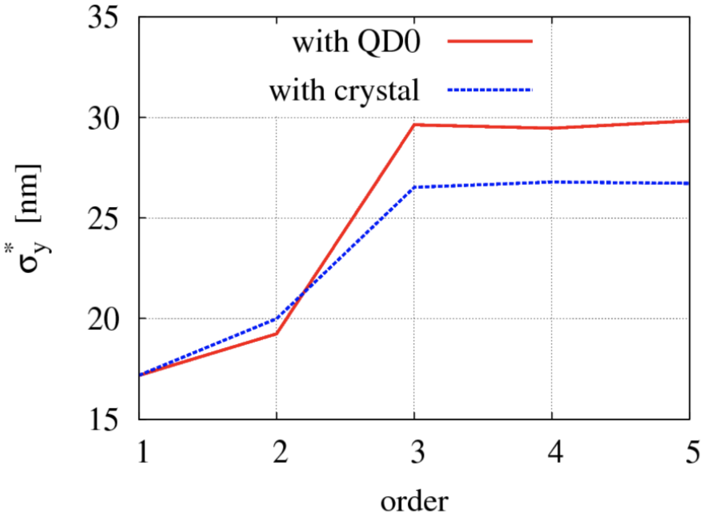

FIGURE 5.13: Horizontal and vertical beam size σ^* evaluated up to 5^{th} order with the multipoles components.

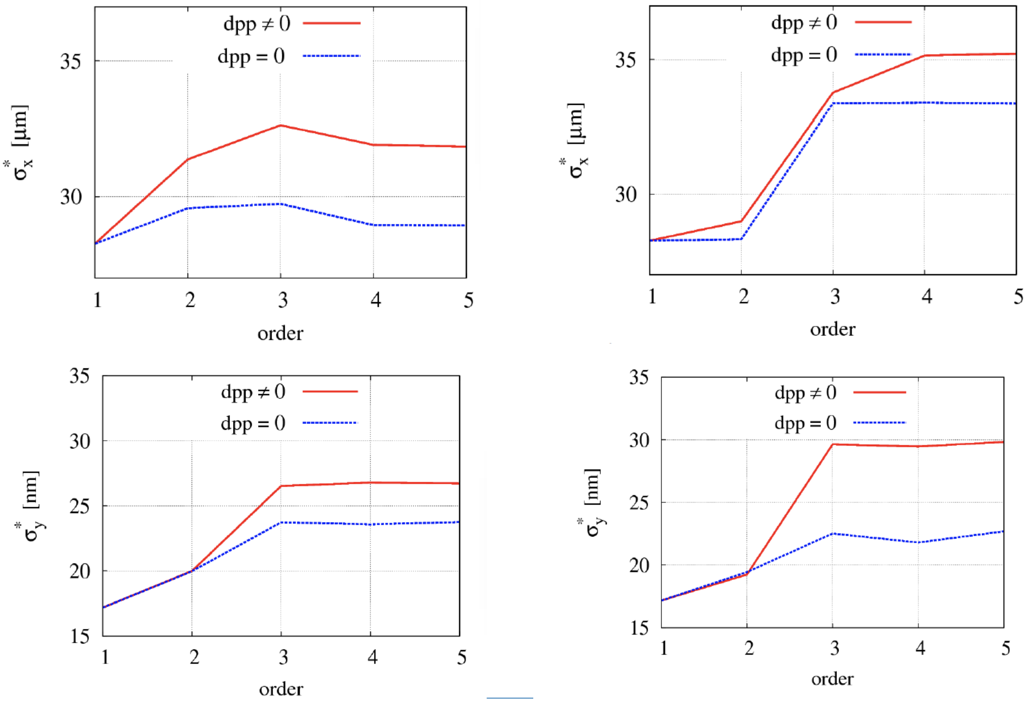

FIGURE 5.14: Beam size values with and without energy spreads. *Left*: crystal case. *Right*: QD0FF case.

dpp=0 (without chromatic aberrations) we can see a significant decrease in the vertical plane for the QD0FF case, while for the crystal we have in both planes a reduction of ≈10%. The important conclusions for this analysis are: the horizontal plane for the crystal is mostly dominated by chromatic aberrations of 2^{nd} and 3^{rd} order; while the vertical one with the crystal is mostly dominated by geometric aberrations of 2^{nd} and 3^{rd} order. It is also important to remember that the beam sizes used in the QD0FF case and crystal case are computed without considering the effect of the octupoles (that can decrease even more the beam size in both cases [37, 38]).

5.3 Luminosity Simulations for CLIC 1.5 TeV

As already said in the introduction of the Chapter, the possibility to deflect channeling particles by bent crystals is known and studied since 1976. Its applications for both positively charged particle beam extraction and collimation have been widely demonstrated and possess perspectives to be used at LHC [74]. Another important aspect of bent crystal is also the possibility of beam focusing. In this Chapter so far, I tried to prove in simulations the real possibility to focus the beam at the IP at a nanometer level using a bent crystal. However, the future e^-e^+ colliders need to focus both negatively and positively particles. Meanwhile, experiments demonstrate that electron beam deflection efficiency remains relatively small even for thin, moderately bent crystals. Besides the strong electron scattering by nuclei, the poor electron channeling efficiency originates also from the unsuitable electron planar potential coordinate dependence, which also makes the method of channeling efficiency increase practically inapplicable [85].

	1 TeV e^-	1 TeV e^+
σ_x^* [nm]	50	20-50
σ_y^* [nm]	15	1
channeling efficiency [%]	50-70	70-90

TABLE 5.4: Estimates of the e^- e^+ beam focus sizes in both focusing xz and normal to it yz planes (table taken from [85]).

According to [85], simulations of crystal focusing in linear colliders to evaluate the total and the peak luminosity ($\mathcal{L}_{tot}$ and $\mathcal{L}_{\%}$) in CLIC 1.5 TeV case are performed. The decision to use CLIC 1.5 TeV case is because it is the baseline that can mostly be approximated at the values considered in table 5.4. The Guinea-Pig program [86] was used to evaluate the luminosity in different cases. One of the assumption was to consider that the β function and the emittance ϵ have the same impact on the beam size increase, in that way it is possible to consider that the beam divergence stays constant in the simulations.

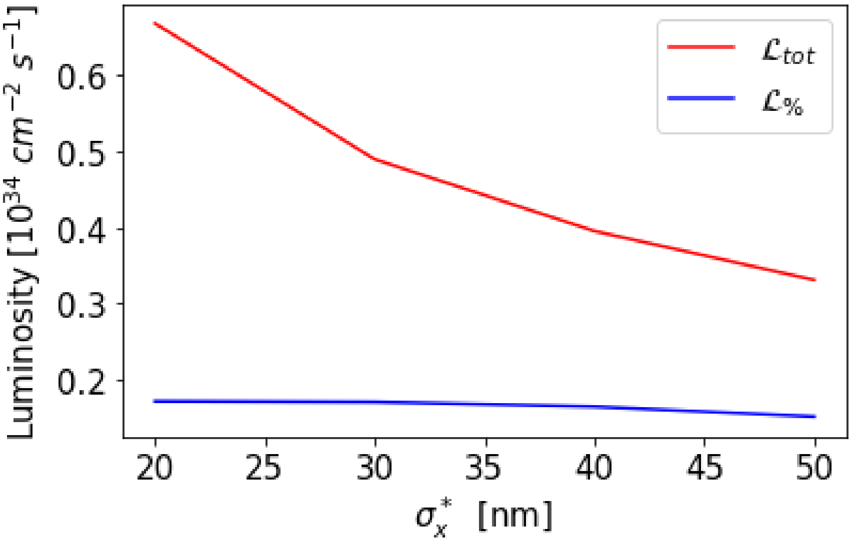

FIGURE 5.15: Total and peak luminosity by varying σ_x^* value of the e^+ beam. The channeling efficiency was taking as a constant value (fixed at 70% for both e^+ and e^- beams).

In fig. 5.15 it is possible to see the total and the peak luminosities versus the σ_x^* values only for the e^+ beam but considering the channeling efficiency constant at the 70% for both e^+ and e^- beams. In fig. 5.16, instead, the beam sizes were taking as a constant values (for the e^+ beam were considered as the design values, $\sigma_x^* = 40$ nm and $\sigma_y^* = 1$ nm taken from [87]), while the channeling efficiency was considered in the range 50%-90%. In all cases, the luminosity is significantly lower than the design values of $\mathcal{L}_{tot} = 3.7$ and $\mathcal{L}_{\%} = 1.4$ taken from [87].

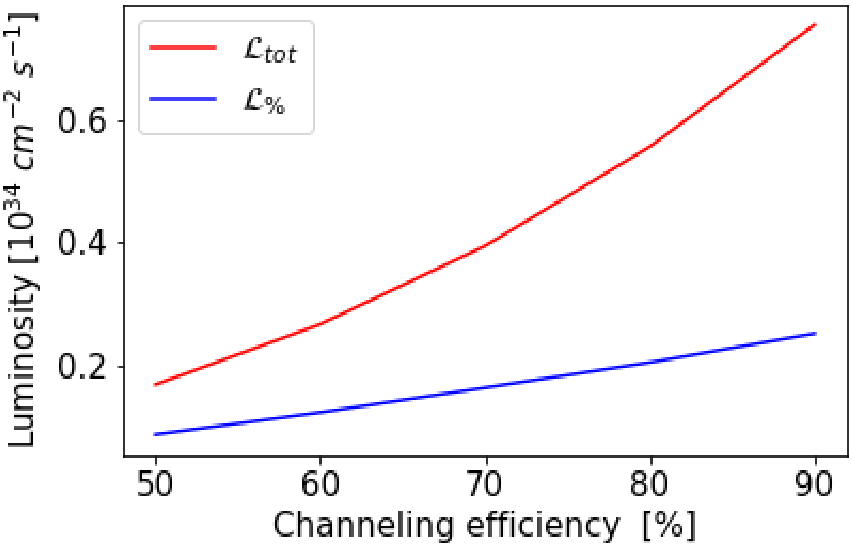

FIGURE 5.16: Total and peak luminosity by varying the channeling efficiency of e^- and e^+ beams. The value of σ_x^* was considered constant (fixed to their design value).

To conclude, the optics simulations done at the beginning showed a good potential for crystal focusing. The new results on the luminosity reached for CLIC 1.5 TeV show a significant lower luminosity performance when using crystals to focus e^- & e^+ beams in future linear colliders, and mostly confirms what said in [85]. The luminosity losses are too big to consider this new concept for CLIC.

Chapter 6

Conclusions and Future Works

This thesis reports some methods for the optimization of the beam size, to a nanometer level, at the Interaction Point of Accelerator Test Facility 2. ATF2 is an accelerator at KEK in Japan, designed to be an R&D platform for future linear colliders (ILC and CLIC). The goals of the ATF2 project are to achieve a 37 nm vertical beam size at the IP (goal 1) and to stabilize the IP beam position at the level of a few nanometers (goal 2). The aim of my thesis is in the framework of both ATF2 goals. The methods described and discussed to achieve these goals are substantially three: mitigation of ground motion effects using the feed-forward control system; experimental studies on IP Beam tuning with ultra-low β_y^* optics; and crystal focusing for FFS.

One potential source of luminosity loss is the motion of the ground itself. The resulting misalignments of the quadrupole magnets cause distortions to the beam orbit and hence beam-beam offsets at the IP. This thesis describes a technique, already in use at ATF2, for compensating this orbit distortion by using seismometers to monitor the misalignment of the quadrupole magnets in real-time. In fact, the compensation of orbit distortion due to quadrupole motion using feed-forward control uses the displacement of the quadrupole to provide the position of the beam to determine the deflection needed. The primary benefit of such a system is that it can correct frequencies higher than the beam repetition rate. The technique was demonstrated for the first time at the KEK ATF using nominal optics where it was able to eliminate 80% of the component of the final focus beam jitter that was due to the motion of the upstream quadrupole [52]. In my thesis work the feed-forward technique has been experimentally verified to perform similarly for the more pushed optics, the ultra-low β_y^* during February 2018 beam operations in ATF2. Future work will examine the possibility of introducing additional sensors and actuators to the feed-forward system. In this way this system could go towards a "global" one.

Lowering the β_y^* value is of special importance for future linear colliders as it allows us to increase the luminosity and therefore improve the collisions efficiency, as well as to reach the desired nanometer beam size at the IP. The ATF2 ultra-low β_y^* lattice is a proposal to test the feasibility for an even larger chromaticity lattice as the CLIC 3 TeV BDS. The ultra-low β_y^* design is an even more advanced optics with a value of $\beta_y^* = 25\ \mu$m, which represents a quarter of that one of the ATF2 nominal lattice. The expected minimum beam size achievable, after high order optimization of the ultra-low β_y^* FFS design, is 20 nm when optimized with a pair of octupoles. Operating the ATF2 FFS with lower β_y^* optics would allow to study the FFS tuning difficulty as function of the IP beam spot size, the impact of the measured multipolar errors, the impact on intensity dependence via wakefield and the compatibility of the IP beam size monitor (Shintake monitor) with a probably enlarged halo. Both the ILC and CLIC projects will benefit from the ATF2 experience at these ultra-low IP betas. Between December 2017 and May 2018, 18 shifts have been dedicated to the ultra-low β_y^* study in ATF2, all ended with an incomplete tuning study. The smallest beam size achieved was $\sigma_y^* = 64 \pm 2$ nm during February 2018 beam operations. The main reason for not have reached a smaller beam size it was mostly because of the not enough tuning time allocated for the study. In conclusion, future work will need more tuning time to be able to address and quantify precisely the performance of the ultra-low β_y^* optics. In fact, there will a full week allocated to this study for November 2018.

A new technique proposed to achieve nanometer beam sizes is using crystals in the Final Focus System region. In my thesis work only the optics aspects were considered using ATF2 as a possible facility for experiments. The first simulation results obtained using only one bent Si crystal as a replacement of the last defocusing quadrupole of the FD (QD0FF) in the FFS has proven to be very fruitful. After the comparison between the conventional optics scheme and the one that involves the crystal, it is possible to say that the natural chromaticity was significantly decreased as well as the beam size of $\approx 10\%$. Then, according to [85], new simulations were done to see the behavior of the crystals in terms of luminosity. CLIC 1.5 TeV was taken as a baseline to do these simulations. The results showed a very significant decrease of luminosity for all the possible cases described in [85] and showed significant limitations of using crystals for focusing e^- beams, especially because of two factors: the not very good focusing and the low channeling efficiency in the crystal for e^- particles.

In conclusion, two out of the three topics presented and discussed in this thesis work have a great possibility to improve performances in Future Linear Collider projects and ATF2.

List of Figures

List of Tables

Bibliography

[1] Howard Baer, Tim Barklow, Keisuke Fujii, Yuanning Gao, Andre Hoang, Shinya Kanemura, Jenny List, Heather E Logan, Andrei Nomerotski, Maxim Perelstein, et al. "The International linear collider technical design report-volume 2: physics". In: *arXiv preprint arXiv:1306.6352* (2013).

[2] M. Aicheler, P. Burrows, M. Draper, T. Garvey, P. Lebrun, K. Peach, N. Phinney, H. Schmickler, D. Schulte, and N. Toge. *A Multi-TeV linear collider based on CLIC technology: CLIC Conceptual Design Report*. Tech. rep. SLAC National Accelerator Lab., Menlo Park, CA (United States), 2014.

[3] Hector Garcia Morales. "Comparative study of Final Focus Systems for CLIC and other luminosity enhancement studies for future linear colliders". PhD thesis. Universitat Politècnica de Catalunya, 2015.

[4] K. Kubo, M. Akemoto, S. Anderson, T. Aoki, S. Araki, K. Bane, P. Blum, J. Corlett, K. Dobashi, P. Emma, et al. "Extremely low vertical-emittance beam in the Accelerator Test Facility at KEK". In: *Physical review letters* **88**.**19** (2002), p. 194801.

[5] Y. Honda, K. Kubo, S. Anderson, S. Araki, K. Bane, A. Brachmann, J. Frisch, M. Fukuda, K. Hasegawa, H. Hayano, et al. "Achievement of Ultralow Emittance Beam in the Accelerator Lest Facility Damping Ring". In: *Physical Review Letters* **92**.**5** (2004), pp. 548021–548025.

[6] H. Grote and F. Schmidt. "MAD-X-an upgrade from MAD8". In: *Particle Accelerator Conference, 2003. PAC 2003. Proceedings of the*. Vol. 5. IEEE. 2003, pp. 3497–3499.

[7] Rogelio Tomás Garcia. "MAPCLASS: a code to optimize high order aberrations". In: *CERN, AB-Note-2006-017 (ABP)* (2006).

[8] PIP. Kalmus. "Particle physics at the turn of the century". In: *Contemporary Physics* **41**.**3** (2000), pp. 129–142.

[9] John T Seeman. "The Stanford linear collider". In: *AIP Conference Proceedings*. Vol. **249**. **2**. AIP. 1992, pp. 2035–2081.

[10] Katsunobu Oide. "Synchrotron-Radiation Limit on the Focusing of Electron Beams". In: *Phys. Rev. Lett.* **61** (15 Oct. 1988), pp. 1713–1715. DOI: `10.1103/PhysRevLett.61.1713`. URL: `https://link.aps.org/doi/10.1103/PhysRevLett.61.1713`.

[11] Matthew Sands. *Emittance growth from radiation fluctuations*. Tech. rep. Stanford Linear Accelerator Center, Menlo Park, CA (USA), 1985.

[12] Nan Phinney, Nobukasu Toge, and Nicholas Walker. "ILC reference design report volume 3-accelerator". In: *arXiv preprint arXiv:0712.2361* (2007).

[13] Lucie Linssen, Akiya Miyamoto, Marcel Stanitzki, and Harry Weerts. *Physics and Detectors at CLIC: CLIC Conceptual Design Report*. Tech. rep. arXiv:1202.5940. CERN-2012-003. ANL-HEP-TR-12-01. DESY-12-008. KEK-Report-2011-7. Comments: 257 p, published as CERN Yellow Report CERN-2012-003. Geneva, 2012. URL: `http://cds.cern.ch/record/1425915`.

[14] Pantaleo Raimondi and Andrei Seryi. "Novel Final Focus Design for Future Linear Colliders". In: *Phys. Rev. Lett.* **86** (17 Apr. 2001), pp. 3779–3782. DOI: `10.1103/PhysRevLett.86.3779`. URL: `https://link.aps.org/doi/10.1103/PhysRevLett.86.3779`.

[15] R. Tomás. "Overview of the Compact Linear Collider". In: *Phys. Rev. ST Accel. Beams* **13** (1 Jan. 2010), p. 014801. DOI: `10.1103/PhysRevSTAB.13.014801`. URL: `https://link.aps.org/doi/10.1103/PhysRevSTAB.13.014801`.

[16] Eduardo Marin Lacoma. "Design and higher order optimisation of Final Focus Systems for Linear Colliders". PhD thesis. CERN, 2012-11-09. URL: `http://inspirehep.net/record/1231151/files/CERN-THESIS-2012-218.pdf`.

[17] R. Tomás. "Nonlinear optimization of beam lines". In: *Phys. Rev. ST Accel. Beams* **9** (8 Aug. 2006), p. 081001. DOI: `10.1103/PhysRevSTAB.9.081001`. URL: `https://link.aps.org/doi/10.1103/PhysRevSTAB.9.081001`.

[18] S. Guiducci. "Chromaticity". In: LNF-91-031-R (June 1991), 16 p. URL: `http://cds.cern.ch/record/223348`.

[19] Karl L. Brown. "Basic optics of the SLC final focus system". In: *PROCEEDINGS OF THE INTERNATIONAL WORKSHOP ON NEXT GENERATION LINEAR COLLIDERS: STANFORD, CA., NOVEMBER 28 - DECEMBER 9, 1988*. 1988. URL: `http://www-public.slac.stanford.edu/sciDoc/docMeta.aspx?slacPubNumber=SLAC-PUB-4811`.

[20] M. Berndt, V. Bressler, F. Le Diberder, V. Medzhidzade, Yu Koisin, R. Ruth, F. Halbo, J. Jeanjean, D. Plouffe, H. Nakayama, et al. *Final focus test beam: Project design report*. Tech. rep. 1991.

[21] Mika Masuzawa et al. "Next generation B-factories". In: *Proc. IPAC* 10 (2010).

[22] C. Collette, S. Janssens, K. Artoos, A. Kuzmin, P. Fernandez Carmona, M. Guinchard, R. Leuxe, and C. Hauviller. “Nano-motion control of heavy quadrupoles for future particle colliders: An experimental validation”. In: *Nucl. Instrum. Meth.* A643 (2011), pp. 95–101. DOI: `10.1016/j.nima.2011.04.028`.

[23] Fabien Plassard, Andrea Latina, Eduardo Marin, Rogelio Tomás, and Philip Bambade. “Quadrupole-free detector optics design for the Compact Linear Collider final focus system at 3 TeV”. In: *Phys. Rev. Accel. Beams* **21** (1 Jan. 2018), p. 011002. DOI: `10.1103/PhysRevAccelBeams.21.011002`. URL: `https://link.aps.org/doi/10.1103/PhysRevAccelBeams.21.011002`.

[24] F. Hinode et al. *Atf accelerator test facility design and study report no. 4, KEK, Tsukuba, Japan 1995*.

[25] Hans Heinrich Braun, Andrzej Wolski, Leo Jenner, Daniel Schulte, Grahame A. Blair, Jeff Gronberg, Masao Kuriki, Armin Reichold, Chafik Driouichi, et al. *ATF2 Proposal: v. 1*. Tech. rep. 2005.

[26] Marcin Patecki. “Optimisation analysis and improvement of the effective beam sizes in Accelerator Test Facility 2”. PhD thesis. Warsaw University of Technology (PL), 2016.

[27] Andrei Seryi, Rogelio Tomas, Frank Zimmermann, Kiyoshi Kubo, Shigeru Kuroda, Toshiyuki Okugi, Toshiaki Tauchi, Nobuhiro Terunuma, Junji Urakawa, Glen White, et al. “Experimental and theoretical progress of linear collider final focus design and ATF2 facility”. In: *Nuclear Instruments and Methods in Physics Research Section A: Accelerators, Spectrometers, Detectors and Associated Equipment* 740 (2014), pp. 2–5.

[28] E. Marin et al. “Design and high order optimization of the Accelerator Test Facility lattices”. In: *Phys. Rev. ST Accel. Beams* **17** (2 Feb. 2014), p. 021002. DOI: `10.1103/PhysRevSTAB.17.021002`. URL: `https://link.aps.org/doi/10.1103/PhysRevSTAB.17.021002`.

[29] J. Alabau-Gonzalvo, C. Blanch Gutierrez, A. Faus-Golfe, JJ. Garcia-Garrigos, J. Resta-Lopez, J. Cruz, D. McCormick, G. White, and M. Woodley. “The ATF2 Multi-OTR System: Studies and Design Improvements”. In: *International Beam Instrumentation Conference*. 2012.

[30] YI. Kim, R. Ainsworth, A. Aryshev, ST. Boogert, G. Boorman, J. Frisch, A. Heo, Y. Honda, WH. Hwang, JY. Huang, et al. “Cavity beam position monitor system for the Accelerator Test Facility 2”. In: *Physical Review Special Topics-Accelerators and Beams* **15.4** (2012), p. 042801.

[31] T. Okugi, S. Araki, P. Bambade, K. Kubo, S. Kurado, M. Masuzawa, E. Marin, T. Naito, T. Tauchi, N. Terunuma, et al. “Linear and second order optics corrections for the KEK Accelerator Test Facility final focus beam line”. In: *Physical Review Special Topics-Accelerators and Beams* **17.2** (2014), p. 023501.

[32] T. Shintake, D. Walz, A. Hayakawa, M. Ohashi, K. Yasuda, D. Burke, S. Wagner, Y. Ozaki, and H. Hayano. “Design of laser Compton spot size monitor”. In: *Int. J. Mod. Phys. Proc. Suppl.* 1.KEK-PREPRINT-92-65 (1992), pp. 215–218.

[33] Yan Jacqueline. “Precise Measurement of Nanometer Scale Electron Beam Sizes Using Laser Interference by Shintake Monitor”. PhD thesis. University of Tokyo, 2015.

[34] Hitoshi Hayano. “Wire scanners for small emittance beam measurement in ATF”. In: *arXiv preprint physics/0008084* (2000).

[35] Jacqueline Yan, Masahiro Oroku, Youhei Yamaguchi, Takashi Yamanaka, Yoshio Kamiya, Taikan Suehara, Sachio Komamiya, Toshiyuki Okugi, Nobuhiro Terunuma, Toshiaki Tauchi, et al. “Shintake Monitor Nanometer Beam Size Measurement and Beam Tuning”. In: *Physics Procedia* **37** (2012), pp. 1989–1996.

[36] Marcin Patecki and Rogelio Tomás. “Effects of quadrupole fringe fields in final focus systems for linear colliders”. In: *Physical Review Special Topics-Accelerators and Beams* **17.10** (2014), p. 101002.

[37] E. Marin, M. Modena, T. Tauchi, N. Terunuma, R. Tomás, GR. White, et al. *Specifications of the octupole magnets required for the ATF2 ultra-low ß* lattice*. Tech. rep. SLAC National Accelerator Laboratory (SLAC), 2014.

[38] M. Modena. “Update on 2 Octupoles Procurement for ATF2 Final Focus Systems”. In: *18th ATF2 Project meeting*. 2015.

[39] Klaus Wille. *The physics of particle accelerators: an introduction*. Clarendon Press, 2000.

[40] Paul Ehrenfest and Tatiana Ehrenfest. *The conceptual foundations of the statistical approach in mechanics*. Courier Corporation, 2002.

[41] OR. Blanco, R. Tomás, and P. Bambade. “Beam focusing limitation from synchrotron radiation in two dimensions”. In: *Physical Review Accelerators and Beams* **19.2** (2016), p. 021002.

[42] Fabien Plassard. “Design optimization of the International Linear Collider Final Focus System with a long L*”. CERN, 2015.

[43] S.Y. Lee. *Accelerator Physics*. World Scientific, 2004. ISBN: 9789812562005. URL: `https://books.google.ch/books?id=VTc8Sdld5S8C`.

[44] Karl L Brown. *FIRST-AND SECOND-ORDER MATRIX THEORY FOR THE DESIGN OF BEAM TRANSPORT SYSTEMS AND CHARGED PARTICLE SPECTROMETERS.* Tech. rep. Stanford Linear Accelerator Center, Calif., 1971.

[45] É. Forest. "Beam Dynamics: A New Attitude and Framework, volume 8 of The Physics and Technology of Particle and Photon Beams". In: *Harwood Academic Pub., Amsterdam* (1998).

[46] Etienne Forest, Frank Schmidt, and Eric McIntosh. *Introduction to the polymorphic tracking code. Fibre bundles, polymorphic taylor types and"Exact Tracking".* Tech. rep. High Energy Accelerator Research Organization, 2002.

[47] Frank Schmidt. "Mad-x ptc integration". In: *Particle Accelerator Conference, 2005. PAC 2005. Proceedings of the*. IEEE. 2005, pp. 1272–1274.

[48] Vladimir Shiltsev. "Observations of random walk of the ground in space and time". In: *Physical review letters* **104.23** (2010), p. 238501.

[49] Andrey Sery and Olivier Napoly. "Influence of ground motion on the time evolution of beams in linear colliders". In: *Physical review E* **53.5** (1996), p. 5323.

[50] Kiyoshi Kubo. "Estimation of orbit change and emittance growth due to random misalignment in long linacs". In: *Physical Review Special Topics-Accelerators and Beams* **14.1** (2011), p. 014401.

[51] Tor O. Raubenheimer. "Estimates of emittance dilution and stability in high-energy linear accelerators". In: *Physical Review Special Topics-Accelerators and Beams* **3.12** (2000), p. 121002.

[52] D.R. Bett et al. "Compensation of orbit distortion due to quadrupole motion using feed-forward control atKEKATF". In: *Nuclear Instruments and Methods in Physics Research Section A: Accelerators, Spectrometers, Detectors and Associated Equipment* **895** (2018), pp. 10–18. ISSN: 0168-9002. DOI: `https://doi.org/10.1016/j.nima.2018.03.037`. URL: `http://www.sciencedirect.com/science/article/pii/S0168900218303735`.

[53] J. Pfingstner, K. Artoos, C. Charrondiere, M. Patecki, Y. Renier, D. Schulte, R. Tomás, A. Jérémie, K. Kubo, S. Kuroda, et al. "Mitigation of ground motion effects in linear accelerators via feed-forward control". In: *Physical Review Special Topics-Accelerators and Beams* **17.12** (2014), p. 122801.

[54] T. Himel. "Feedback: Theory and accelerator applications". In: *Annual Review of Nuclear and Particle Science* **47.1** (1997), pp. 157–192.

[55] V.A. Dolgashev, S.G. Tantawi, Y. Higashi, and T. Higo. "Status of high power tests of normal conducting single-cell structures". In: 806233.SLAC-PUB-14681 (2008), MOPP083.

[56] Christophe Collette, David Tshilumba, Lionel Fueyo-Rosa, and I Romanescu. “Conceptual design and scaled experimental validation of an actively damped carbon tie rods support system for the stabilization of future particle collider superstructures”. In: *Review of scientific instruments* **84.2** (2013), p. 023302.

[57] ATF2 Group et al. “ATF2 Proposal Vol. 2”. In: *arXiv preprint physics/0606194* (2006).

[58] G.R. White, R. Ainsworth, T. Akagi, J. Alabau-Gonzalvo, D. Angal-Kalinin, S. Araki, A. Aryshev, S. Bai, P. Bambade, D.R. Bett, et al. “Experimental validation of a novel compact focusing scheme for future energy-frontier linear lepton colliders”. In: *Physical review letters* **112.3** (2014), p. 034802.

[59] S. Fartoukh and R. De Maria. “Optics and Layout Solutions for HL-LHC with Large Aperture Nb _{3} Sn and NB-TI Inner Triplets”. In: 1205201.CERN-ATS-2012-136 (2012), MOPPC011.

[60] Christophe Collette, Stefan Janssens, Pablo Fernandez-Carmona, Kurt Artoos, Michael Guinchard, Claude Hauviller, and André Preumont. “Inertial Sensors for Low-Frequency Seismic Vibration Measurement”. In: *Bulletin of the seismological society of America* **102.4** (2012), pp. 1289–1300.

[61] Douglas Robert Bett. “The development of a fast intra-train beam-based feedback system capable of operating on the bunch trains of the International Linear Collider”. In: (2013). URL: `http://www-pnp.physics.ox.ac.uk/~font/thesis/thesisBett.pdf`.

[62] Ben Constance. “Design and beam testing of a fast, digital intra-train feedback system and its potential for application at the International Linear Collider”. In: (2011).

[63] S. H. John, W. Eaton, D. Bateman, and R. Wehbring. *GNU Octave version 4.2.0 manual: a high-level interactive language for numerical computations*. 2016.

[64] Benoit Bolzon. “Etude des vibrations et de la stabilisation à l’échelle sous-nanométrique des doublets finaux d’un collisionneur linéaire”. PhD thesis. Université de Savoie, 2007.

[65] J.G. Proakis and D.G. Manolakis. “Digital Signal Processing Macmillan Publishing Company”. In: *USA* (1992).

[66] M. Patecki, D. Bett, E. Marin, F. Plassard, R. Tomás, K. Kubo, S. Kuroda, T. Naito, T. Okugi, T. Tauchi, et al. “Probing half β_y^* optics in the Accelerator Test Facility 2”. In: *Physical Review Accelerators and Beams* **19.10** (2016), p. 101001.

[67] Toshiyuki Okugi et al. “Achievement of Small Beam Size at ATF2 Beamline”. In: *28th Linear Accelerator Conf.(LINAC’16), East Lansing, MI, USA, 25-30 September 2016*. JACOW, Geneva, Switzerland. 2017, pp. 27–31.

[68] P. Bambade, T. Tauchi, N. Terunuma, J. Jones, R. Tomás, D. Wang, E. Marin, Y. Renier, J. Gao, G. White, et al. *ATF2 ultra-low IP betas proposal*. Tech. rep. 2009.

[69] Glen White, Andrei Seryi, Mark Woodley, Eduardo Marin, Yoshio Kamiya, S Bai, Benoit Bolzon, K Kubo, S Kuroda, Toshiyuki Okugi, et al. “Operational Experiences Tuning the ATF2 Final Focus Optics Towards Obtaining a 37nm Electron Beam IP Spot Size”. In: *1st International Particle Accelerator Conference (IPAC 2010)*. Joint Accelerator Conferences Website. 2010, pp. 2383–2385.

[70] M. Woodley. “Summary of activities, software development and tuning performance pertaining to the extraction line system”. In: *11th ATF2 Project Meeting*. 2011.

[71] J. Alabau-Gonzalvo, M. Woodley, D. McCormick, J.J. Garcia-Garrigos, C. Blanch Gutierrez, A. Faus-Golfe, J. Cruz, and G. White. “Optical transition radiation system for ATF2”. In: *Conf. Proc.* Vol. 110904. IPAC-2011-TUPC127. 2012, pp. 1317–1319.

[72] Sha Bai, Alexander Aryshev, Philip Bambade, Doug Mc Cormick, Benoit Bolzon, Jie Gao, Toshiaki Tauchi, and Feng Zhou. “First beam waist measurements in the final focus beam line at the KEK Accelerator Test Facility”. In: *Physical Review Special Topics-Accelerators and Beams* **13.9** (2010), p. 092804.

[73] W. Scandale, G. Arduini, M. Butcher, F. Cerutti, S. Gilardoni, A. Lechner, R. Losito, A. Masi, E. Metral, D. Mirarchi, et al. “Observation of focusing of 400 GeV/c proton beam with the help of bent crystals”. In: *Physics letters B* **733** (2014), pp. 366–372.

[74] W. Scandale, G. Arduini, M. Butcher, F. Cerutti, M. Garattini, S. Gilardoni, A. Lechner, R. Losito, A. Masi, D. Mirarchi, et al. “Observation of channeling for 6500 GeV/c protons in the crystal assisted collimation setup for LHC”. In: *Physics Letters B* **758** (2016), pp. 129–133.

[75] W. Scandale, G. Arduini, F. Cerutti, M. Garattini, S. Gilardoni, A. Masi, D. Mirarchi, S. Montesano, S. Petrucci, S. Redaelli, et al. “Comprehensive study of beam focusing by crystal devices”. In: *Physical Review Accelerators and Beams* **21.1** (2018), p. 014702.

[76] M.A. Gordeeva, M.P. Gurev, A.S. Denisov, Y. Platonov, V.V. Skorobogatov, A.I. Smirnov, O.L. Fedin, A.I. Shchetkovskii, V.I. Baranov, N.A. Galyaev, et al. “First results on the focusing of a 70-GeV proton beam by a curved single crystal”. In: *JETP Lett* **54.9** (1991).

[77] A.M. Taratin and S.A. Vorobiev. ““Volume reflection” of high-energy charged particles in quasi-channeling states in bent crystals”. In: *Physics Letters A* **119.8** (1987), pp. 425–428.

[78] A.M. Taratin and S.A. Vorobiev. "Deflection of high-energy charged particles in quasi-channeling states in bent crystals". In: *Nuclear Instruments and Methods in Physics Research Section B: Beam Interactions with Materials and Atoms* **26.4** (1987), pp. 512–521.

[79] A.I. Sytov, V. Guidi, V.V. Tikhomirov, E. Bagli, L. Bandiera, G. Germogli, and A. Mazzolari. "Planar channeling and quasichanneling oscillations in a bent crystal". In: *The European Physical Journal C* **76.2** (2016), p. 77.

[80] Walter Scandale, Alberto Vomiero, S Baricordi, P Dalpiaz, M Fiorini, V Guidi, A Mazzolari, R Milan, G Della Mea, G Ambrosi, et al. "Experimental study of the radiation emitted by 180- GeV/ c electrons and positrons volume-reflected in a bent crystal". In: *Physical Review A* **79.1** (2009), p. 012903.

[81] V.M. Katkov, V.M. Strakhovenko, et al. *Electromagnetic processes at high energies in oriented single crystals*. World Scientific, 1998.

[82] V.A. Arutyunov, N.A. Kudryashov, V.M. Samconov, and M.N. Strikhanov. "Radiation of ultrarelativistic charged particles in a bent crystal". In: *Nuclear Physics B* **363**.2-3 (1991), pp. 283–300.

[83] V.A. Maisheev. "Volume reflection of ultrarelativistic particles in single crystals". In: *Physical Review Special Topics-Accelerators and Beams* **10.8** (2007), p. 084701.

[84] V.M. Biryukov, V. I. Kotov, and Yu A. Chesnokov. "Steering of high-energy charged-particle beams by bent single crystals". In: *Physics-Uspekhi* **37.10** (1994), p. 937.

[85] Victor V. Tikhomirov. "Can electron beams be really focused by bent crystals?" In: *arXiv preprint arXiv:1809.06164* (2018).

[86] Daniel Schulte. *Study of electromagnetic and hadronic background in the interaction region of the TESLA collider*. Tech. rep. 1997.

[87] The CLIC, M.J. Boland, U. Felzmann, P.J. Giansiracusa, T.G. Lucas, R.P. Rassool, C. Balazs, T.K. Charles, K. Afanaciev, I. Emeliantchik, et al. "Updated baseline for a staged Compact Linear Collider". In: *arXiv preprint arXiv:1608.07537* (2016).